JOURNAL OF TELECOMMUNICATIONS AND INFORMATION TECHNOLOGY

2/2005

MIKON 2004 young authors special issue
edited by Józef Modelski

Ultra-wideband radar targets discrimination based on discrete E-pulse synthesis
A. Aleksandrov et al. — Paper 3

Ultra-wideband 3D image processing for improving landmine detection with GPR
E. Ligthart et al. — Paper 9

Analysis of errors in on-wafer measurements due to multimode propagation in CB-CPW
A. Lewandowski and W. Wiatr — Paper 16

A 100 W ISM 2.45 GHz-band power test system
W. Wojtasiak, D. Gryglewski, and W. Gwarek — Paper 23

A broadband multistate interferometer for impedance measurement
P. Szymański and W. Wiatr — Paper 29

Absorption of EM energy by human body in the vicinity of the GSM base station antenna
D. Wójcik, T. Topa, and K. Szczepański — Paper 34

Characterization of an aperture-stacked patch antenna for ultra-wideband wearable radio systems
M. Klemm and G. Troester — Paper 39

Spatial power combiner using a planar active transmitarray of stacked patches
F.-C. E. Tsai and M. E. Bialkowski — Paper 45

Editorial Board

Editor-in Chief: . . . . . ***Paweł Szczepański***

Associate Editors: . . . . . ***Krzysztof Borzycki***
Marek Jaworski

Managing Editor: . . . . . ***Maria Łopuszniak***

Technical Editor: . . . . . ***Anna Tyszka-Zawadzka***

Editorial Advisory Board

Chairman: . . . . . ***Andrzej Jajszczyk***
Marek Amanowicz
Daniel Bem
Wojciech Burakowski
Andrzej Dąbrowski
Andrzej Hildebrandt
Witold Hołubowicz
Andrzej Jakubowski
Alina Karwowska-Lamparska
Marian Kowalewski
Andrzej Kowalski
Józef Lubacz
Tadeusz Łuba
Krzysztof Malinowski
Marian Marciniak
Józef Modelski
Ewa Orłowska
Andrzej Pach
Zdzisław Papir
Michał Pióro
Janusz Stokłosa
Wiesław Traczyk
Andrzej P. Wierzbicki
Tadeusz Więckowski
Józef Woźniak
Tadeusz A. Wysocki
Jan Zabrodzki
Andrzej Zieliński

ISSN 1509-4553

© Copyright by National Institute of Telecommunications
Warsaw 2005

Circulation: 300 copies

Sowa - druk na życzenie, www.sowadruk.pl, tel. 022 431-81-40

JOURNAL OF TELECOMMUNICATIONS AND INFORMATION TECHNOLOGY

Preface

The special issue of the *Journal of Telecommunications and Information Technology* is devoted to the **15th International Conference on Microwaves, Radar and Wireless Communications MIKON'04**, which was held on 17–19 May 2004 in Warsaw. The event is widely considered one of the highest ranking microwave conference. Expressing my gratitude towards the Editorial Board, I would like to present a brief history of the Conference as well as a short summary of last year's MIKON.

It is worth pointing out that the success of last year's conference should be perceived in the light of MIKON's 35-year long history. It started in 1969 as a microwave solid state technology conference MECS and in 1983 it was transformed and renamed into a microwave conference. All over the years, MIKON has been continuously modified and expanded. The first nine conferences were national assemblies of the Polish microwave community, organized every two or three years with only a limited number of invited foreign guests. In 1994 MIKON received the international status. Since then it has been organised biannually in May under the auspices of two parent institutions: the Polish Academy of Sciences, being the original one, and the new one – the Institute of Electrical and Electronics Engineers, and is hosted by various Polish cities – biggest research and culture centres. Due to the fact that telecommunications and radar technology are the principal driving forces behind microwave research, in 1998 MIKON was extended once again and since then has been held as an international conference on microwaves, radar and wireless communications. Nowadays, MIKON assembles the whole Polish microwave and radiolocation community as well as numerous representatives of our immediate neighbors. It is also privileged to host the leaders of other foreign research centres collaborating with Poland as well as scientists of Polish origin, now working and living abroad. Almost 140 papers were presented during MIKON-1994 as well as for the MIKON-1996. Each of the following three conferences in Cracow (1998), Wrocław (2000) and Gdańsk (2002) featured about 190 papers, making MIKON one of leading events in Europe.

In 2004 MIKON moved to Warsaw, with the record number of **234** papers accepted for presentation: 105 from Poland and, what we highly appreciate, 129 of those come from abroad, from **31** countries. These figures are certainly indicative of the enhanced international dimension of MIKON. The majority of foreign papers were submitted by the neighboring countries – Russia, Ukraine, Germany, Sweden and Lithuania as well as other European

countries including France, Italy and the Netherlands. From overseas, the largest number of papers came from Australia and the USA. Out of the accepted papers, 137 were oral and 97 poster presentations. The MIKON-2004 program comprised 36 sessions in total. The number of contributions from the area of wireless communications and antennas had been constantly increasing, and last year 10 sessions were organized on these subjects. Traditional MIKON topics such as CAD methods, measurement techniques, active and passive components were also very well covered. Although millimetre technology, integrated circuits and optoelectronics have attracted less interest in regular papers, they were well represented by invited speakers.

The MIKON-2004 was for the eighth time organized by the **Telecommunications Research Institute** (PIT). Celebrating already its 70th anniversary, PIT is nowadays the leading research centre in radar technology, assembling the biggest group of microwave specialists in Poland. Large scale research collaboration with various technical universities has facilitated the development by PIT of high quality advanced systems, also well known on the international market. PIT will also be the organizer of MIKON-2006 in Cracow.

This year's MIKON constituted the kernel of the Microwave and Radar Week-2004 in Poland (17–21 May), which was comprised, besides MIKON, of the following events: the *5th International Radar Symposium*, the *17th International Conference on Electromagnetic Fields and Materials* and the *East-West Workshop on Advanced Techniques in Electromagnetics*. A total number of 506 participants from 40 countries attended the whole Week, for which 374 papers were presented.

The Polish microwave and radar community felt privileged to have many distinguished guests among the Conference participants. We took the chance of listening to welcome addresses given by Prof. Michał Kleiber, Minister of Scientific Research and Information Technology, IEEE MTT 2004 President, Prof. Robert Trew and Prof. Władysław Włosiński of the Polish Academy of Sciences. Furthermore, six distinguished members of the MIKON community were presented with special *certificates of appreciation* in recognition of their outstanding contributions to the technical program of the Conferences over the years as well as the promotion of MIKON among the world's microwave and radar community.

Last year's Conference hosted a strong representation of young authors. MIKON-2004 continued the Young Scientist Contest addressed to young engineers and Ph.D. students. In whole, 83 papers of young authors were submitted for the competition, over half of which came from abroad. The prizes were founded by the European Microwave Association, IEEE AP/AES/MTT Joint Chapter of Poland Section and the Polish Academy of Sciences.

This special issue comprises 15 papers, chosen from those presented by young authors. A significant number of the papers is devoted to the analysis and design of antennas and antenna arrays (particularly for mobile communication systems). Another group of papers focuses on new microwave measurement techniques as well as advanced numerical methods and modelling in electrodynamics. Finally, the areas of microwave photonics and lightweight technology are also represented.

It is my hope that this volume addresses issues of interest to the Readers and will prove relevant in terms of practical application.

Józef Modelski
Guest Editor

Paper

Ultra-wideband radar targets discrimination based on discrete E-pulse synthesis

Andrey Aleksandrov, Timophey Shevgunov, Andrey Baev, and Yury Kuznetsov

Abstract—A frequency domain approach to the E-pulse radar target discrimination technique is introduced. This approach allows the interpretation of E-pulse phenomenon via the E-pulse spectrum. The discrete E-pulse and its relation to continuous E-pulse are shown. The addition of extra zeroes to E-pulse structure has been suggested and its influence on the increasing of discrimination accuracy has been proved. The results of discrimination scheme digital simulation by using the characteristic E-pulse parameters for known targets are presented.

Keywords— radar target recognition, signal processing.

1. Introduction

A growing interest in the target discrimination methods using ultra-wideband target response has been arisen recently. Ultra-wideband radar proposes using sharp pulses with duration about units of nanoseconds. These pulses excite electromagnetic oscillations in the target defined by geometric range and form of it. According to the Baum's singularity expansion method (SEM) [1], which provides the necessary mathematical formulation for describing the transient behavior of conducting targets, scattered target response can be represented as a sum of damped oscillations:

$$y(t) = x(t) + w(t)$$

$$= \sum_{k=1}^{K} A_k \mathrm{e}^{-\sigma_k t} \cos(\omega_k t + \varphi_k) + w(t), \qquad (1)$$

where $s_k = \sigma_k + j\omega_k$ is the kth aspect-independent natural complex frequency of the target, and A_k and φ_k are the aspect- and excitation-dependent amplitude and phase of the kth target mode, respectively, $w(t)$ is an additive Gaussian band-limited noise. The number of natural resonances K is determined by the finite frequency content of the waveform exciting the target and by the geometrical shape of the object.

The identification methods using in the ultra-wideband radar can be divided into parametric and non-parametric. Parametric methods consist in the estimation of the target specified features based on as its natural frequencies in the measured response [2]. Determined parameters can be compared to the known parameters of the targets included in the database and identification decision can be made relaying on it. The main part of these methods consists – of feature extraction technique: Prony's method, pencil-of-function method or ESPRIT.

Another way of the ultra-wideband target discrimination is the E-pulse method [3]. This method offers to fit special signal (E-pulse) to the target response so the convolution of the response and the signal is minimum (or equal to zero in the ideal case) at the time period determined by the signal parameters. Frequency domain method for the synthesis of the discrete subsectional E-pulse is described in this paper.

The paper is organized as follows. In Section 2, the frequency domain E-pulse method is presented. Section 3 describes the discrete E-pulse synthesis. The model chosen for simulation and the parameter for estimation the identification quality are introduced in Section 4. The results of digital simulation are presented in Section 5. Concluding remarks are drawn in Section 6.

2. Frequency domain E-pulse method

E-pulse is a special waveform which fitted for target response in such a way that its convolution with the response gives zero since the certain moment:

$$c(t) = e(t) \cdot x(t) = 0 \quad t > T_L\,. \qquad (2)$$

There T_L may be chosen equal to zero or positive value reasonably. Frequency domain approach [4] allows the convolution (2) to be written in the form

$$c(t) = \sum_{k=1}^{K} A_k \left|E(s_k)\right| \mathrm{e}^{-\sigma_k t} \cos(\omega_k t + \psi_k), \quad t > T_L\,, \qquad (3)$$

where

$$E(s) = L\{e(t)\} = \int_0^{T_E} e(t) e^{-st} dt \qquad (4)$$

is the Laplace transform of a finite duration ($T_E \leq T_L$) E-pulse waveform, and

$$\psi_k = \varphi_k + \arg\left(E(s_k)\right). \qquad (5)$$

Now, equality $c(t)$ to zero for $t > T_L$ requires:

$$E(s_k) = E(s_k^*) = 0, \quad 1 \leq k \leq K\,. \qquad (6)$$

The expression written above clears the way to various synthesis possibilities. It is enough to set the desired E-pulse waveform with some unknown parameters and in accordance with chosen T_L. Next step is the equation set composition which solution makes all the parameters determined and the E-pulse will consider to be found.

We've tried to analyze (6) itself to state the necessary condition for all synthesized waveform to be E-pulse. Understanding of the E-pulse as a finite duration waveform means that its Laplace transform doesn't consist of any poles and can be generally represented as a polynomial of s. Therefore the values of s making the polynomial $E(s)$ vanish are its roots by definition. Consequently E-pulse indispensable condition is zero arrangement on the s-plane providing its matching with the poles of the target response E-pulse is constructed for:

$$E_{nec}(s) = \prod_{k=1}^{K} (s - s_k)\,(s - s_k^*)\,. \tag{7}$$

But the attempt of utilizing the waveform which Laplace transform includes only the necessary zeroes has no sense because of the inverse transformation of such polynomial (7) contains high order derivatives of delta-function. This case agrees with $T_L = 0$ consequently the application of E-pulse waveform providing $T_L > 0$ is evident. Hence it requires the adding of extra zeroes covered by the specified waveform synthesis scheme chosen to create E-pulse. Different schemes assign different rules for zero addition and make its placing on the s-plane various.

Generally E-pulse can be defined as an arbitrary waveform. However the E-pulse proposes to be expressed as a sum

$$e(t) = \sum_{m=0}^{M} f_m(\alpha_m, t)\,, \tag{8}$$

where $f_m(\alpha_m, t)$ is the mth basis function, α_m describes the function parameters that can vary in order to provide (2), and a number of basis function used to construct the extinction component is defined by M. A very useful application results from using subsectional basis function [8]:

$$f_m(\alpha_m, t) = \begin{cases} g(\alpha_m, t - m\Delta), & m\Delta \le t \le (m+1)\Delta \\ 0, & \text{elswhere,} \end{cases} \tag{9}$$

where $g(t)$ is a Laplace transformable function and Δ is the section width. If $g(t)$ assumes to be delta-function $\delta(t)$ the E-pulse will be written:

$$e_d(t) = \sum_{m=0}^{M} \alpha_m \delta(t - m\Delta)\,. \tag{10}$$

This case corresponds to the degenerate E-pulse that can be considered as a specific model for phenomenon explanation.

For considered poles model (1) the zeroes of $e_d(t)$ can be found:

$$s_{01r} = \sigma_1 + j\frac{2\pi}{\Delta} r, \quad r = 0, \pm 1, \pm 2, \ldots \tag{11}$$

$$s_{0kr} = \sigma_k + j\Big(\frac{2\pi}{\Delta} r \pm \omega_k\Big), \quad k = \overline{2,K} \tag{12}$$

$$\Delta = \frac{p\pi}{\omega_1}, \quad p = 1, 2, \ldots \tag{13}$$

where ω_1 is the maximum of ω_k. This case writes the natural E-pulse described in [5]. Otherwise section width Δ is chosen freely the zeroes are located by

$$s_{0kr} = \sigma_k + j\left(\frac{2\pi}{\Delta} r \pm \omega_k\right), \quad k = \overline{1,K}, \quad r \in Z \tag{14}$$

and such E-pulse is called forced. Natural E-pulse only exists for discrete range of section width Δ while forced E-pulse being doesn't depend on Δ.

The example applied often is the rectangular E-pulse that can be obtained by integrating $e_d(t)$. This case suggests the constant function $g(t) = \alpha$. Then

$$f_m(t) = \begin{cases} \alpha_m, & m\Delta \le t \le (m+1)\Delta \\ 0, & \text{elsewhere.} \end{cases} \tag{15}$$

Since the basis function are defined the equation set can be composed to find the unknown parameters α_m and after it's solved E-pulse will construct.

3. Discrete E-pulse synthesis

The advantage of digital signal processing can be successfully applied for E-pulse technique. Since the sampling procedure leads to mapping s-plane zeroes and poles onto z-plane via

$$z = \exp(pT_s)\,, \tag{16}$$

where T_s is a period of sampling. Now the section width should obviously be equal to integer number of periods T_s. Natural E-pulse zeroes allocation on z-plane can be received by applying the transformation (16) to the expressions (11–13):

$$z_{01r} = \exp(\sigma_1 T_s) \exp\left(j\frac{2\pi}{N_\Delta} r\right), \quad r = 0, 1, \ldots, N_\Delta - 1\,, \tag{17}$$

$$z_{0kr} = \exp(\sigma_k T_s) \exp\left(j\frac{2\pi}{N_\Delta} r\right) \exp(\pm j\omega_k T_s)\,,$$

$$k = \overline{2,K}, \quad r = 0, 1, \ldots, N_\Delta - 1\,, \tag{18}$$

where N_Δ is the width of section in samples.

The expression (17) being demands the sampling frequency to be divisible by natural frequency of any poles:

$$\omega_1 T_s = 2\pi n, \quad n = 1, 2, 3, \ldots \tag{19}$$

So the usage of natural E-pulse in discrete form has the notable difficulties. The sampling frequency can't be surely taken to provide the appropriate section width. Therefore only forced E-pulse should be applied. The expression (16) maps its s-plane zeroes onto z-plane via:

$$z_{0kr} = \exp(\sigma_k T_s)\exp\left(j\frac{2\pi}{N_\Delta}r\right)\exp(\pm j\omega_k T_s),$$
$$k = \overline{1,K},\quad r = 0,1,\ldots,N_\Delta - 1. \tag{20}$$

Figure 1 shows z-plane poles allocation for example while forced E-pulse is constructed for the response that contains only one pair of poles. The section width has chosen to be 3 samples. As follows all zeroes belong to the same pole component lie on the circle symmetrically around the lines divided z-plane into equal parts.

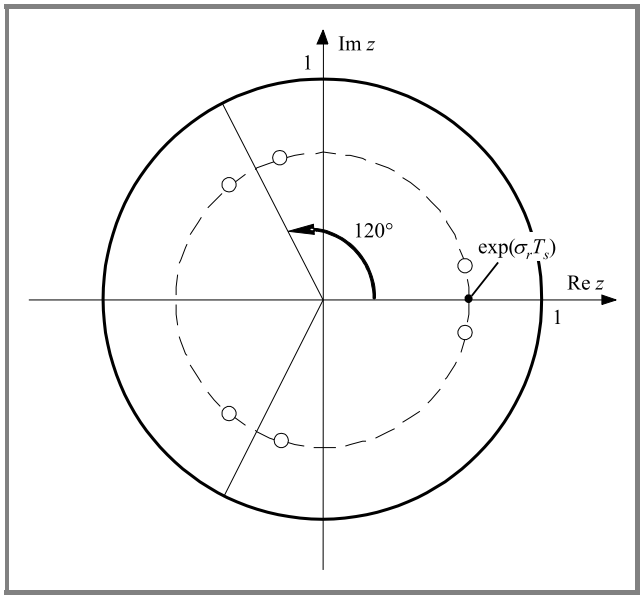


Fig. 1. Discrete E-pulse zeroes allocation on z-plane for one pole discrimination and section width equal to 3 samples.

E-pulse can be represented via z-transform technique directly. Z-transform of the sampled target response $x[n]$ can be written as

$$\widetilde{X}(z) = \frac{L(z)}{P(z)}, \tag{21}$$

where $L(z)$ and $P(z)$ are polynomials of z. Carrying out expression (2) the signal $c[n]$ (as sampled $c(t)$) must be finite, so its z-transform must be free from poles. On the other hand the E-pulse itself is the finite waveform and its z-transform contains no poles:

$$\widetilde{C}(z) = \widetilde{X}(z)\cdot\widetilde{E}(z) = \frac{L(z)\cdot E(z)}{P(z)} = C(z), \tag{22}$$

where $\widetilde{X}(z)$, $\widetilde{E}(z)$, $\widetilde{C}(z)$ are z-transforms of the target response, the E-pulse, fitted to the response, and their convolution correspondingly, and $L(z)$, $E(z)$, $P(z)$, $C(z)$ are z-power polynomials.

It's obviously that expression (21) requires E-pulse to meet the condition:

$$E(z) = P(z)\cdot D(z), \tag{23}$$

where polynomial $P(z)$ coincides with the denominator of z-transform $\widetilde{X}(z)$, and $D(z)$ is a z-power polynomial.

Thus the zeroes of $\widetilde{E}(z)$ should be placed in the same point of the complex plane where the poles of the target response $\widetilde{X}(z)$ lie. However in addition to them E-pulse can also consist extra zeroes, all of them are described by the polynomial $D(z)$. The quality of target discrimination can be improved by optimal allocation of these extra zeroes.

Inverse z-transform of the polynomial $P(z)$ represents the minimal duration basic E-pulse $e_{base}[n]$. In contrast to the continuous this E-pulse is practically realized and can find practical application if discriminated targets poles lie far from each other only. In the case of close allocated target poles discriminating possibilities of this E-pulse is extremely low, so extra zeroes addition is required.

The discussed zeroes allocation (20) meets to the necessary condition while $k = 0$. Inverse z-transform of such the polynomial constructed by these zeroes gives

$$e[n] = \sum_{k=0}^{2K} \alpha_k \delta\left[n - kN_\Delta\right], \tag{24}$$

where K describes the pairs of poles number in target response model, $\delta[n]$ is a discrete delta-function.

More sophisticated E-pulse structure can be reach by using high order polynomial section. In the case of rectangular section the E-pulse determined by the expression (24) should be convolved with rectangular pulse of the N_Δ samples duration. For the application of the higher then the first order base function it's reasonable to use the continuity condition to section border for the waveform and its derivatives [8].

4. Target model and estimation parameter

To make the simulation considerable it's important to choose appropriate target model. We use the model of two aircrafts F-4 and MIG-27 based on three main natural frequencies. The target poles are shown in Fig. 2.

The choice of three main resonances was made on the assumption that they contain the most part of the object response energy. Actually the number of significant poles may exceed several dozens and depends on the target geometry complication.

E-pulse discrimination ratio (EDR) is used for the estimation of discrimination algorithm quality. This param-

eter allows creating the automated target discrimination scheme [7, 8]:

$$EDR_p\ [\text{dB}] = 10 \lg \left(\frac{EDN_p}{\min\limits_p (EDN)} \right), \tag{25}$$

where p describes the number of channel tuned for specified expected target, EDN means E-pulse discrimination number calculated as:

$$EDN_p = \sum_{n=N_L}^{N_L+N_W} c_p^2[n] \Big/ \sum_{n=0}^{N_E} e_p^2[n], \tag{26}$$

where N_L is the time in samples showing the beginning of the late-time part of the convolution received target response with E-pulse and N_W is the measuring interval width, N_E is the E-pulse duration. A priori minimum EDN

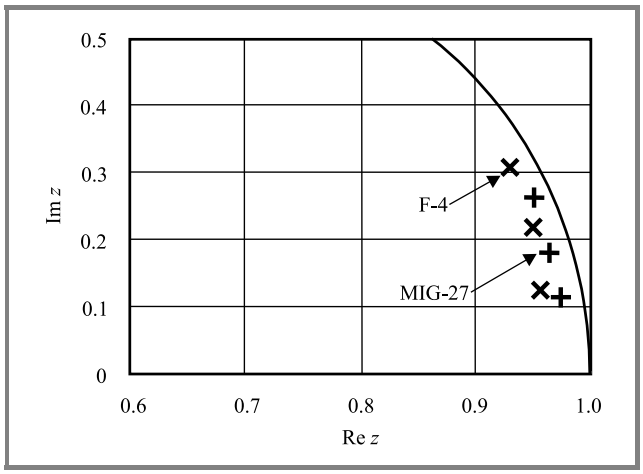


Fig. 2. Complex z-plane plot of aircraft models.

supposes to be in the channel fitted to the expected target since EDR for expected target is identically zero [dB] and called "baseline". The unexpected targets EDRs differ from baseline and the greater exceeding of the baseline demonstrate the better identification possibilities.

5. Digital simulation

In our opinion using the predefined poles model of two aircraft serves the good example for exposure the features of the E-pulse technique.

Power spectra of target responses are shown in Fig. 3. It's obviously that both aircraft response spectra take the wide frequency band.

Pulse response based on constructed E-pulse to annul the scattered signal of F-4 aircraft is shown in Fig. 4.

The basis function has been chosen rectangular and each section duration is equal to 8 samples.

Figure 5 displays the convolution of the F-4 E-pulse with restored responses of the expected target and an unexpected target (MIG-27). Late-time region of the MIG-27 response convolution is visibly distinct from the same region of F-4. However the presence of noise makes this difference unclear like Fig. 6 shows.

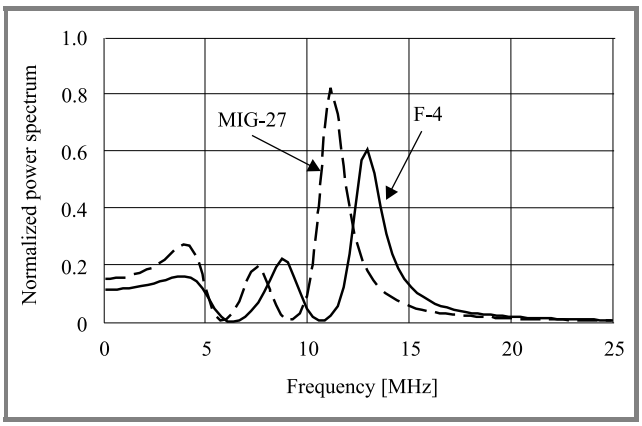


Fig. 3. Power spectrum of aircraft models.

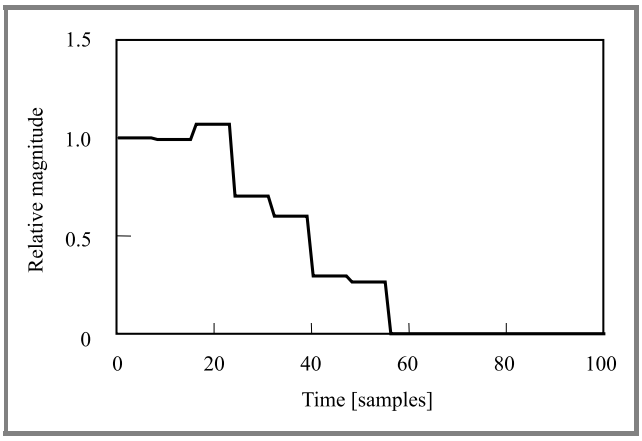


Fig. 4. E-pulse constructed for F-4 aircraft model, the section width is equal to 8 samples.

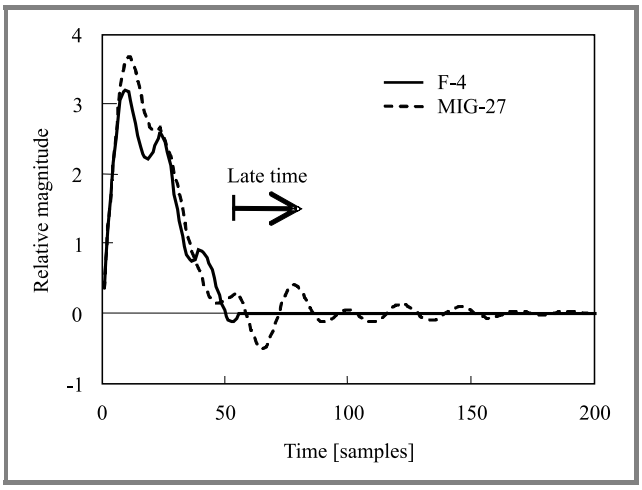


Fig. 5. Convolution of the E-pulse with responses of the expected and an unexpected targets.

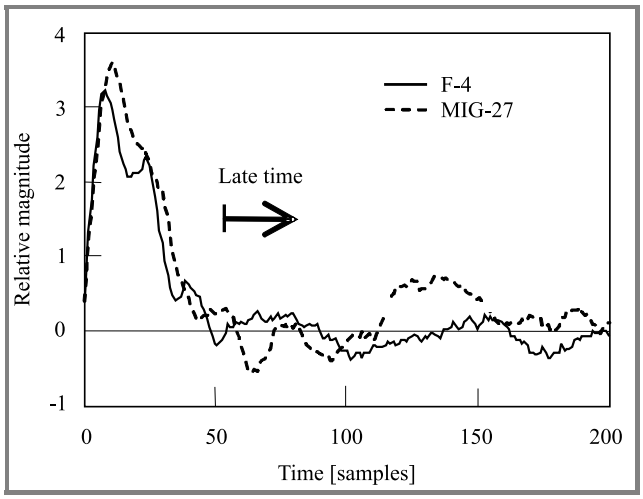


Fig. 6. Convolution of the E-pulse with responses of the expected and an unexpected targets while SNR = 5 dB.

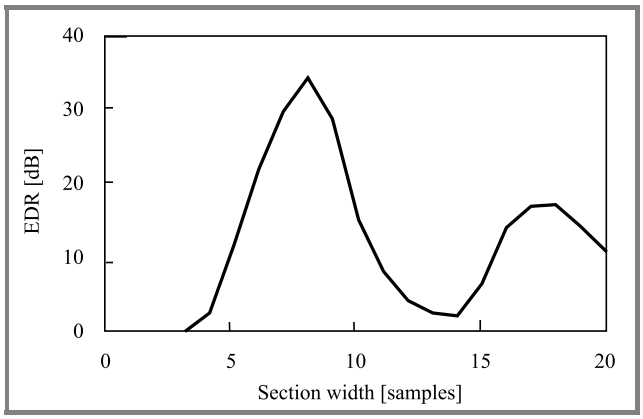


Fig. 7. EDR for rectangular E-pulse against its section width in samples in the presence of noise, SNR = 30 dB.

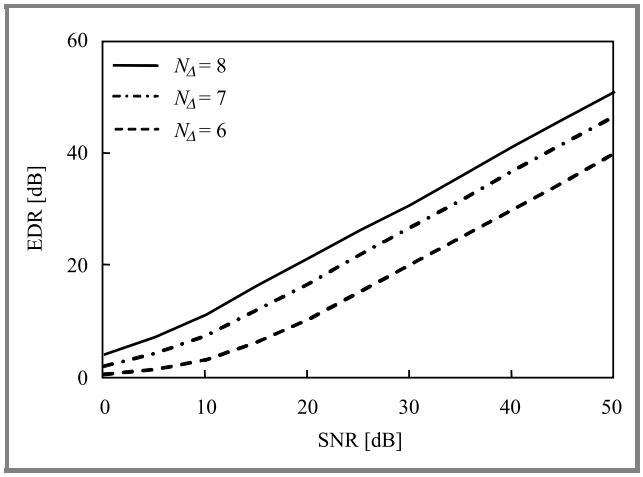


Fig. 8. EDR against SNR for better discrimination capability E-pulses.

The discrete E-pulse application certainly requires determining its duration. Since it can be expressed through the width of the section it's important to choose the width that provides possibly maximum EDR in comparison with others. The results of EDR evaluated for E-pulses which section are measured in samples are shown in Fig. 7. The simulation has been made for additive band-limited Gaussian noise while SNR = 30 dB.

Figure 7 can help to make the decision of E-pulse section width. Obviously that function EDR (N_Δ) has the maximum that corresponds to the section width of 8 samples. The knowledge about the E-pulse section width giving the maximum EDR is able to synthesize the E-pulse having better discrimination capability.

Figure 8 shows the EDRs for the E-pulses with different section width for comparison.

6. Conclusion

Frequency domain approach to E-pulse synthesis can be successfully applied for the resonant model of the complex targets in ultra wideband radar. Based on the known target poles the specified waveform can be constructed for its discrimination. The necessary condition requiring the particular zero allocation for the waveform to be the E-pulse is noticed in the paper.

An attempt to make the proper description of the discrete E-pulse was made. The directly dependence between *z*-plane zeroes arrangement of discrete E-pulse and *s*-plane zeroes arrangement of continuous E-pulse was shown. It described the difficulties of the natural E-pulse usage in discrete time and makes the forced E-pulse to be applied.

Digital simulation was carried out by the example of scaled models F-4 and MIG-27 aircrafts. For the E-pulse effectiveness estimation the EDR parameter was engaged. As its result the width of the E-pulse providing better determination capability in comparison with other was found.

References

[1] C. E. Baum, "The singularity expansion method", in *Transient Electromagnetic Fields*, L. B. Felson, Ed. New York: Springer-Verlag, 1976, pp. 129–179.

[2] A. Baev, Y. Kuznetsov, and V. Chtchekatourov, "Parameter estimation of the resonant model in passive and active radar systems by using third-order statistics", in *29th Eur. Microw. Conf.*, Munich, Germany, 1999, pp. 395–398.

[3] E. Rothwell, K. M. Chen, D. Nyquist, and B. Drachman, "Radar target discrimination using the extinction-pulse technique", *IEEE Trans. Anten. Propagat.*, vol. 33, no. 9, pp. 929–936, 1985.

[4] E. Rothwell, K. M. Chen, and D. P. Nyquist, "Frequency domain E-pulse synthesis and target discrimination", *IEEE Trans. Anten. Propagat.*, vol. 35, no. 4, pp. 426–434, 1987.

[5] Y. Kuznetsov, A. Baev, and R. Sedletskiy, "Application of E-pulse method for remote sensing arbitrary shaped objects in lossy media", in *30th Eur. Microw. Conf.*, Paris, France, 2000, pp. 255–259.

[6] T. Shevgunov and A. Aleksandrov, "Ultra wideband radar targets discrimination using frequency domain E-pulse method", in *15th Int. Conf. Microw. Radar Wirel. Commun. MIKON 2004*, Warsaw, Poland, 2004.

[7] P. Liavasaran, J. Ross, E. Rothwell, K. M. Chen, and D. Nyquist, "Perfonance of an automated radar target discrimination scheme using E-pulse and S-pulse", *IEEE Trans. Anten. Propagat.*, vol. 41, no. 5, pp. 582–588, 1993.

[8] M. Carrió, A. Gallego, J. Portí, and D. Ruiz, "Subsectional-polynomial E-pulse synthesis and application to radar target discrimination", *IEEE Trans. Anten. Propagat.*, vol. 41, no. 9, pp. 1204–1210, 1993.



Andrey V. Aleksandrov was born in Minsk, Byelorussia, on April 4, 1964. He received the M.Sc.E. degree in electrical engineering from the Moscow Aviation Institute (State University of Aerospace Technology), Russia, in 1989. His current research interests deal with system identification, signal processing, and spectral analysis.

e-mail: aaleksan@akc.ru
Theoretical Radio Engineering Department
Flight Vehicle Radio Electronics Faculty
Moscow Aviation Institute (State University of Technology)
Volokolamskoe shosse st 4
A-80, GSP-3, Moscow, 125993, Russia



Timophey J. Shevgunov was born in Moscow, Russia, on May 2, 1983. He entered the Moscow Aviation Institute (State University of Aerospace Technology), Russia, in 1999, and now he's a fifth year regular student. His current research interests deal with system identification, signal processing, and spectral analysis.

e-mail: lorens@online.ru
Theoretical Radio Engineering Department
Flight Vehicle Radio Electronics Faculty
Moscow Aviation Institute (State University of Technology)
Volokolamskoe shosse st 4
A-80, GSP-3, Moscow, 125993, Russia



Andrey B. Baev was born in Moscow, Russia, on December 3, 1975. He received the M.Sc.E. and Ph.D. degrees from the Moscow Aviation Institute (State University of Aerospace Technology), Russia, in 1999, and 2002, respectively, all in electrical engineering. He has worked for the Theoretical Radioelectronics Chair of the Moscow Aviation Institute since 1996. He is currently Associate Professor. His current research interests deal with system identification, signal processing, higher order statistics, and spectral analysis.

e-mail: mai_k405@mtu-net.ru
Theoretical Radio Engineering Department
Flight Vehicle Radio Electronics Faculty
Moscow Aviation Institute (State University of Technology)
Volokolamskoe shosse st 4
A-80, GSP-3, Moscow, 125993, Russia



Yury V. Kuznetsov was born in Kursk, Russia, on December 28, 1951. He received the M.Sc.E. and Ph.D. degrees from the Moscow Aviation Institute (State University of Aerospace Technology), Russia, in 1974, and 1981, respectively, all in electrical engineering. He is the Head of the Theoretical Radioelectronics Chair in Moscow Aviation Institute (State University of Aerospace Technology) from 2001. His current research interests deal with system identification, signal processing, higher order statistics, and spectral analysis.

e-mail: yury_kuznetsov@mtu-net.ru
Theoretical Radio Engineering Department
Flight Vehicle Radio Electronics Faculty
Moscow Aviation Institute (State University of Technology)
Volokolamskoe shosse st 4
A-80, GSP-3, Moscow, 125993, Russia

Paper

Ultra-wideband 3D image processing for improving landmine detection with GPR

Eveline E. Ligthart, Alexander G. Yarovoy, Friedrich Roth, and Leo P. Ligthart

Abstract—This paper describes a new landmine detection algorithm starting from high resolution 3D ground penetrating radar (GPR) images. The algorithm consists of two procedures, object detection and object classification; both strongly depend on the properties of 3D GPR images. The algorithm has been tested on data measured with an ultra-wideband (UWB) video impulse radar (VIR) system developed by the International Research Centre for Telecommunications and Radar (IRCTR). It was found that the algorithm is able to detect all landmines (including difficult to detect M14 mines) and classifies almost all landmines correctly with a large reduction in the number of false alarms caused by clutter. It turns out that for clutter removal it is most effective to eliminate detected objects with a small height.

Keywords— ground penetrating radar, image processing, object detection, classification, clutter removal.

1. Introduction

Improving detectability and decreasing the false alarm rate of a ground penetrating radar (GPR) sensor for landmine detection is the main objective of numerous researches in the past years. Some improvements can be obtained in software processing, particularly for mine detection in GPR images, by optimising image processing techniques. The contribution of this paper lies in reducing the false alarm rate and obtaining a better performance than existing methods in GPR landmine detection.

Earlier research on object detection has been performed. In [1], landmines have been detected using an 2D energy projection of a synthetic aperture radar (SAR) image volume. Also research of object detection and classification of landmines in 2D images has been performed [2]. As for 3D image analysis, only object visualization [3] has been performed. However, to our knowledge landmine detection and classification using the 3D nature of GPR images is new.

The goal of this paper is to describe the developed algorithm that uses specific properties of these images to detect landmines. The algorithm should meet a number of demands:

- All recognizable landmines need to be detected.
- A low number of false alarms is required.
- Multiple 2D images are combined to form 3D images. In the algorithm all actual 3D image information is used for detection and classification.
- The performance of the algorithm should be validated based on actual GPR measurements.

The novelty of this paper is the development of an algorithm, which detect landmines in GPR images using their 3D nature.

In Section 2 the acquisition and preprocessing of the data is described including a short description of its properties. Section 3 presents the detection procedure for 3D GPR images. The classification procedure is addressed in detail in Section 4. The results and a discussion of the performance are given in Section 5. Finally, the paper ends with conclusions and some recommendations in Section 6.

2. Generation of the 3D GPR image and its properties

The measurement campaign for the acquisition of the measurement data [4] was performed on a dry sandy lane at the test facilities for landmine detection systems located at TNO Physics and Electronics Laboratory in The Hague, The Netherlands. During the measurement campaign the GPR system has been mounted on the relocatable scanner of the Delft University of Technology. It scans along one axis measuring A-scans every 1 cm and combines them to B-scans along the other axis with an interval of 1 cm as well. The measured area is 170 cm by 196 cm and 20 cm in depth. Two types of landmine simulants are buried there: PMN mines (metal content, diameter: 11.2 cm) and M14 mines (very low metal content, diameter: 5.6 cm). In total, 12 mines are buried (6 PMN mines and 6 M14 mines) and one unintentionally buried man-made object which radar image has such strong resemblance to that of a landmine that it is also labeled as a wanted target. Further, some false alarms like stones, a bottle and a piece of barbed wire are intentionally buried. All other objects are referred to as clutter and are unwanted in the detection and classification process.

The GPR system that was used to acquire the data is the polarimetric ultra-wideband (UWB) video impulse radar (VIR) system. This system has been developed by IRCTR

and is dedicated to buried landmine detection. The VIR system consists of 2 transmit antennas and 4 receive antennas as seen in Fig. 1. The data is measured in a co-polar antenna combination and with the receive antenna in "monostatic" and in "bistatic" mode. For further information about the VIR system one is referred to [5].

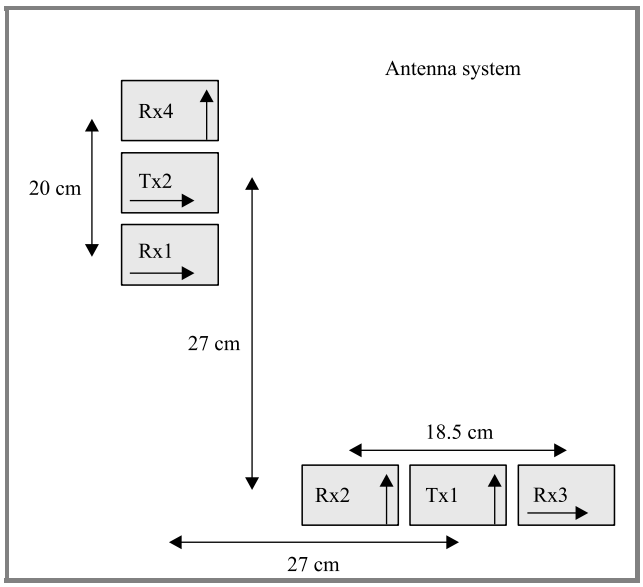


Fig. 1. Top view of the antenna system.

Before image processing is performed, the acquired data have to be preprocessed to remove system instabilities and to reduce clutter. The latter can be obtained by applying SAR processing using a three-dimensional imaging method. All performed preprocessing steps including the 3D imaging method are found in [6].

Properties of 3D radar images of wanted targets that discriminate them from clutter are used for detection and classification of these wanted targets. These are the rotationally symmetric amplitude distribution of wanted target images in horizontal cross section, the high amplitudes and the appearance in many depth slices (the total depth is sampled with a step of 0.25 cm resulting in 80 depth slices).

3. Object detection

Before object detection is applied, the envelope of each A-scan in the 3D image is computed. This is done to eliminate zero crossings and negative amplitudes in the time-domain signal. The phase of the envelope is not used, because such phase analysis (allowing for investigating discontinuities in permittivity) is beyond the scope of this work.

To detect the wanted targets in the 3D image, a threshold procedure is used. Instead of using a fixed threshold procedure, an adaptive threshold technique is used to establish different threshold values for each depth slice of the 3D image. The reason for using different thresholds is that the amount of clutter is much higher in depth slices containing residuals of the ground reflection than in other depth slices and therefore needs a higher threshold value to avoid detection of clutter.

The used adaptive threshold technique is called the decreasing threshold procedure. For each depth slice all possible threshold values are applied. For each threshold value, objects are grouped in the resulting binary depth slice; the number of these detected objects is computed and is plotted against the accompanying threshold value. The resulting curve is different for each depth slice, but it has roughly the same shape (Fig. 2). From experience, it turned out that

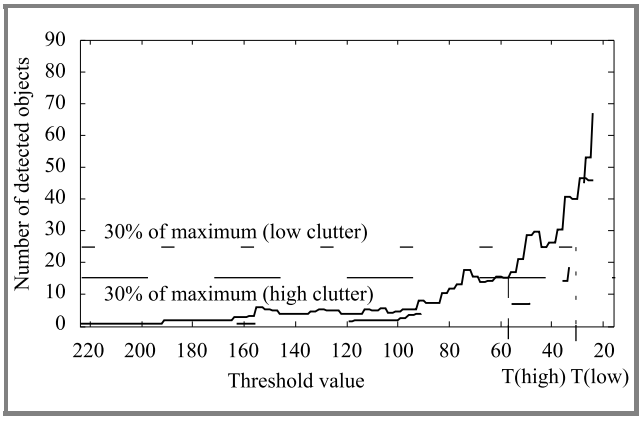


Fig. 2. Number of detected object images versus threshold value. The solid curve represents a depth slice with high amount of clutter, while the dashed curve is the result from a depth slice with low amount of clutter. The horizontal lines represent 30% of the maximum values of the curves with T(high) and T(low) as resulting threshold values.

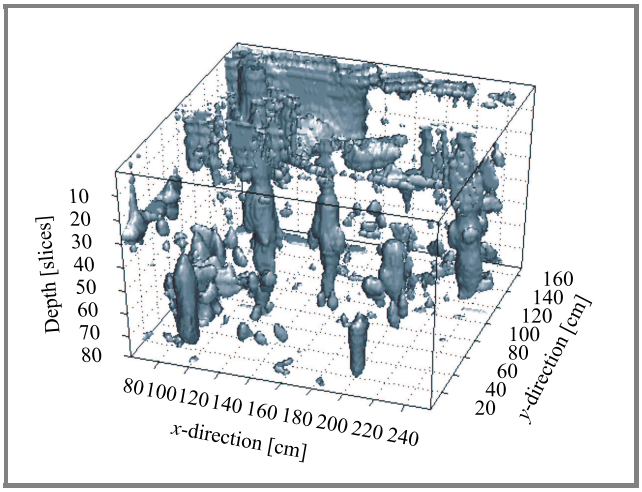


Fig. 3. Binary 3D image volume after threshold procedure.

the best threshold value is situated at the beginning of the steep slope in the curve. This threshold value can be found by calculating a percentage of the maximum number of detected objects in the curve and determine its accompanying threshold value. The choice for this percentage is based on the minimum size of the buried landmines in the measured area and is set to 30% of the maximum of the curve.

In Fig. 2 it is seen that for depth slices with a low amount of clutter the threshold value will be lower than for depth slices with a high amount of clutter.
The 3D binary result after applying the decreasing threshold procedure is shown in Fig. 3. Not only are the wanted targets detected, but also surface clutter and other unwanted objects. It is still difficult to distinguish the wanted targets from these unwanted objects and therefore classification is performed to eliminate the clutter and to obtain a low number of false alarms.

4. Object classification

Classification is based on the established properties of wanted targets. Because it is desirable to remove clutter objects before classification, size based clutter removal (Subsection 4.1) is applied. For classification of all remaining objects (Subsection 4.3), features are extracted from the established properties and selected (Subsection 4.2).

4.1. Size based clutter removal

Based on the dimensions of the wanted targets, two types of object removal are applied: removal of objects with a large horizontal size and removal of objects with a small height.

4.1.1. Removal of objects with a large horizontal size

Especially the residuals from the ground reflection result into detected objects with large horizontal dimensions. These are extremely unwanted for further processing and do not meet the dimension criteria for wanted targets. Therefore, these object images should be removed from the 3D image volume. The removal is performed per depth slice.
An unwanted secondary but slightly acceptable consequence is the possibility that wanted target images merged with clutter images in one or more depth slices are removed as well. To avoid this as much as possible, the horizontal size limit needs to be set with a sufficient margin.

4.1.2. Removal of objects with a small height

The most characteristic property of wanted targets is their appearance in many depth slices. The height of the wanted target images depends on the spatial length of the radar pulse in soil (vertical resolution), the sampling, the depth of the wanted targets (related to the intensity), the physical height of the wanted targets and the chosen threshold value for object detection.
The removal of object images with small height is performed by taking image slices in vertical directions along the *x*- and *y*-direction respectively and removing all objects smaller than an established height limit. This height limit is based on the height of the smallest and weakest wanted target image in the data.

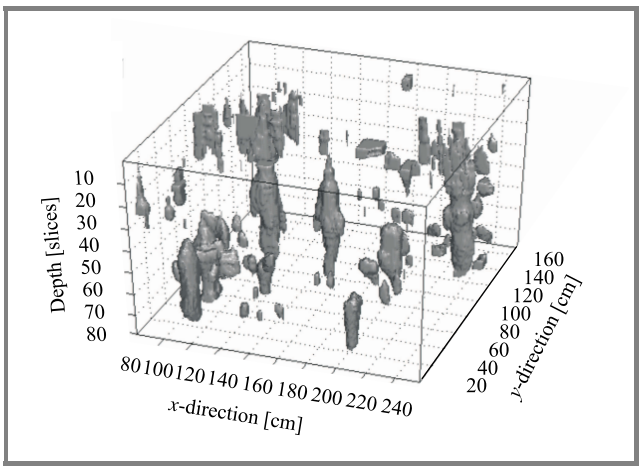


Fig. 4. Binary 3D image volume after size based clutter removal.

The overall result after the size based clutter removal is shown in Fig. 4, where the amount of detected clutter objects is decreased by 70% from 351 to 112 objects.

4.2. Feature extraction

Feature extraction is a preparatory step for the classification of the detected object images and has a big influence on the distinction of wanted target images from clutter images.
The features are divided into four categories: statistical, structure-, shape- and size-based features. Due to the earlier performed size-based clutter removal no features have been selected from the last category. The statistical and structure-based features are computed from intensity images and therefore require a 3D window to be placed around the detected objects [7]. The shape based features are computed from binary images.
The quality of a feature depends on its discriminating power, reliability and independency with other features. Based on these criteria, nine features (F_1 to F_9) are determined to be used in the feature selection:

Statistical based features

F_1 maximum intensity

F_2 ratio of mean over maximum intensity

F_3 ratio of minimum over maximum intensity

F_4 standard deviation

Structure based features

F_5 similarity with a template

F_6 similarity between orthogonal horizontal cross lines

F_7 depth similarity

Shape based features

F_8 eccentricity of the bounding ellipse

F_9 ratio of minor axis over major axis lengths

4.3. Classification

To limit the computational time, the best performing features of the total feature set are selected (with the so-called forward feature selection method [8]) to be used in the classification process.

The classifier is based on a simple classification rule. For testing of the classification routine the leave-one-out method is used to obtain training and test sets from the feature set without having a large amount of objects in this feature set. The classification boundary is calculated from the training set, which is then used to decide whether a test object is a wanted target or a clutter object. To minimize the risk of having a missed detection, the boundary is computed with a certain safety margin, which is 5% of the overall maximum value of the specific feature added to the boundary. In Fig. 5 scatter plots for two features are plotted including the computed boundaries, showing that the boundaries eliminate many clutter objects.

The selected feature set contains 5 features. These are: the maximum intensity (F_1), because wanted target reflections exhibit high amplitudes; the ratio of the mean over the maximum intensity (F_2); similarity with a template (F_5), where the template is a representative horizontal cross section of one of the wanted target images; similarity between orthogonal horizontal cross lines (F_6), because of the rotationally symmetric amplitude distribution of wanted target images in horizontal cross section; and the ratio of the length of the minor axis over that of the major axis (F_9), also because of the circular shape of the wanted target images.

After classification, 20 false alarm objects retain in the image volume as can be seen in Fig. 6. This corresponds to a clutter reduction of more than 80%.

Because of the limited down-range resolution, it is not possible to have two distinctive landmine reflection events in a depth range of 20 cm which are situated closer than the smallest possible distance between two landmines. Therefore, these object images have to be merged into one object image.

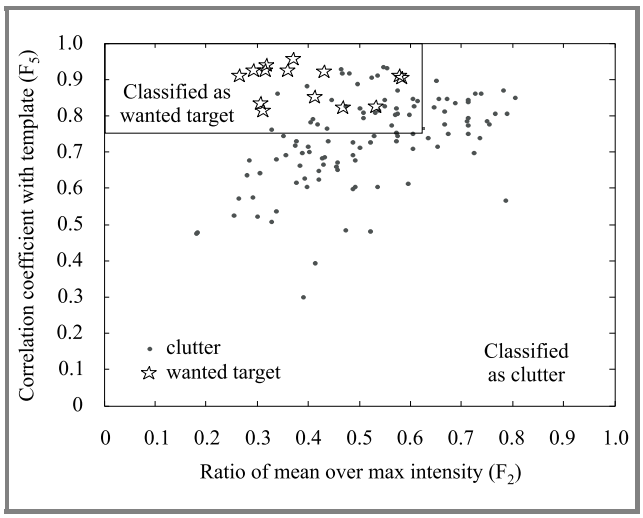


Fig. 5. Scatterplot of feature F_2 and F_5 including the classification boundary.

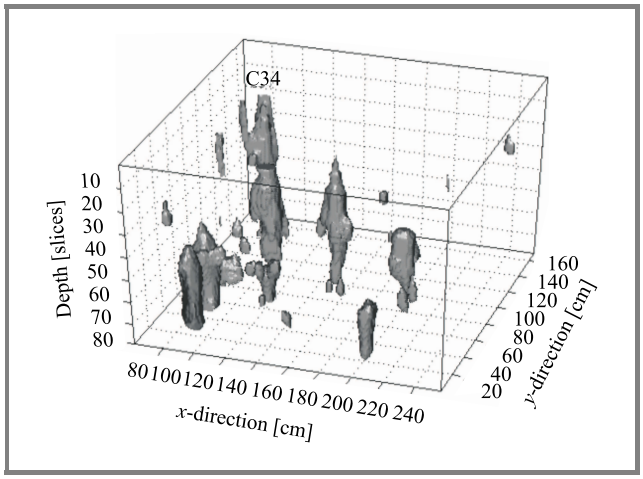


Fig. 6. Binary 3D image volume after classification.

5. Performance of the algorithm

Besides the requirement that 100% of all wanted targets have to be detected, the algorithm has to meet also another requirement which is the low amount of false alarms. In Fig. 7 the clutter reduction for each image processing procedure of the algorithm is shown. It is remarkable that the largest reduction of clutter is achieved by applying a size-based clutter removal; that is, the removal of objects with a small height (procedure *b*). The increase in amount of clutter objects in procedure a is due to division of objects into more objects by removing parts of objects with a large horizontal size per depth slice.

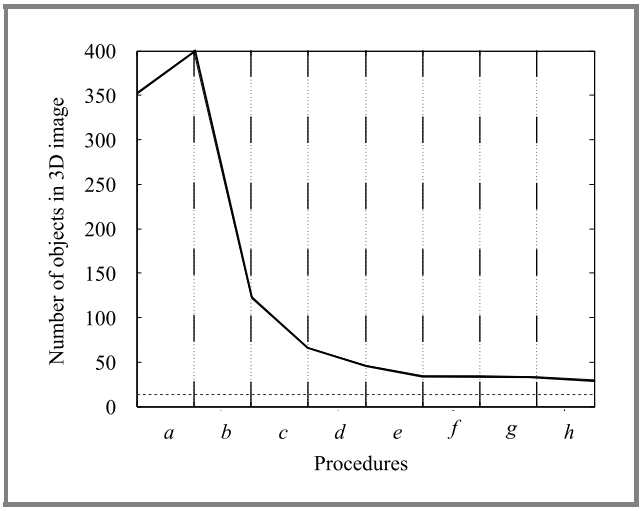


Fig. 7. Reduction of the amount of object images per procedure (solid line). The dashed line represents the number of the buried landmines in the test-lane area. Procedures are: *a*, *b* – size based clutter reduction; *c*, *d*, *e*, *f*, *g* – classification performance per feature; *h* – merging of objects due to down-range resolution.

The results of the classification method are shown in the confusion matrix of Table 1. It demonstrates that for

this 3D image the amount of clutter images classified as wanted targets (false alarms) has been drastically reduced to 18 including a positive detection of 12 wanted targets. All small M14 mines are classified as wanted target. The missed detection is an "easy to detect" PMN mine, which is situated close to the border of the measurement test-lane area. The misdetection is caused by incorrect SAR processing, which resulted in an oval shape for the landmine in horizontal cross section instead of a circular shape. For correct SAR processing some defined space around object images is required, which is not the case for objects situated near the border of the test lane area. This problem will be solved when the measurement area has an overlap with its neighboring measurement areas in such a way that incorrect SAR processing can be avoided.

Table 1
Confusion matrix of the classification results

Clutter	Classifier-determined label target	Classifier-determined label clutter
True wanted target	12	1
True clutter	18	93

The above reported results are obtained by using the leave-one-out-method to create larger training sets, but a consequence is that the test sets are not completely independent from the training sets. Therefore, the reliability of the established classification boundaries is tested with data from the other transmitting and/or receiving antennas. In total, 3 test sets are used; one where the receive antenna is also in "monostatic" mode as is the case for the training data and two sets with the receive antenna in "bistatic" mode. The results are put in confusion matrices, which are shown in Table 2.

Table 2
Confusion matrices for other transmitter/receiver combinations; transmit/receive numbering as indicated in Fig. 1

Bistatic mode Tx1Rx4		
Clutter	Classified wanted target	Classified clutter
True wanted target	2	5
True clutter	11	95
Monostatic mode Tx2Rx1		
Clutter	Classified wanted target	Classified clutter
True wanted target	7	1
True clutter	13	53
Bistatic mode Tx2Rx3		
Clutter	Classified wanted target	Classified clutter
True wanted target	7	3
True clutter	28	113

It can be seen that the classification results for the transmitter/receiver combinations in "bistatic" mode are worse than those for the "monostatic" mode. The large number of missed detections for "bistatic" mode has two main reasons. First of all, in "bistatic" mode the reflections are weaker. Therefore, classification which is partly based on intensity values of the object images causes more missed detections. Secondly, due to the large distance between the transmit and receive antenna in "bistatic" mode, the landmines are tilted with respect to the vertical direction. Therefore, the wanted target images do not fit the 3D window nicely anymore, which results in a larger number of missed detections.

The transmitter/receiver combination in "monostatic" mode of Table 2 has a reasonably low number of false alarms and almost all wanted targets are classified correctly. The reason for the one missed detection is its weak reflections. To conclude, the data measured in "monostatic" mode gives better results and satisfies the established classification boundaries more.

In view of the obtained results, we have to take into account that the data were measured over a fixed type of ground with two types of buried mines. When measuring over a lossy type of ground, the results probably will deteriorate.

Besides the circular shape of the buried landmines, other shapes are possible. This may change the properties of the landmine images. Consequently, in this case the features that are used in the here-presented classification scheme will probably not act properly, causing the performance of the classification procedure to degrade.

The size of the measured area also influences the performance of the procedures. Measuring a larger area results in more objects and therefore in a larger training set.

Points for improvement in the overall landmine detection procedure are the adaptive thresholding technique, the 3D window used in the classification procedure and the classification procedure itself.

6. Conclusions and recommendations

An algorithm for GPR landmine detection has been developed, where full use is made of the 3D nature of GPR images. It consists of two procedures: object detection based on a self-developed adaptive thresholding technique and object classification using a simple classification routine designed to reduce the possibility of missed detections. This algorithm has been realized, tested and validated.

Landmine detection in 3D GPR images gives promising results. All M14 mines are detected and classified as wanted target. Only one large PMN mine is misclassified due to incorrect SAR processing at the border of the measurement area. The removal of objects with a small height proves to be a good procedure to eliminate clutter from the image volume. However, we have to implement this procedure with care to avoid that small and deeply buried landmines are removed.

The now-available object detection procedure also needs an expert decision; however in future this decision could be determined by the size and possible depth of the buried landmines.
The classifier in the object classification procedure is quite simple, but effective. When paying more attention to the selection of the classification method, it might be better to use a neural network as classifier, which "learns" to separate landmines from clutter based on their radar images.
The performance of a landmine detection system is also improved sensor fusion. Merging different sensors like the metal detector, the infrared detector and GPR into one landmine detection system [2] leads to the necessary further development of algorithms with improved performance.

References

[1] A. G. Yarovoy, V. Kovalenko, F. Roth, L. P. Ligthart, and R. F. Bloemenkamp, "Multi-waveform full-polarimetric GPR sensor for landmine detection: first experimental results", in *Int. Conf. Requir. Technol. Detect., Remov. Neutr. Landm. UXO*, Brussels, Belgium, 2003, pp. 554–560.

[2] F. Cremer, W. de Jong, and K. Schutte, "Fusion of polarimetric infrared features and GPR features for landmine detection", in *2nd Int. Worksh. Adv. GPR*, Delft, The Netherlands, 2003, pp. 222–227.

[3] L. Zanzi, M. Lualdi, H. M. Braun, W. Borisch, and G. Triltzsch, "An ultra high frequency radar sensor for humanitarian demining tested on different scenarios in 3D imaging mode", in *9th Int. Conf. Ground Penetr. Radar, Proc. SPIE*, vol. 4758, pp. 240–245, 2002.

[4] A. G. Yarovoy, V. Kovalenko, F. Roth, J. van Heijenoort, P. Hakkaart, W. de Jong, F. Cremer, J. B. Rhebergen, P. J. Fritz, M. A. Ouwens, and R. F. Bloemenkamp, "Multi-sensor measurement campaign at TNO-FEL test lanes in July 2002", in *Int. Conf. Requir. Technol. Detect., Remov. Neutr. Landm. UXO*, Brussels, Belgium, 2003, pp. 208–215.

[5] A. G. Yarovoy, L. P. Ligthart, A. Schukin, and I. Kaplun, "Polarimetric video impulse radar for landmine detection", *Subsurf. Sens. Technol. Appl.*, vol. 3, no. 4, pp. 271–293, 2002.

[6] J. Groenenboom and A. G. Yarovoy, "Data processing and imaging in GPR system dedicated for landmine detection", *Subsurf. Sens. Technol. Appl.*, vol. 3, no. 4, pp. 387–402, 2002.

[7] E. E. Ligthart, "Landmine detection in high resolution 3D GPR images", M.Sc. thesis, Delft University of Technology, Faculty of Electrical Engineering, Mathematics and Computer Science, Delft, The Netherlands, 2003.

[8] A. R. Webb, *Statistical Pattern Recognition*. London: Hodder, Arnold, 2001.



Eveline E. Ligthart was born in Leiden, The Netherlands, on February 18, 1979. She received the M.Sc. degree in electrical engineering from the Delft University of Technology, The Netherlands, in March 2004. The present paper is part of her graduation thesis "Landmine detection in high resolution 3D GPR images" performed at the International Research Centre for Telecommunications and Radar (IRCTR). At present, she is a pattern recognition scientist at Prime Vision in Delft, The Netherlands. Her work includes the recognition of postal addresses and license plates.

e-mail: E.Ligthart@PrimeVision.com
International Research Centre
for Telecommunications and Radar (IRCTR)
Faculty of Electrical Engineering,
Mathematics and Computer Science
Delft University of Technology
Mekelweg st 4
2628 CD Delft, The Netherlands



Alexander G. Yarovoy graduated from the Kharkov State University, Ukraine, in 1984 with the diploma with honor in radio physics and electronics. He received the Cand. phys. and math. sci. and Dr. phys. and math. sci. degrees (all in radio physics) in 1987 and 1994, respectively. In 1987 he joined the Department of Radiophysics at the Kharkov State University as a Researcher and became a Professor there in 1997. From September 1994 through 1996 he was with Technical University of Ilmenau, Germany, as a Visiting Researcher. Since 1999 he is with the International Research Centre for Telecommunications and Radar (IRCTR) at the Delft University of Technology, The Netherlands, where he coordinates all GPR-related projects. Currently his main research interests are in ultra-wideband technology including radars and in applied electromagnetics.

e-mail: A.Yarovoy@EWI.TUDelft.nl
International Research Centre
for Telecommunications and Radar (IRCTR)
Faculty of Electrical Engineering,
Mathematics and Computer Science
Delft University of Technology
Mekelweg st 4
2628 CD Delft, The Netherlands



Friedrich Roth was born in Munich, Germany, in 1972. He received a M.Sc. degree in geophysics from the Colorado School of Mines (CSM), USA, in 1999. While at CSM, he studied the possible use of inertial navigation for real-time antenna position and orientation estimation for ground penetrating radar data acquisition. Since 2000 he has been a Ph.D. student at the International Research Centre for Telecommunications and Radar (IRCTR) at the Delft University of Technology, The Netherlands, working on landmine detection problems. His current research interests include electromagnetic scattering

from buried landmines, deconvolution and target identification, GPR polarimetry, and real-time data processing.
e-mail: FRoth@Clamart.oilfield.slb.com
International Research Centre
for Telecommunications and Radar (IRCTR)
Faculty of Electrical Engineering,
Mathematics and Computer Science
Delft University of Technology
Mekelweg st 4
2628 CD Delft, The Netherlands



Leo P. Ligthart was born in Rotterdam, the Netherlands, on September 15, 1946. He received an engineer's degree (*cum laude*) and a Doctor of technology degree from Delft University of Technology in 1969 and 1985, respectively. He is Fellow of IEE and IEEE. He received doctorates (*honoris causa*) at Moscow State Technical University of Civil Aviation in 1999 and Tomsk State University of Control Systems and Radioelectronics in 2001. He is academician of the Russian Academy of Transport. Since 1988, he has held the chair of Microwave Transmission, Radar and Remote Sensing in the Faculty of Electrical Engineering, Mathematics and Informatics, Delft University of Technology. In 1994, he became Director of the International Research Centre for Telecommunications and Radar. Prof. Ligthart's principal areas of specialization include antennas and propagation, radar and remote sensing, but he has also been active in satellite, mobile and radio communications. He has published over 350 papers and 1 book.
e-mail: L.P.Ligthart@IRCTR.TUDelft.nl
International Research Centre
for Telecommunications and Radar (IRCTR)
Faculty of Electrical Engineering,
Mathematics and Computer Science
Delft University of Technology
Mekelweg st 4
2628 CD Delft, The Netherlands

Paper

Analysis of errors in on-wafer measurements due to multimode propagation in CB-CPW

Arkadiusz Lewandowski and Wojciech Wiatr

Abstract—We study for the first time errors in on-wafer scattering parameter measurements caused by the parasitic microstrip-like mode propagation in conductor-backed coplanar waveguide (CB-CPW). We determine upper bound for these errors for typical CPW devices such as a matched load, an open circuit, and a transmission line section. To this end, we develop an electromagnetic-simulations-based multimode three-port model for the transition between an air-coplanar probe and the CB-CPW. Subsequently, we apply this model to examine errors in the device *S* parameters de-embedded from measurements affected by the parasitic MSL mode. Our analysis demonstrates that the multimode propagation in CB-CPW may significantly deteriorate the *S*-parameters measured on wafer.

Keywords*— *on-wafer measurements, multimode propagation, error analysis, conductor-backed coplanar waveguide (CB-CPW), microstrip-like mode, numerical electromagnetic analysis, on-wafer probe, calibration, de-embedding, monolithic microwave integrated circuit (MMIC).

1. Introduction

The advent of a new wafer-level measurement technology, the on-wafer microwave probing [1], has resulted in proliferation of the coplanar waveguide (CPW) as a basic transmission medium for connecting dies with standard measurement instrumentation through microwave coplanar probes. Although this technology greatly alleviates on-wafer measurements of monolithic microwave integrated circuits (MMICs), it also brings about fresh metrology problems. Some of the problems result from the fact that in typical measurement configurations the CPW becomes an overmoded transmission line. This is due to the fact that, besides the three strips placed on the upper substrate side, the CPW comprises usually a backside metallization plane, which is either plated on the substrate or introduced by the chuck of the on-wafer measurement station [1]. Such a four conductor CPW structure is called a conductor-backed coplanar waveguide (CB-CPW) and in general supports three modes [1, 2]: a coplanar mode (CPW), a slot-line mode (SLM) and a microstrip-like mode (MSL), which is also referred to as a parallel-plate mode [3]. Since both CB-CPW structures and microwave coplanar probes contacting them usually maintain symmetry, the slot-line mode is virtually not excited and therefore is not considered in this work. Of the two remaining modes, CPW is the desired one that usually dominates over the parasitic MSL mode.

There are two basic approaches to the moding in the CB-CPW: the conventional one neglecting undesired modes and using an approximate single-mode representation, and the complete one taking into account all modes. The former utilizes the well-known circuit theory methods [4], stemming from the assumption of the single mode propagation, while the later refers to a more general multimode waveguide circuit theory [5], at an expense, however, of a higher complexity. With a constant increase of the maximum frequency of MMICs, the accuracy of the conventional approach becomes insufficient for a fast and effective design of high-speed electronic circuits which is essential for shortening time-to-market and reducing costs. Therefore, one needs novel circuit analysis and measurement characterisation methods that take into account the multimode propagation effects in MMIC structures.

A general theoretical basis for multimode waveguide circuit theory methods has already been laid in [4, 5]. Furthermore, numerical electromagnetic (EM) 3D simulation techniques, that have rapidly advanced in the last few years, have been successfully applied in the analysis of the propagation and excitation properties of the MSL mode, as well as means of its suppression [2, 3, 6–9].

However, as regards the on-wafer metrology, there have been only a few works dealing with the influence of the parasitic MSL mode on the measurement accuracy of CB-CPW based structures. Potential errors in the on-wafer multiline-TRL calibration [10] on the CB-CPW are mentioned in [11]. A trial to quantify these errors in case of the TRL calibration [12] is presented in the previous conference paper of the authors [13].

The aim of this work is to fill up this gap by presenting a systematic analysis of errors occurring in the measurements of CB-CPW based structures due to the presence of the parasitic MSL mode. The topic is a continuation of [13]. Here, we study first multimode excitation in a transition between an air-coplanar probe and a CB-CPW line using 3D EM simulations, and then model this transition with a multimode three-port scattering matrix. In the next step, we use this model to examine some exemplary one- and two-port CB-CPW structures and determine errors in the conventional single-mode approach arising due to the presence of the parasitic MSL mode. Results show that these errors may be significant.

2. Multimode excitation in an air-coplanar-probe-to-CB-CPW transition

In general, a microwave coplanar probe has a very complicated design, optimized in terms of low insertion and return loss, as well as low radiation [1]. Accurate modelling of all probe's characteristics is thus a very tedious and time consuming task. However, considering excitation of the parasitic MSL mode, the most important part of the probe is the discontinuity arising at the contact between the probe-tip and the CPW transmission line.

A simplified analysis of this excitation may be performed using approaches that rely on the mode matching technique applied to the quasi-static description of both modes in terms of modal voltages and currents [2, 3]. Although these methods are particularly useful for understanding the MSL mode excitation phenomena, their feasibility is limited to simple discontinuities and low frequencies, for which dispersion effects are negligible [6]. Therefore an exact analysis of the MSL mode excitation calls for numerical EM simulations.

Taking this into account, we construct a model of the probe depicting fairly well the probe-tip and investigate multimode excitation at the probe-tip discontinuity using numerical EM simulations. A view of the probe model placed over a section of the CB-CPW is shown in Fig. 1. The picture presents only a half of the whole symmetric structure which has been split with a magnetic wall along the center of the signal strip in order to reduce the analysis time.

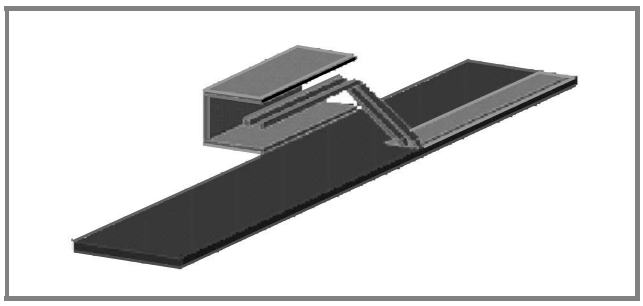


Fig. 1. A half-view of the air-coplanar-probe-to-CB-CPW transition.

The probe consists of two parts: a simplified launching section and a precisely modelled contacting part. The launching section comprises an air CPW surrounded by a rectangular waveguide, while the contacting section consists of an air-coplanar line declining at an angle to the substrate and ending with a contacting tip. The probe tip has dimensions of a real microwave probe: pitch of 150 μm, center conductor width of 50 μm, and contact length of 50 μm.

In our analysis, we consider typical lines on an alumina substrate used mainly for manufacturing of impedance standard substrates (ISS), and lines on a typical MMIC GaAs substrate. Their dimensions, given in Table 1, were chosen to provide 50 Ω characteristic impedance for the CPW mode.

Table 1

Parameters of lines used in the EM simulation: w – centre strip width, s – slot width, w_g – ground strip width, h – substrate height, and ε_r – relative dielectric permittivity

Line	h [μm]	ε_r	w [μm]	s [μm]	w_g [μm]
ISS	635	9.9	50	25	250
GaAs	100	12.95	50	48	250

We performed the EM simulations with the QuickWave software package, employing the method of finite-differences in time-domain (FDTD) [14]. At first we determined field distributions and dispersion characteristics of the CPW and MSL modes for both substrates in the frequency range from 5 to 15 GHz. Figure 2 shows the effective dielectric permittivity of both modes. In each case, the effective permittivity of the CPW mode does not depend

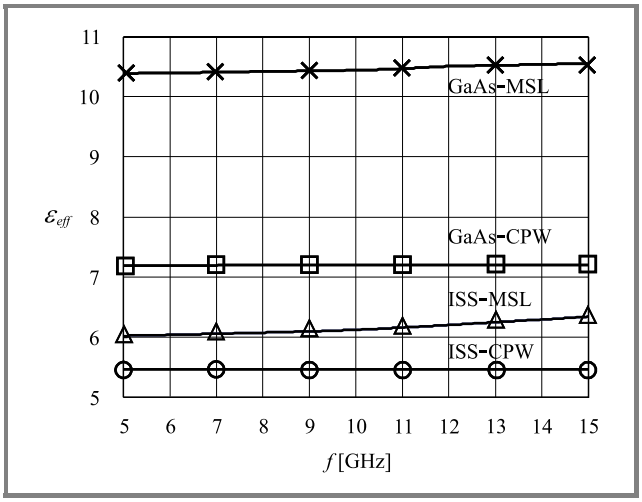


Fig. 2. Effective permittivity for the CPW and MSL mode in ISS, and the CPW and MSL mode in GaAs.

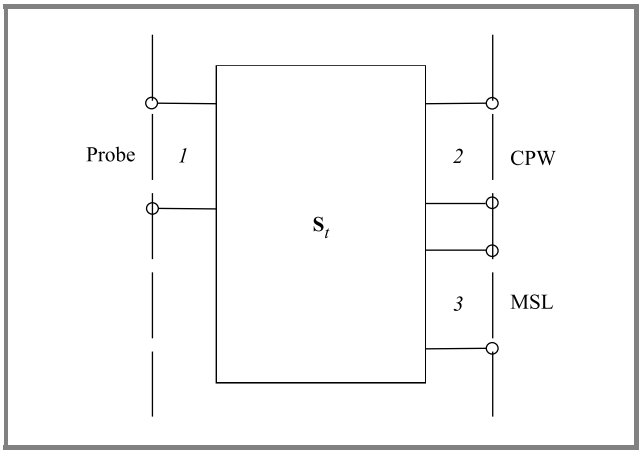


Fig. 3. Three-port model of the transition represented with a scattering matrix $\mathbf{S}_t$.

on frequency, while the effective permittivity of the MSL mode is higher and its slope reveals a small dispersion.

Next, we analysed electrical properties of the transition determining its multimode scattering matrix $\mathbf{S}_t$. Figure 3 shows the three-port model of the transition, in which port *1* is associated with the probe's launching part, while ports *2* and *3* correspond to the CPW and MSL modes, respectively. In the simulation their reference planes were placed at the end of the CB-CPW line to prevent coupling through higher order modes. After the simulation the reference planes have been shifted down to the probe tip to account for the electrical properties of the transition itself.

Figure 4 shows magnitude of the scattering parameters S_{21} and S_{31}, representing transmission for the CPW and MSL mode, respectively. The graphs demonstrate a significant signal transmission on the MSL mode for both substrates, which is slightly higher for the GaAs substrate because of thinner substrate in comparison to the total line width [2].

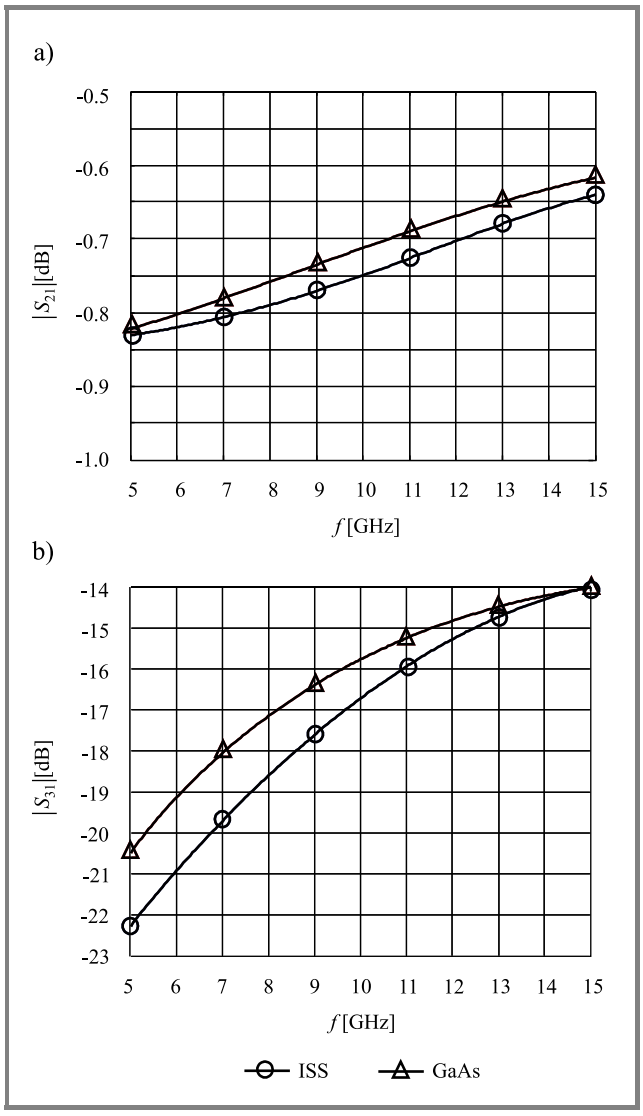


Fig. 4. Scattering parameters (a) S_{21} and (b) S_{31} of the transition between an air-coplanar probe and the CB-CPW on the ISS and GaAs substrate.

3. Errors in measurements of typical devices

When measuring CB-CPW devices, one is usually interested in device parameters for the CPW mode. Consequently, the conventional device measurement is based on neglecting the MSL mode and employing a single-mode device description. In this approach, the device under test (DUT) is modelled as a linear two-port embedded into a cascade of two other linear two-ports representing systematic measurement errors [1]. Thus, the conventional *S*-parameter measurement procedure relies on removing the errors from the DUT measurements and is performed in two steps: probe calibration[1] and device de-embedding [1].

The probe calibration is based on measuring several known devices to determine the systematic errors introduced by the probes. For this purpose, diverse calibration methods are applied, among which SOLT, LRRM [15], and various versions of TRL [10, 12] are the most frequently used [1]. After the calibration, the parameters of both embedding two-ports, each representing the relevant probe, are known and their effect on the measurement can be easily removed in the de-embedding procedure basing on the conventional single-mode waveguide circuit theory [4].

However, this straightforward conventional approach may introduce some errors when the single-mode assumption is not met. In the reality, the CPW mode is accompanied by the parasitic MSL mode and they both simultaneously contribute to the measured signal [5]. If the effect of the MSL signal is not negligible, multimode errors emerge in the DUT *S*-parameters.

To assess these errors, we mimic the conventional approach employing, however, the multimode matrix $\mathbf{S}_t'$ of the probe-to-line transition. We perform our study in two steps, first analysing the calibration procedure, and then the device de-embedding.

Since in the conventional approach probes are represented by two-ports, application of the single-mode calibration procedure to the multimode case leads to a reduction of three-port matrix $\mathbf{S}_t$ to a two-port matrix $\mathbf{S}_t'$. Such a reduction can be carried out uniquely when all measured CPW devices exhibit the same reflection coefficient for the MSL mode. However, if it is not the case, this reduction is ambiguous, and matrix $\mathbf{S}_t'$ strongly depends on the type of standards employed in the calibration [13]. Therefore, to avoid such problems in the calibration, we assume to deal with an ideal case, i.e., when the MSL mode is suppressed and all energy is transmitted over the CPW mode. Such a situation approximately takes place for thick substrates and may be arranged in practice by inserting an additional thick dielectric layer between the CPW substrate without backside metallisation and the chuck [2]. The characteristic impedance for the MSL mode becomes then very high in comparison to the CPW mode, which is equivalent

[1]For the sake of simplicity we assume here that the vector network analyzer (VNA) has been calibrated at the coaxial reference planes.

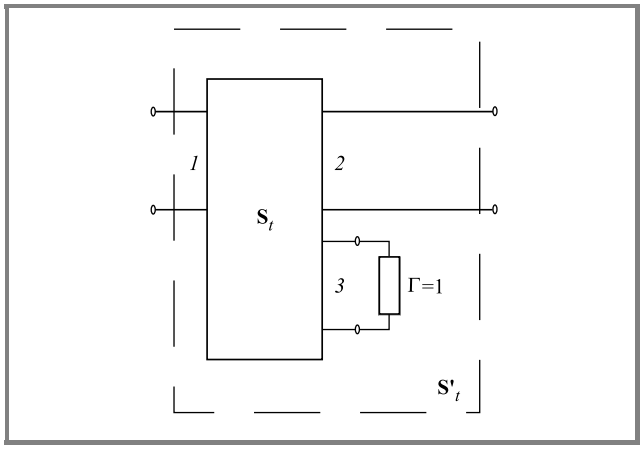


Fig. 5. Reduction of the three-port to a two-port model.

to attaching an open circuit at the MSL mode port of the three-port as shown in Fig. 5. Consequently, the determination of the matrix $\mathbf{S}'_t$, representing the systematic measurement errors of the probe, becomes straightforward.
Having calculated the matrix $\mathbf{S}'_t$, we are able to simulate the de-embedding of multimode measurements for one-port and two-port devices whose parameters for CPW are assumed to be known. To study the errors, we simulate the measurement results using the three-port model with some general assumptions regarding properties of the MSL circuit. The errors are defined as a deviation of the de-embedded *S*-parameters in reference to the parameters assumed for the CPW mode. Two next subsections present results of the error analysis for a matched load and an ideal open circuit, as exemplary one-port devices, and a CB-CPW transmission line section with a varying length, as a two-port device.

3.1. Matched load and ideal open circuit

We analyse multimode propagation errors in measurements of a matched load and an ideal open circuit by investigating the influence of different loading conditions for the MSL mode. The basic idea of our approach is depicted in Fig. 6.
For a CPW device with a reflection coefficient Γ_{CPW} we measure a reflection coefficient Γ_m, which is different from Γ_{CPW} because of the systematic errors brought in by the probe and the contribution of the MSL mode, represented by the variable reflection coefficient Γ_{MSL}. From Γ_m we de-embed the reflection coefficient Γ'_{CPW} using the single-mode description $\mathbf{S}'_t$ of the probe and employing the relationship:

$$\Gamma'_{CPW} = \frac{\Gamma_m - S'_{t11}}{S'_{t22}\Gamma_m - \det \mathbf{S}'_t}. \qquad (1)$$

We seek for bounds of Γ'_{CPW} deviations from the true value, Γ_{CPW}, considering dependence of Γ'_{CPW} on Γ_{MSL} under the condition of passiveness of the later $|\Gamma_{MSL}| \leq 1$.

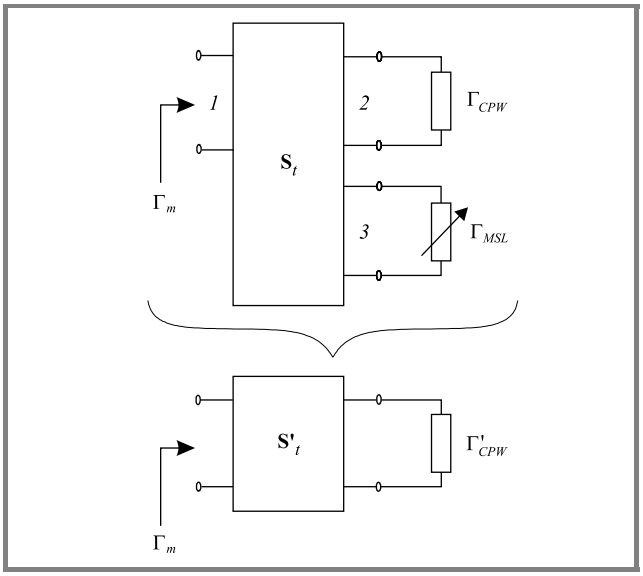


Fig. 6. Analysis method for one-port devices.

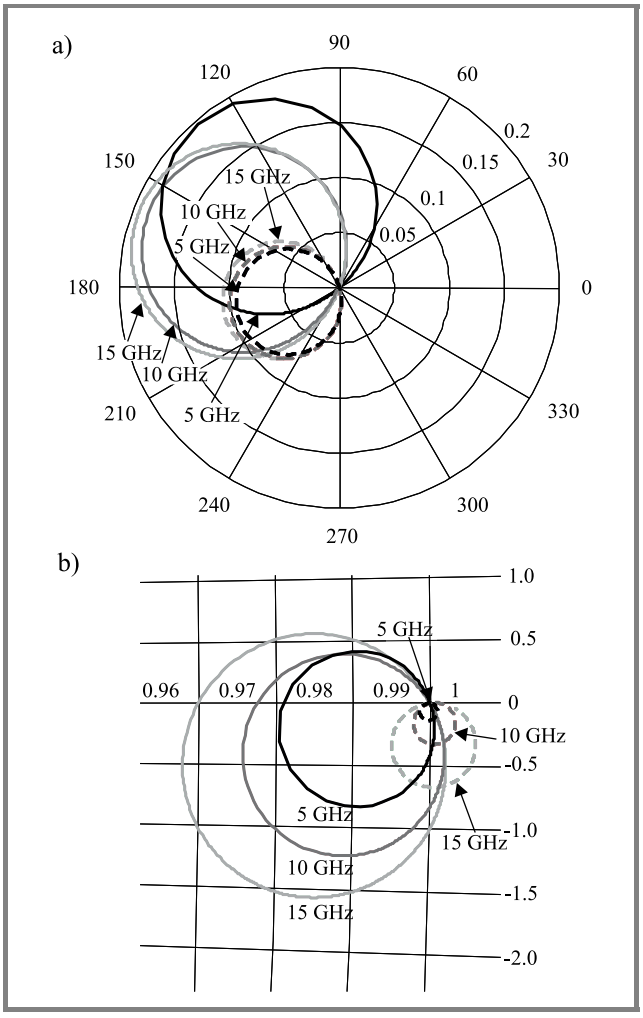


Fig. 7. Loci of $|\Gamma_{MSL}| = 1$ in the plane of the de-embedded reflection coefficient Γ'_{CPW} for (a) a matched load ($\Gamma_{CPW} = 0$), and (b) an open circuit ($\Gamma_{CPW} = 1$), for ISS (- - -) and GaAs (——) substrate.

Due to bilinear relationship between Γ_m and Γ_{MSL}, the deviations are constrained by the locus circle $|\Gamma_{MSL}| = 1$ in the complex Γ'_{CPW} plane. Such loci are presented in Fig. 7 in polar coordinates for a matched load and an ideal open circuit, at three frequencies: 5, 10, and 15 GHz and for both substrates (see Table 1). As it can be seen, the multimode propagation errors may have considerable effects, especially in case of the matched load. In both cases the errors are bigger for the GaAs substrate than for the ISS substrate, which can be justified with a higher transmission on the MSL mode in case of the GaAs substrate (see Fig. 4b). Furthermore, the error increases with frequency, which may be explained with an increasing transmission on the MSL mode seen in Fig. 4b.

3.2. CB-CPW transmission line section

In this section we investigate multimode propagation errors in case of a section of the CB-CPW transmission line. To this end we examine the impact of the parasitic MSL mode transmission on the measurement of the line parameters for the CPW mode. The basic idea of our method is shown in Fig. 8.

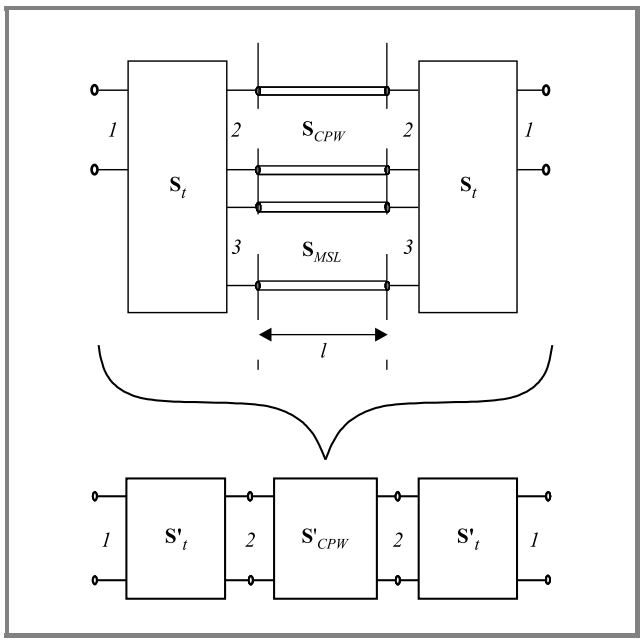


Fig. 8. Analysis method for the CB-CPW line section.

To simulate the measurement of a section of a multimode lossless CB-CPW line, we describe propagation for the CPW and MSL mode with scattering matrices:

$$\mathbf{S}_{CPW} = \begin{bmatrix} e^{-j\beta_{CPW}l} & 0 \\ 0 & e^{-j\beta_{CPW}l} \end{bmatrix}, \tag{2a}$$

$$\mathbf{S}_{MSL} = \begin{bmatrix} e^{-j\beta_{MSL}l} & 0 \\ 0 & e^{-j\beta_{MSL}l} \end{bmatrix}, \tag{2b}$$

where β_{CPW} and β_{MSL} are propagation constants of the CPW and MSL mode, respectively, determined from the 3D EM simulations, and l is the line length. In the measurement we obtain two-port S-parameters $\mathbf{S}_m$, which are different from the parameters $\mathbf{S}_{CPW}$ of the CPW line because of the systematic errors introduced by the probe and parasitic transmission over the MSL mode. From $\mathbf{S}_m$, we de-embed matrix $\mathbf{S}'_{CPW}$ of the CPW line employing previously determined two-port probe description with matrix $\mathbf{S}'_t$. For this purpose we apply the wave transmission matrix notation utilising the following relationship:

$$\mathbf{T}'_{CPW} = \mathbf{T}'^{-1}_t \mathbf{T}_m \overline{\mathbf{T}'_t}^{-1}, \tag{3}$$

where $\mathbf{T}'_{CPW}$, $\mathbf{T}'_t$ and $\mathbf{T}_m$ are the transmission matrices corresponding to relevant scattering matrices, and $\overline{\mathbf{T}'_t}$ denotes the matrix of the reversely connected two-port $\mathbf{T}'_t$.

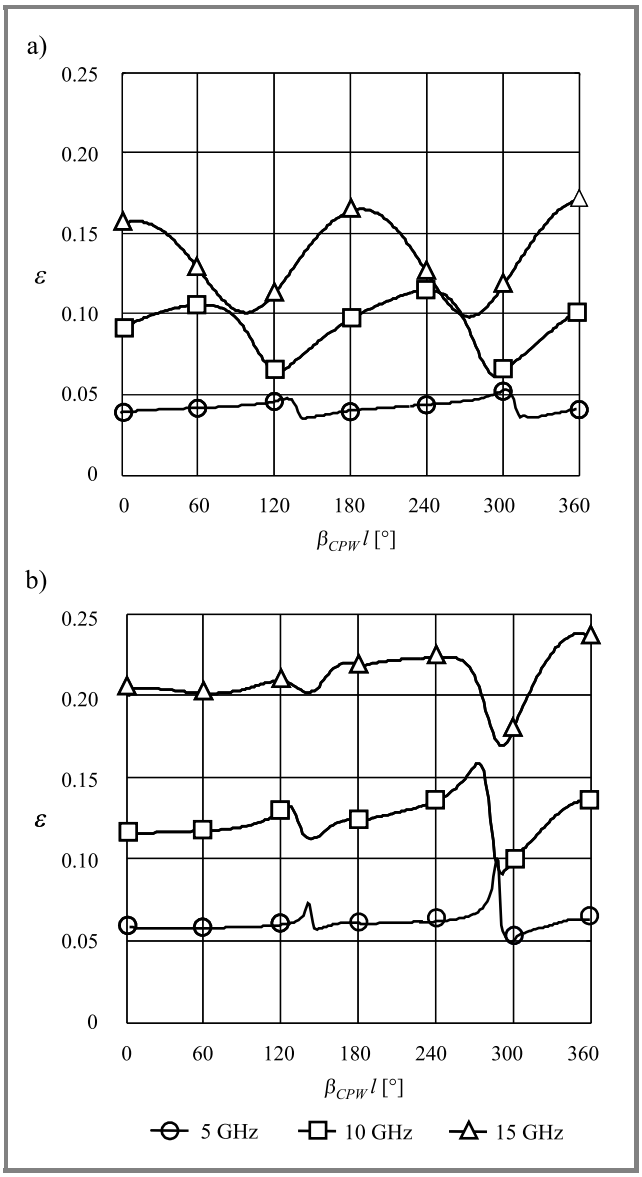


Fig. 9. Worst case error ε due to multimode propagation in a measurement of CPW line S-parameters as a function of CPW line electrical length for (a) ISS and (b) GaAs substrate.

Subsequently, with (3) we calculate the worst case deviation between the actual and de-embedded parameters of the CPW line, defined as:

$$\varepsilon = \max_{i,j} \left| S'_{CPW,ij} - S_{CPW,ij} \right| . \quad (4)$$

Results of our simulations for the ISS and GaAs substrate for different line lengths are shown in Fig. 9. The worst case error ε is presented as a function of the CPW electrical line length at three frequencies: 5, 10 and 15 GHz. As it can be can seen in Fig. 9, the error caused by multimode propagation is significant. Its dependence on the line length reveals some ripples that may be explained with the interference of both modes each having own phase velocity (see Fig. 2). Growth of the errors in frequency can be attributed to the increase of the MSL mode transmission seen in Fig. 4. Furthermore, comparison between Fig. 9a and Fig. 9b shows that the multimode propagation error is higher for the GaAs substrate, which corresponds well with the higher transmission of the MSL mode for this substrate (see Fig. 4b).

4. Conclusions

We have presented for the first time a systematic analysis of errors occurring in on-wafer measurement of typical CPW elements due to the presence of the parasitic MSL mode in substrates with a backside metallisation. We determined the upper bound for these errors in measurements of some exemplary one- and two-port devices. Our analysis consisted of two steps.

At first we characterized a transition between an air-coplanar probe and a CB-CPW line using 3D EM simulations. We took into account two types of substrates: the ISS calibration substrate and a typical MMIC GaAs substrate. In both cases our results revealed significance of the parasitic MSL mode in comparison with the transmission on the main CPW mode. We utilised results of the EM simulations to model the transition as a multimode three-port.

In the next step we applied the model to assess the errors due to the parasitic MSL mode by mimicking the conventional single-mode measurement procedure typically used for characterisation of CPW devices. To this end, we examined a matched load, an ideal open circuit, and CB-CPW transmission line section as the most frequently used exemplary circuits. We studied errors in de-embedding of their S-parameters from simulated measurements under varying circuit conditions for the MSL mode. Assuming passive response of the MSL circuit, we determined upper bounds for the errors in the measurements of these CPW devices.

Our analysis reveals that the errors caused by the parasitic MSL mode may seriously deteriorate measurements, especially for CPW loads and lines. This in turn may have a significant impact on both CB-CPW-based calibration and de-embedding procedures. In consequence, the design reliability of CB-CPW-based circuits, e.g., MMICs, may suffer much.

References

[1] S. A. Wartenberg, *RF Measurements of Dies and Packages*, *Artech House Microwave Library*. Boston: Artech House, 2002.

[2] M. Riaziat, R. Mjidi-Ahy, and I.-J. Feng, "Propagation modes and dispersion characteristics of coplanar waveguides", *IEEE Trans. Microw. Theory Techn.*, vol. 38, pp. 245–251, 1990.

[3] K. Beilenhoff and W. Heinrich, "Excitation of the parasitic parallel-plate line mode at coplanar discontinuities", in *Proc. IEEE MTT-S 1997*, Denver, USA, 1997, pp. 1789–1792.

[4] R. B. Marx and D. F. Williams, "A general waveguide circuit theory", *J. Res. Natl. Inst. Stand. Technol.*, vol. 97, no. 5, pp. 533–562, 1992.

[5] D. F. Williams, L. A. Hayden, and R. B. Marks, "A complete multimode equivalent-circuit theory for electrical design", *J. Res. Natl. Inst. Stand. Technol.*, vol. 102, no. 4, pp. 405–423, 1997.

[6] W. Heinrich, F. Schnieder, and T. Tischler, "Dispersion and radiation characteristics of conductor-backed CPW with finite ground width", in *Proc. IEEE MTT-S 2000*, Boston, USA, 2000, vol. 3, pp. 1663–1666.

[7] C.-C. Tien, C.-K. C. Tzuang, S. T. Peng, and C.-C. Chang, "Transmission characteristics of finite-width conductor-backed coplanar waveguide", *IEEE Trans. Microw. Theory Techn.*, vol. 41, pp. 1616–1624, 1993.

[8] J.-P. Raskin, G. Gauthier, L. P. Katehi, and G. M. Rebeiz, "Mode conversion at GCPW-to-microstrip-line transition", *IEEE Trans. Microw. Theory Techn.*, vol. 48, pp. 158–161, 2000.

[9] R. W. Jackson, "Mode conversion due to discontinuities in modified grounded coplanar waveguide", in *Proc. IEEE MTT-S 1988*, New York, USA, 1988, pp. 203–206.

[10] R. B. Marks, "A multiline method of network analyzer calibration", *IEEE Trans. Microw. Theory Techn.*, vol. 39, pp. 1205–1215, 1991.

[11] D. F. Williams, J.-M. Belquin, G. Dambrine, and R. Fenton, "On-wafer measurements at millimeter wave frequencies", in *Proc. IEEE MTT-S 1996*, San Francisco, USA, 1996, pp. 1683–1686.

[12] G. F. Engen and C. A. Hoer, "Thru-reflect-line: an improved technique for calibrating the dual six-port automatic network analyzer", *IEEE Trans. Microw. Theory Techn.*, vol. 12, pp. 987–993, 1990.

[13] A. Lewandowski and W. Wiatr, "Errors in on-wafer measurements due to multimode propagation", in *XV Int. Microw. Conf. MIKON-2004*, Warsaw, Poland, 2004, pp. 759–763.

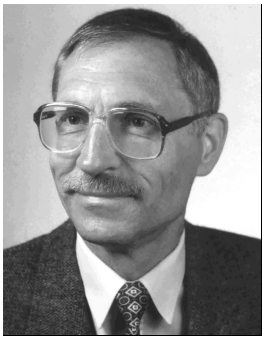
[14] QWED, "QuickWave V.2.2 Manual", http://www.qwed.com.pl

[15] A. Davidson, K. Jones, and E. Strid,"LRM and LRRM calibrations with automatic determination of load inductance", in *34th ARFTG Conf. Dig.*, Ft. Lauderdale, USA, 1989, pp. 57–62.



Arkadiusz Lewandowski was born in Poland in 1975. He received the M.Sc. degree in electrical engineering from Warsaw University of Technology, Poland, in 2001. Since 2002 he has been with Institute of Electronics Systems, Warsaw University of Technology pursuing the Ph.D. degree in the area of microwave measurements. From 2002 to 2004 he was involved in the development of DDS-based generators of radar signals at Telecommunications Research Institute, Warsaw, Poland. He is currently with National Institute of Standards and Technology, Boulder, USA, working on the development of VNA calibration methods applicable for time-domain

measurements. His current research interests include on-wafer microwave measurements and VNA calibration techniques.
e-mail: A.Lewandowski@ieee.org
Institute of Electronic Systems
Warsaw University of Technology
Nowowiejska st 15/19
00-661 Warsaw, Poland



Wojciech Wiatr received the M.Sc. and the Ph.D. degrees in electronics engineering from Warsaw University of Technology, Warsaw, Poland, in 1970 and 1980, respectively. In 1971, he joined the Institute of Electron Technology CEMI in Warsaw, affiliated to national semiconductor industry. Since 1972, he has been with the Institute of Electronic Systems at the Warsaw University of Technology, presently as an Assistant Professor. His main scientific interests are in the field of precision microwave measurements. He has been developing new techniques and instrumentation for broadband scattering and noise parameter measurements of microwave transistors and MMICs. He is an inventor of the RF multistate total power radiometer realizing simultaneous noise and vector analysis of microwave networks with natural noise excitation. He was engaged in realization of many research projects. In noise metrology, he collaborated with the National Radio Astronomy Observatory in Charlottesville, VA, USA, and the Ferdinand-Braun-Institut für Höchstfrequenztechnik in Berlin. He has been an Affiliate Researcher of the National Institute of Standards and Technology in Boulder, CO, USA. Dr. Wiatr published 1 book, over 90 papers and holds two patents.
e-mail: Wiatr@ise.pw.edu.pl
Institute of Electronic Systems
Warsaw University of Technology
Nowowiejska st 15/19
00-661 Warsaw, Poland

Paper

A 100 W ISM 2.45 GHz-band power test system

Wojciech Wojtasiak, Daniel Gryglewski, and Wojciech Gwarek

Abstract—This paper describes development of solid-state microwave power test system (MPTS) operating over 2.3 to 2.6 GHz with the output power level of 100 W for industrial applications in material processing, and for designing of microwave power industrial equipment. The MPTS unit consists of four major parts: PLL synthesizer, high power solid-state amplifier, detector probes for return losses and leakage measurement and microcontroller. The MPTS system is able to operate in either single fixed-frequency regime, or in swept mode with self-tuning for minimum reflection of a heated load.

Keywords— microwave precise heating, high power solid-state amplifier , push-pull GaAs FET, synthetsizer, power measurement unit.

1. Introduction

Despite theoretical advantages of microwave power systems, modern industrial applications of microwaves are still limited. The main reason is that there is only one relatively low cost, high power microwave source available – the magnetron. It provides much distorted microwave signal with respect to an amplitude and spectrum purity. Moreover its frequency behavior is strongly dependent on the heated load properties. On the other hand, many industrial applications in material processing require microwave heating with precise frequency and amplitude control based on the feedback from the time varying process parameters. Such requirements can be only fulfilled by solid-state high frequency stability high power sources (HPS). They are based on synthesized VCO high power solid-state amplifiers (SSPA). Other advantages of HPS as compared to magnetrons and other microwave tubes are also important. In particular, the SSPAs require lower voltage operation and simpler cooling system, and are more reliable. However, the magnetrons achieve higher efficiency and higher output power levels at low cost. In fact, a fundamental disadvantage of HPSs lies in their thermal limitations. The basic components of HPSs are microwave transistors of a proper output power level. Currently, due to the development of wireless personal communications market, the demand for high power solid-state transmitters is on the rise. This demand is also the reason for the fast development of high power microwave transistors technologies.

This paper presents the concept and practical development of a 100 W ISM 2.4 GHz-band microwave power test system (MPTS). It is built as a modular structure with power amplifiers based on a new generation high power push-pull GaAs FETs [1]. These transistors operating in class AB (cw) achieve up to 300 W (240 W available in commercial market) output power level at W-CDMA frequency band. The MPTS system includes four major sections: a synthesized VCO based on PLL subsystem with digital variable attenuator and switch for AM modulation, power measurement probes with diode detectors, high power amplifier and microcontroller (μC). It is assumed that this PC controlled system will be used for a variety of functions including:

- delivery of microwave power up to 100 W at a single frequency with precise control of power level and frequency;
- measurement of reflection coefficient versus frequency at high power levels;
- automatic tuning of the frequency of the system to the minimum of reflection from the load changing in time;
- precise measurement of leakages from microwave industrial systems versus frequency with the dynamic range between the maximum input power and minimum detected leakage up to 100 dB.

Other functions may be subject to PC programming depending on particular needs.

2. Concept of MPTS

The idea and the block diagram of the MPTS system is shown in Figs. 1 and 2. The MPTS can operate in either single fixed-frequency regime, or in swept mode with self-tuning for minimum reflection coefficient of a resonant load such as a cavity partially filled with the heated material. The reflection characteristics are continuously extracted using power measurements obtained from the detector probes

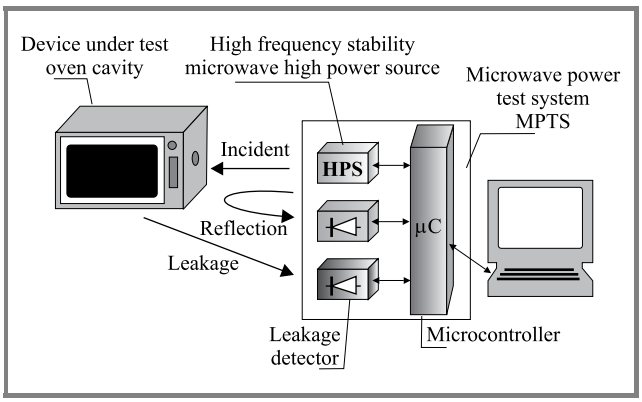


Fig. 1. The concept and block diagram of the MPTS system.

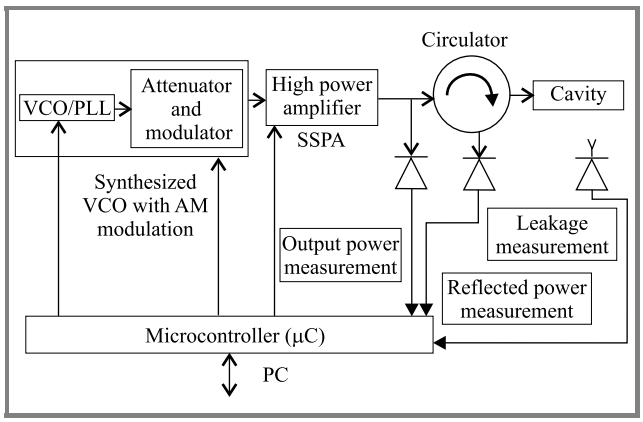


Fig. 2. The block diagram of the MPTS system.

placed at the output SSPA and in the third arm of the circulator. The setting and control of the output frequency and output power level over a 15 dB dynamic range as well as all calculations are realized by means of an 8-bit microcomputer with 4 KBytes flash memory (PEROM) [2]. The PC is used as the user interface for programming various functions of the setup and displaying the basic parameters and measured characteristics.

3. Synthesized VCO

The synthesized VCO is based on PLL subsystem. To realize VCO the IBM HBT transistor (IBM43RF0100) and the varactor diode (MA46477-120 by M/ACOM) were chosen.

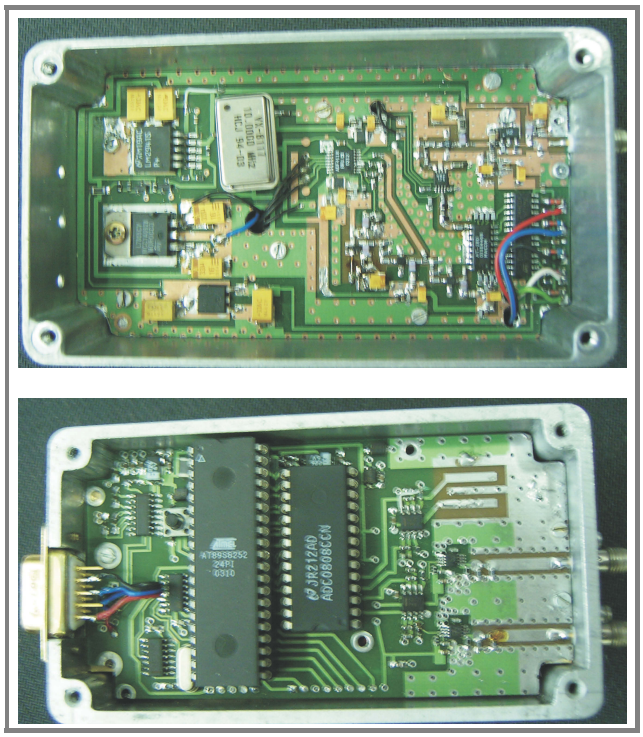


Fig. 3. The view of synthesized VCO (microwave part and microcontroller with detectors).

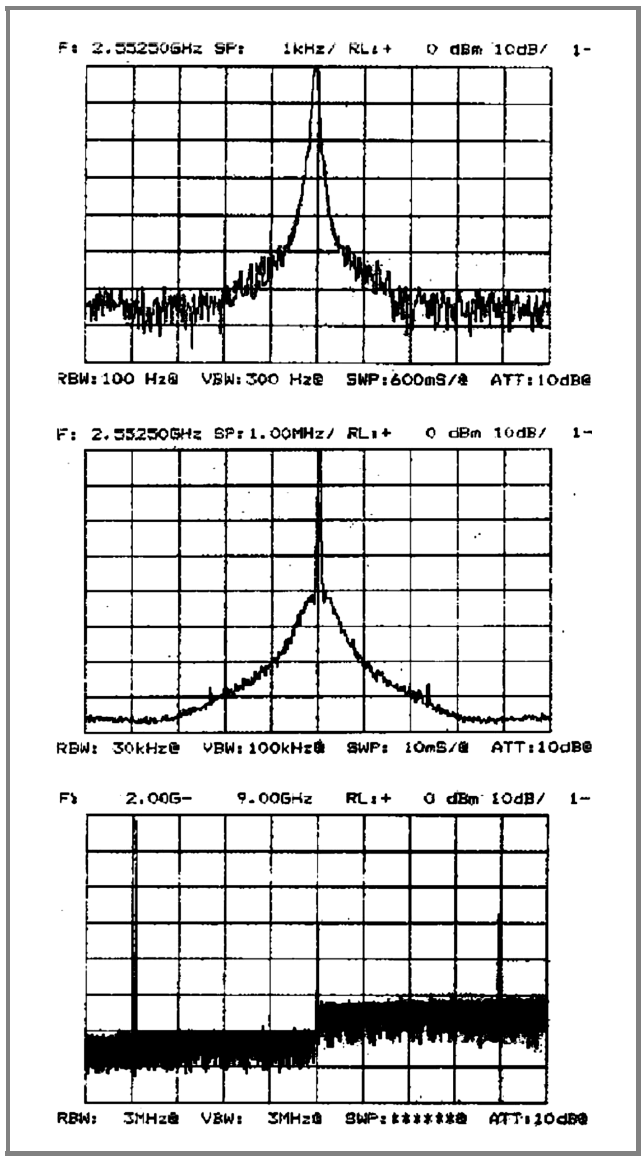


Fig. 4. The spectrum of synthesized VCO.

The small-signal approach with the Nyquist criteria was used for the design. The oscillator structure was optimized by means of ADS microwave simulator (Agilent Technologies) in microstrip technique. The limitation of the pulling effect was achieved by reduction of coupling between microstrip resonator and varactor. The basic component of PLL subsystem is a VLSI monolithic circuit AD4118 (ANALOG DEVICES) integrating adjustable frequency prescaler, phase/frequency detector, charge pump, and reference oscillator/buffer functions. The device requires an external loop filter and there is no need to use other active components. The practically realized synthesizer operates over the wide 2.2 to 2.8 GHz frequency range with minimum frequency resolution $\Delta f = 250$ kHz and is fully programmable. The long-term frequency stability as well as phase noises level of the synthesizer depends mainly on the stability of reference frequency standard. As reference source the TCXO crystal oscillator is used in synthe-

sizer. To achieve a high isolation and an appropriate output power level two monolithic amplifiers (ERA-3 and ERA-3 by MiniCircuits) at the oscillator output were applied. The output part of synthesizer was especially developed for the class AB SSPA driving purpose. This subsystem includes a high gain, more then 14 dB, 1 W power amplifier with the class AB AlGaAs/GaAs HJFET SHF0289 manufactured by SIRENZA driven by another monolithic amplifier ERA-5. To obtain a required output power level dynamic, the digital attenuator AT270 (by M/ACOM) was applied. As AM modulator, the switch HMC174 (HITTITE) was used. The AM modulation is an option of MPTS (turn on/off from PC). It is applied the sensitivity of leakage measurement. Both components are GaAs MESFET monolithic devices and low cost. The view of the complete synthesized VCO and its spectrum are presented in Figs. 3 and 4.

The AD8314 (ANALOG DEVICES) was chosen for incident and reflected power detection purposes. The probe

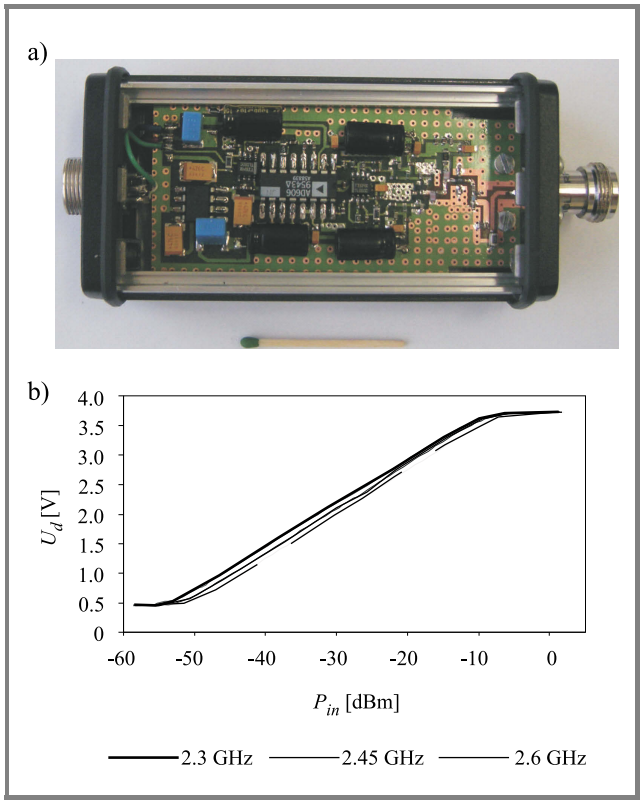


Fig. 5. (a) The photos of the leakage detector and (b) its characteristics $U_d = f(P_{in})$.

for leakage measurement is equipped with a two-Schottky-diodes detector followed by a logarithmic narrow-band amplifier AD606. The leakage detector and its characteristics $U_d = f(P_{in})$ has been shown in Fig. 5.

4. High power amplifier SSPA

The SSPA consists of the 10 W driver amplifier with a class A GaAs MESFET to achieve high gain and the 100 W balanced amplifier with push-pull GaAs FET operating in class AB, and 2-way divider/combiner as shown in Fig. 6.

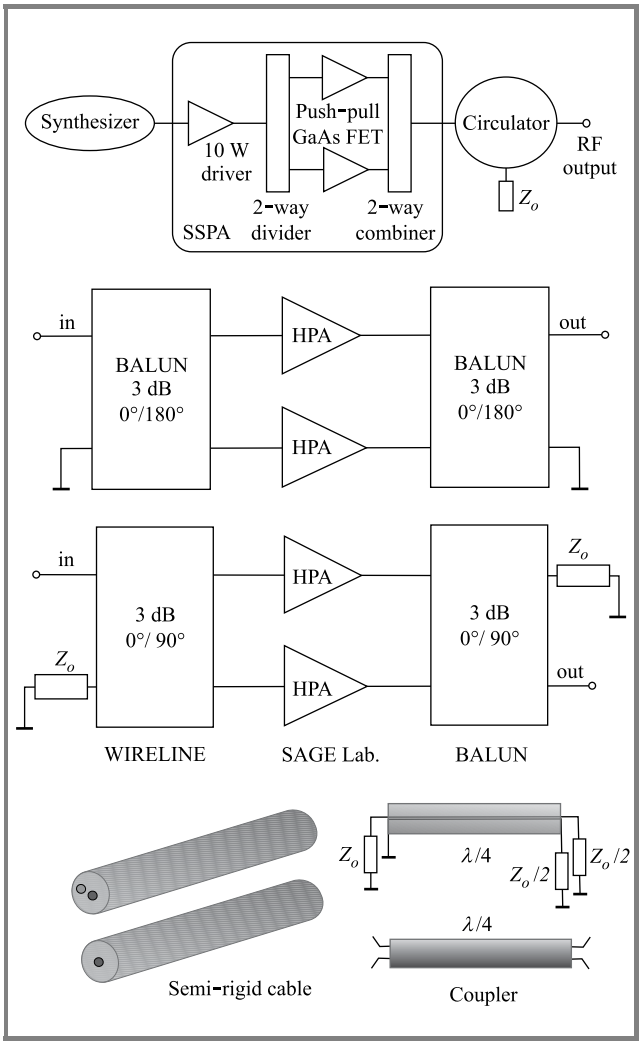


Fig. 6. Block diagram of the 100 W SSPA and the combining technique with semi-rigid cable.

The active components of the SSPA are the common source FETs: the 10 W L-band FLL120MK as driver and push-pull FLL1200IU-3 of $P_{sat} = 120$ W at 2.45 GHz, both manufactured by FUJITSU [1]. The surface-mount 3 dB/90° WIRELINE couplers, developed and patented by SAGE Lab., were used as 2-way divider/combiner [3]. All elements used in the design are commercially available. The WIRELINE couplers consist of a pair of wire center conductors surrounded by a continuous dielectric insulator and shielded by a drawn or extruded outer jacket. Finally, the construction has the physical properties of semi-rigid coaxial cable with the electrical features of a TEM coupled line. These couplers also reduce sizes of a board circuit. The insertion loss of WIRELINE 2-way divider/combiner is less than 0.2 dB within the desired band.

The basic concern in high power amplifier design is appropriate matching at the input and output of the transistor,

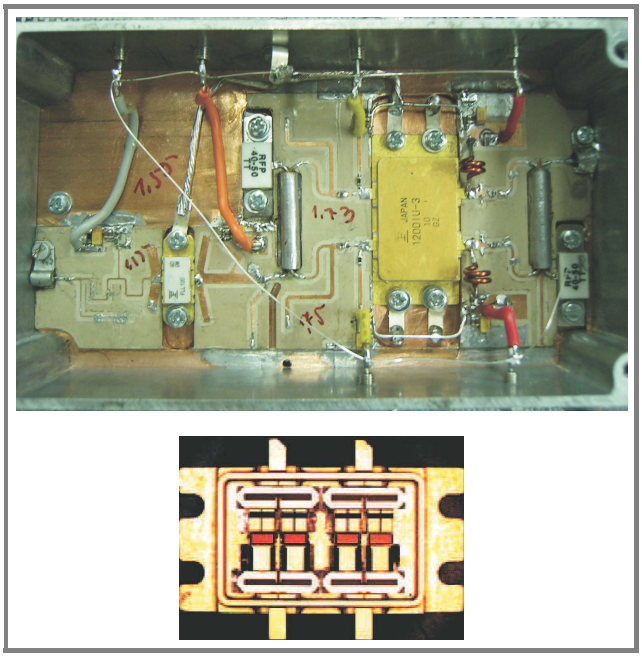


Fig. 7. The view of the 100 W amplifier with FLL120MK as the driver and FLL1200IU-3 push-pull transistor.

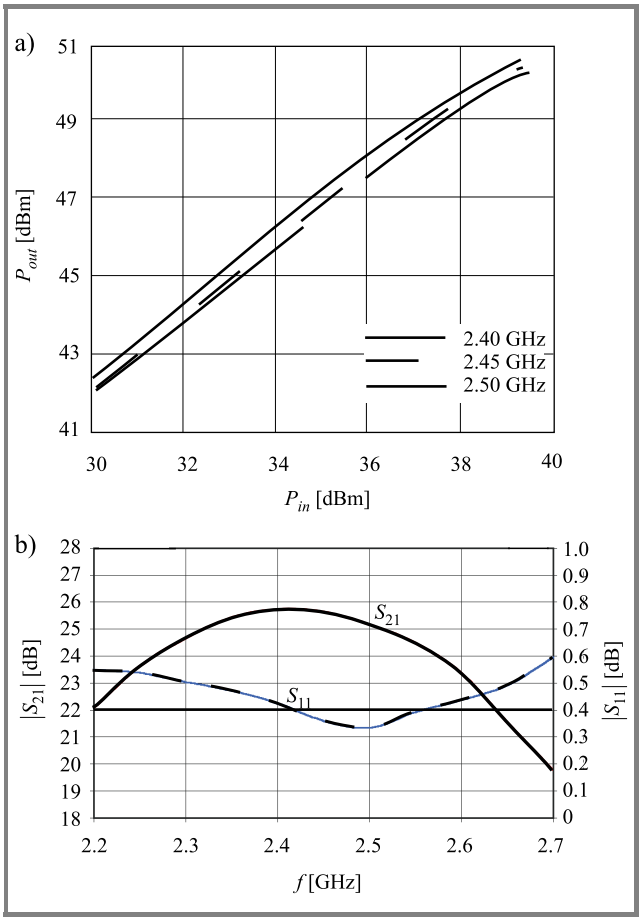


Fig. 8. (a) The $P_{out} = f(P_{in})$ small-signal gain and (b) reflection versus frequency of the 100 W amplifier with FLL1200IU-3 push-pull transistor.

and it is necessary to know the values of input and output impedances within a given frequency range. For high power transistors, the only practical way to determine is the source/load-pull technique. Numerical methods based on transient analysis or harmonic balance are not currently effective due to the very complicated transistor structure. In general, measurement methods of optimum source and load impedances for different amplifier requirements are well known and applied. However, in the case of high power transistors this technique causes many problems because the measured impedances usually have a very low real part. It can be assumed the error of the best source/load-pull technique amounts to within about 10% [4]. Therefore, to achieve optimum or at least satisfactory results, some re-tuning is necessary, in particular for the output matching section. Some of the high power transistors available on the market include internal matching circuits helping to achieve satisfactory performance at a specific frequency. They are, however, very difficult to tune in a wider frequency range. The view of the 100 W amplifier (SSPA) with FLL1200IU-3 push-pull GaAs FET (transistor consist of four chips and its structure) and its power characteristic is shown in Figs. 7 and 8. To reduce the dimension of the amplifier, the Rogers substrate RT/DUROID 6010 was used.

5. Performances

Here is the summary of the features of the developed MPTS (Fig. 9):

- frequency band from 2.3 to 2.6 GHz, set by a microcontroller with 250 kHz step;
- long-term frequency stability more than 10^{-7} and phase noises: –75 dBc/Hz 1kHz;
- output power level up to 100 W, controlled within 15 dB range with 0.5 dB step;
- AM modulation: square wave with frequency 2 kHz that can be switched on/off by software;
- output: N type connector 50 W from circulator integrated with high power load;
- leakage detector: more than 45 dB dynamic (up to –105 dB below the maximum power generated by the power module), VSWR less than 1.2;
- microcontroller software: full setup for operating regime, output power level, range and step frequency;
- PC interface: connection RS-232 or USB;
- PC control software: graphical presentation of measurement results – reflection and leakage versus frequency.



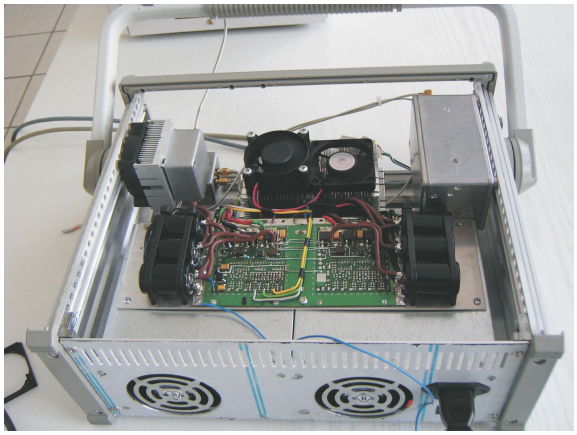




Fig. 9. The view of the 100 W ISM 2.4 GHz power test system.

6. Conclusions

The MPTS system has been successfully realized. It makes available many new practical applications of microwave power, such as microwave-driven chemical reactions or precise measurements of material parameters, heating efficiency, and system leakage.

References

[1] Fujitsu, "Microwave Semiconductors Data Book", http://www.fcsi.fujitsu.com

[2] Atmel, http://www.atmel.com

[3] Sage Lab., Inc., "Wireline and WirePac Design Guide", http://www.sage.com

[4] Fujitsu, "Application Note 008, 011", http://www.fcsi.fujitsu.co



Wojciech Wojtasiak received the M.Sc. and Ph.D. degrees in electronic engineering from the Warsaw University of Technology, Warsaw, Poland, in 1984 and 1998, respectively. He is currently an Assistant Professor at WUT. His early research interests concerned characterization and application of nonuniform transmission lines. Since 1990 his research activity concentrates on the design of high-frequency-stability microwave high-power solid-state sources and transmitters. Recently, he has been also engaged in research on thermal analysis in time domain of high power microwave FETs. Since 1998 he has been a member of IEEE.
e-mail: wwojtas@ire.pw.edu.pl
Institute of Radioelectronics
Warsaw University of Technology
Nowowiejska st 15/19
00-665 Warsaw, Poland



Daniel Gryglewski received the M.Sc. and Ph.D. degrees in electronic engineering from the Warsaw University of Technology, Warsaw, Poland, in 1996 and 2001, respectively. In 2001 he became an Assistant Professor at WUT. His research activity concentrates on high power microwave amplifiers.

e-mail: dgrygle@ire.pw.edu.pl
Institute of Radioelectronics
Warsaw University of Technology
Nowowiejska st 15/19
00-665 Warsaw, Poland



Wojciech K. Gwarek was born and works now in Poland. He graduated from the Warsaw University of Technology (1970) from which he also received the Ph.D. (1977) and where he is currently a Professor. He also holds M.Sc. degree from M.I.T. (1974). His early research activity concentrated on nonlinear analysis of microwave mixers and measurements. Since mid-eighties he has been engaged in research on electromagnetic analysis in time domain. Since 1990 his activity also includes development of commercial software tools by himself and a group of his co-workers. The brand names of these tools QuickWave and Concerto have become popular worldwide. Prof. Gwarek is the founder and president of QWED company, which successfully commercializes these tools. He has been also involved in many IEEE activities as a reviewer for various journals, member of the TPC of IMS and the Chairman of the MTT/AP/AES Joint Chapter of Poland. Since 2001 he has been a fellow of IEEE.

e-mail: gwarek@ire.pw.edu.pl
Institute of Radioelectronics
Warsaw University of Technology
Nowowiejska st 15/19
00-665 Warsaw, Poland

Paper

A broadband multistate interferometer for impedance measurement

Piotr Szymański and Wojciech Wiatr

Abstract— We present a new four-state interferometer for measuring vectorial reflection coefficient from 50 to 1800 MHz. The interferometer is composed of a four-state phase shifter, a double-directional coupler and a spectrum analyzer with an in-built tracking generator. We describe a design of the interferometer and methods developed for its calibration and de-embedding the measurements. Experimental data verify good accuracy of the impedance measurement.

Keywords— impedance measurement, multistate interferometer, reflectometer.

1. Introduction

Vectorial reflection coefficient measurement may be performed today using various instruments. Besides the most popular vector network analyzers, there is a broad class of interferometers, in which the relationship between the incident and reflected waves on the tested device is established indirectly by measuring power of interfering different microwave signals that are linearly related to those waves. Within the class, there are instruments performing the measurement instantly (measurement multiports) or in successive steps (multistate reflectometers). The former group is represented by the well-known six-port junction [1], while the last one by multistate reflectometer [2] or AM/PM switched three port reflectometer [3]. All they yield almost the same number of measured powers necessary to unambigously determine the reflection coefficient.

As it has been shown in [3], sequential measurements made with one detector in several independent states of the switched three-port are equivalent to simultaneous readings from four detectors in the six-port junction. Since designers of the interferometers pursue for simplicity and lower cost, they tend to substitute the number of measurement states for the number of measurement ports at an expense of extended measurement time.

For automated measurement, the multistate interferometers use switched AM/PM modulators to realize different measurement states. Set of all amplitude and phase states realized by the modulator at a given frequency is typically depicted with points in polar coordinates and referred to as the modulator state distribution. Since accuracy of the impedance measurement depends on a particular state distribution, an optimal arrangement of the distributions in the whole frequency range is a challenging task for an instrument designer. As it was shown in [4], AM/PM switches of reflection type may operate over the bandwidth of few octaves, if properly designed.

The theory behind the reflection coefficient measurement using the six-port has been known for over quarter of a century [1] and can be applied to the multistate interferometers as well [2, 3]. There are two types of models that describe such a measurement, the linear and nonlinear ones and this results in the relevant calibration and accuracy enhancement techniques utilized for the multistate interferometers. Generally, the linear methods [5] are much simpler to implement in computer than the nonlinear ones [6], but usually utilize more unknown quantities and thus are more measurement extensive.

We present here a new four-state interferometer system for impedance measurement from 50 to 1800 MHz. The system employs a spectrum analyzer with an in-built tracking generator, a four-state phase shifter and a double directional coupler. The generator stimulates the measurement circuit through phase shifter and the coupler while the receiver of the spectrum analyzer measures the interfering waves in every phase-state of the shifter. We describe the shifter design and discuss two different models for the impedance measurement validating they usefulness with experimental measurements.

2. Multistate interferometer

A general scheme of the multistate interferometer is shown in Fig. 1a. The instrument measuring unknown impedance Z_x consists of a signal source, an AM/PM switch, a double directional coupler and a detector. In the kth state, the modulator produces two stimulating signals, a_{1k} and a_{2k}, that emerge then as the reflected waves b_{3k} and b_{4k} at relevant ports of the coupler. Due to mismatched terminations (the detector and Z_x), incident waves a_{3k} and a_{4k}, respectively, appear also at these ports. Consequently, all the waves interfere in the coupler's main line and the detector measures the resultant power. The measured power depends on the phase and magnitude relationships of both stimulating signals, which vary along with the modulator state. Generally, any stable receiver capable of measuring power may fulfil the detector's role.

The waves' interference can be explained using the equivalent circuit shown in Fig. 1b, where two wave sources b_{3k} and b_{4k} model the stimulation, and the reflection coefficient Γ_{rk} represents the receiver (detector) impedance for the kth state. The power measured by the receiver in this state is described by

$$P_k = \alpha_k \frac{|b_{3k} + \Gamma_x b_{4k}|^2}{|1 - \Gamma_x \Gamma_{rk}|^2} = c_k \frac{|\Gamma_x - q_k|^2}{|1 - \Gamma_x \Gamma_{rk}|^2}, \qquad (1)$$

where $q_k = -b_{3k}/b_{4k}$ is the reference point, i.e., the value of Γ_x for which the power drops to zero, and α_k and $c_k = \alpha_k |b_{4k}|^2$ are system constants. In the plane of the complex reflection coefficient Γ_x, formula (1) describes a family of cirles, being loci of constant power. The circles are excentric if the receiver is mismatched ($\Gamma_{rk} \neq 0$).

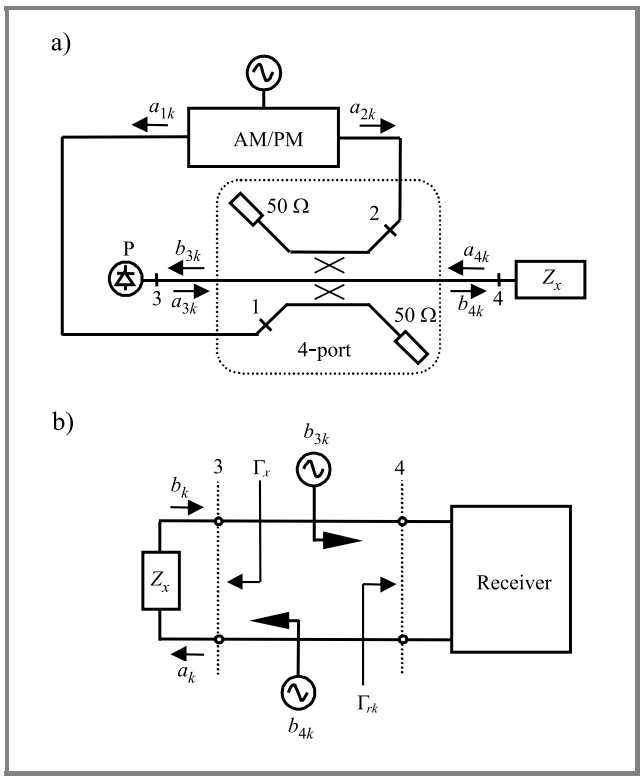


Fig. 1. Multistate interferometer: functional diagram (a) and its equivalent circuit (b).

There are five real parameters: c_k, $\mathrm{Re}\, q_k$, $\mathrm{Im}\, q_k$, $\mathrm{Re}\,\Gamma_{rk}$ and $\mathrm{Im}\,\Gamma_{rk}$, in formula (1). Therefore, calibration of the multistate interferometer requires, in general, measuring of at least five different impedance standards in each state to determine the unknown parameters. Considering K states of the interferometer, one gets the total of $5K$ calibration measurements. In case, when the input reflection coefficient of the receiver is invariant to the interferometer's state, the number of the unknowns reduces to $3K+2$ and thus fewer standards are necessary for the calibration.

3. Four-state phase shifter

We have decided to use a four-state phase shifter as our modulator and designed it considering availability and affordable costs of its components. The block diagram of the shifter is presented in Fig. 2. With the signal source

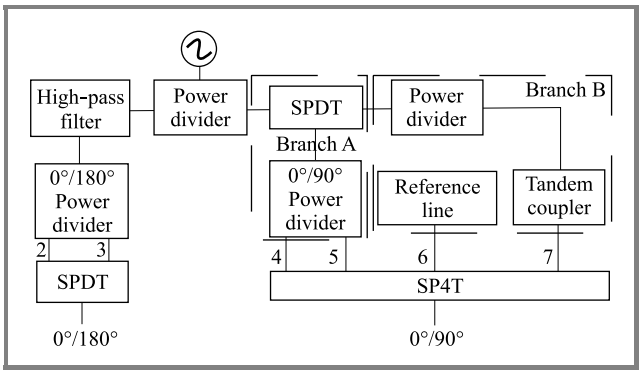


Fig. 2. Block diagram of the four-state phase shifter.

at the input, this three-port circuit produces two signals shifted in phase by 0° or 180° at one output and 0° or 90° at the other one. The phase shifts are realized by two specialized sections of this circuit, which are separated with the in-phase input power divider. Each section comprises a power divider whose outputs are shifted in phase and the phase keying rely on selecting the appropriate signal.

In contrast to the 0°/180° section, the 0°/90° section is composed of two branches, A and B, to provide coverage of the full frequency range. Due to limited bandwidth (50–700 MHz) of the 0°/90° commercial divider in branch A, the phase shifter in branch B, composed of another in-phase power divider, a tandem coupler and a reference line (a delay line), was built entirely in house for the upper subband (700–2000 MHz). The switches, single pole double throw (SPDT) and single pole four throw (SP4T) controlled by a microcontroller (not shown in Fig. 2), select the appropriate signals in each section, shifted in phase by: 0°, 90°, 180° or 270°. The phase shifts have been optimized in the whole frequency range using advanced design system (ADS), a microwave circuit simulator, on the basis of characteristics measured for the major components. To correct the phase at low frequency end, the high-pass filter (see Fig. 2) has been added in the 0°/180° section.

Distribution of the reference points can be evaluated from the three-port S parameters:

$$q_{ji} = \frac{S_{j1}}{S_{i1}}, \qquad (2)$$

where indices $i = 2,3$ and $j = 4,5,6,7$ regard relevant modulator's states in both subbands.

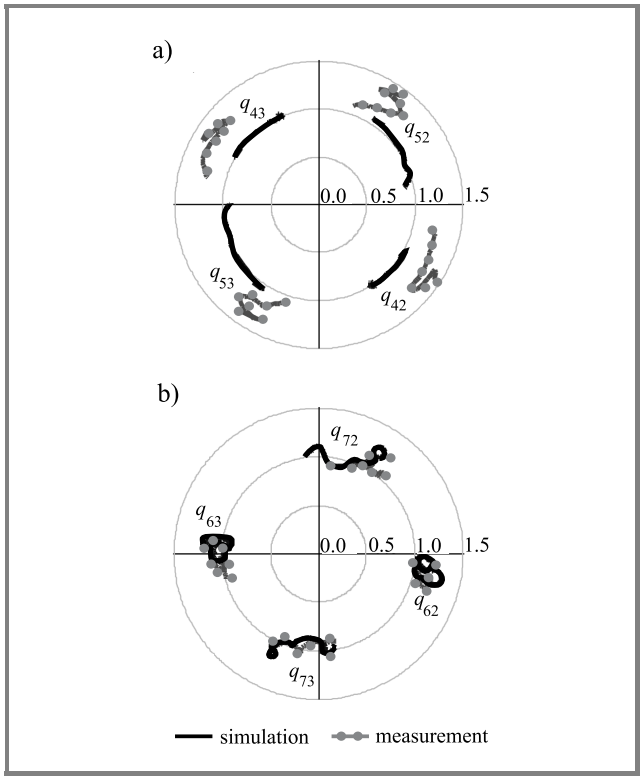


Fig. 3. Distribution of the modulator's phase states versus frequency in: lower (a) and upper (b) subbands.

Figure 3 shows frequency variations of (2) in the polar coordinates. The curves revolve similarly on each diagram thus maintaining almost 90° separation. The characteristics obtained by measurement and simulation in ADS are well matched, especially over the upper subband.

4. Calibration of multistate interferometer

Since in contrary to the six-port junction, the measurements made on the multistate interferometer do not comprise straight information on the incident wave in the circuit, the known six-port methods cannot be directly applied to calibration of the multistate interferometer. Therefore, we have developed our own method based on a linear model describing the measurements. For $\Gamma_{rk} = \Gamma_r = \text{const}$ ($k = 1, 2, 3, 4$) in formula (1), we write the equation:

$$\mathbf{x}\boldsymbol{\beta}_\mathbf{k} + p_k \mathbf{x}_\mathbf{p}\boldsymbol{\beta}_\mathbf{r} = p_k\,, \tag{3}$$

where p_k is a dimensionless power indication of the receiver in the kth state, the row vectors depend on Γ:

$$\mathbf{x} = \left[1-|\Gamma|^2 \quad 1+|\Gamma|^2 \quad -2\,\mathrm{Re}\,\Gamma \quad -2\,\mathrm{Im}\,\Gamma\right]$$

and

$$\mathbf{x_p} = \left[|\Gamma|^2 \quad 2\,\mathrm{Re}\,\Gamma \quad 2\,\mathrm{Im}\,\Gamma\right],$$

while the vectors $\boldsymbol{\beta}_\mathbf{k}$ and $\boldsymbol{\beta}_\mathbf{r}$ represent the system parameters:

$$\boldsymbol{\beta}_\mathbf{k}^\mathbf{T} = \frac{c_k}{2}\left[1-|q_k|^2 \quad 1+|q_k|^2 \quad -2\,\mathrm{Re}\,q_k \quad -2\,\mathrm{Im}\,q_k\right],$$

$$\boldsymbol{\beta}_\mathbf{k}^\mathbf{T} = -\left[|\Gamma_r|^2 \quad -\mathrm{Re}\,\Gamma_r \quad \mathrm{Im}\,\Gamma_r\right].$$

In the above formulae, the β parameters are nonlinearly related and this can be exploited to reduce the number of unknown coefficients in the Eq. (3) by $K+2$. The nonlinear relationships are as follows [7]:

$$\begin{aligned} \beta_{k2}^2 - \beta_{k1}^2 - \beta_{k3}^2 - \beta_{k4}^2 &= \boldsymbol{\beta}_\mathbf{k}^\mathbf{T}\mathbf{D}\boldsymbol{\beta}_\mathbf{k} = 0\,, \\ \beta_{r1}^2 - \beta_{r2}^2 - \beta_{r3}^2 &= \boldsymbol{\beta}_\mathbf{r}^\mathbf{T}\mathbf{D}_\mathbf{r}\boldsymbol{\beta}_\mathbf{r} - \mathbf{e}\boldsymbol{\beta}_\mathbf{r} = 0\,, \end{aligned} \tag{4}$$

where $\mathbf{D} = \text{diag}\ \{1\,{-}1\ 1\ 1\}$, $\mathbf{D_r} = \text{diag}\ \{0\ 1\ 1\}$ and $\mathbf{e} = [1\,0\,0]$.

For the system calibration, a set of known impedance standards $\{\Gamma_n\}$, $n = 1, 2, \ldots, N \geq 4$, is used and the measurements described by Eq. (3) can be set up in matrix form:

$$\mathbf{X_e}\boldsymbol{\beta} = \mathbf{y}\,, \tag{5}$$

where the vector $\boldsymbol{\beta}^\mathbf{T} = \left[\boldsymbol{\beta}_\mathbf{1}^\mathbf{T}\ \boldsymbol{\beta}_\mathbf{2}^\mathbf{T}\ \boldsymbol{\beta}_\mathbf{3}^\mathbf{T}\ \boldsymbol{\beta}_\mathbf{4}^\mathbf{T}\ \boldsymbol{\beta}_\mathbf{r}^\mathbf{T}\right]$ represents the unknown parameters, $\mathbf{y}^\mathbf{T} = \left[\mathbf{y}_\mathbf{1}^\mathbf{T}\ \mathbf{y}_\mathbf{2}^\mathbf{T}\ \mathbf{y}_\mathbf{3}^\mathbf{T}\ \mathbf{y}_\mathbf{4}^\mathbf{T}\right]$ comprises the measurements $\mathbf{y}_\mathbf{k}^\mathbf{T} = \left\{p_{kn}\right\}$ and the block coefficient matrix $\mathbf{X_e}$ is composed of matrices:

$$\mathbf{X} = \{\mathbf{x_n}\},\quad \mathbf{X_p} = \{\mathbf{x_{pn}}\}\ \text{ and }\ \mathbf{P_k} = \text{diag}(p_{kn})\,,$$

$$\mathbf{X_e} = \begin{bmatrix} \mathbf{X} & \mathbf{0} & \mathbf{0} & \mathbf{0} & \mathbf{P_1X_p} \\ \mathbf{0} & \mathbf{X} & \mathbf{0} & \mathbf{0} & \mathbf{P_2X_p} \\ \mathbf{0} & \mathbf{0} & \mathbf{X} & \mathbf{0} & \mathbf{P_3X_p} \\ \mathbf{0} & \mathbf{0} & \mathbf{0} & \mathbf{X} & \mathbf{P_4X_p} \end{bmatrix}.$$

The over-determined equation set (5) may be solved using a least squares method accounting for the constraints (4) [7]. For this purpose, we use the objective function:

$$\begin{aligned} L(\lambda, \beta) &= (\mathbf{y} - \mathbf{X_e}\boldsymbol{\beta})^\mathrm{T}\mathbf{W}(\mathbf{y} - \mathbf{X_e}\boldsymbol{\beta}) \\ &- \sum_k \lambda_k \boldsymbol{\beta}_\mathbf{k}^\mathbf{T}\mathbf{D}\boldsymbol{\beta}_\mathbf{k} - \lambda_r(\boldsymbol{\beta}_\mathbf{r}^\mathrm{T}\mathbf{D_r}\boldsymbol{\beta}_\mathbf{r} - \mathbf{e}\boldsymbol{\beta}_\mathbf{r})\,, \end{aligned} \tag{6}$$

where $\mathbf{W}$ is a diagonal weight matrix and the vector $\lambda = [\lambda_1\ \lambda_2\ \lambda_3\ \lambda_4\ \lambda_r]^\mathrm{T}$ comprises Lagrangian multipliers. We minimize (6) with a similar method as in [7] approaching the optimal solution iteratively. If the system is calibrated, reflection coefficients of measured devices are calculated in similar way as in [7].

5. Experimental results

For measurements, we arranged the interferometer in a measurement system shown in Fig. 4. The interferometer comprises the four-state shifter, a double directional

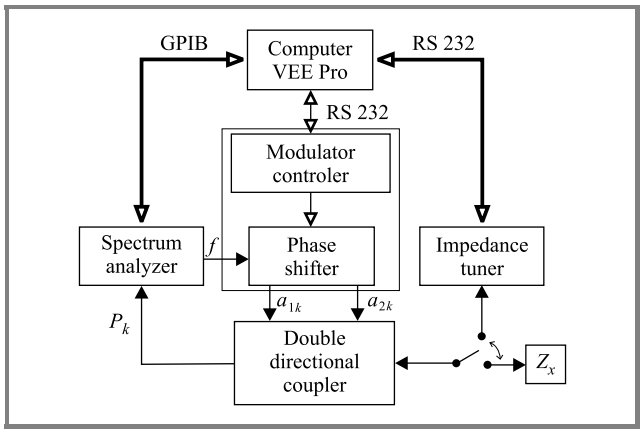


Fig. 4. Block diagram of the measurement system.

coupler and an HP8590L spectrum analyzer with in-built tracking generator. The generator stimulates the measurement circuit through phase shifter and the coupler while the spectrum analyzer measures the interfering waves at one port of the coupler's main line. The other port of this line is terminated with measured impedance Z_x. For the calibration, the system is equipped with an electronic impedance tuner that produces 36 known and repeatable values of the reflection coefficient [8]. All the system is controlled from a PC through GPIB and RS 232 communication buses using a program developed in VEE Pro environment [9].

The program enables user to perform the system calibration in two ways, with either a simplified or complete procedure. The simplified procedure assumes $\Gamma_{rk} = 0$ in the model (1) and in consequence $\boldsymbol{\beta}_\mathbf{r} = 0$ in (3)–(6). It may be, thus, applied to spectrum analyzers with well-matched input, e.g., using an attenuator. The simplified calculations go faster than in case of the complete procedure. This is achieved, however, at an expense of higher measurement

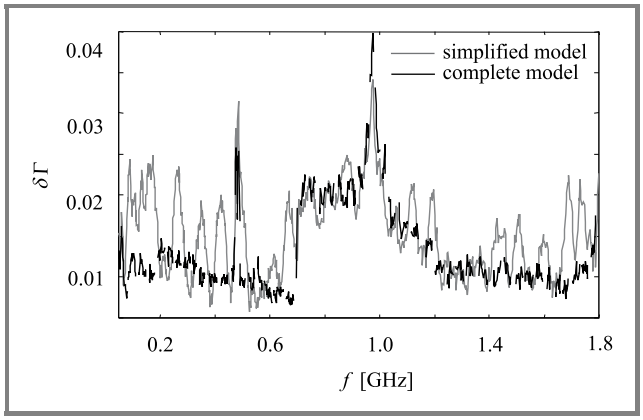


Fig. 5. Frequency dependence of the RMS error.

uncertainty. Figure 5 shows this with two traces each for different procedure.

The graph in Fig. 5 illustrates frequency dependence of the root mean square (RMS) error of the reflection coefficient measurement in the system. The RMS error is calculated from deviations of the reflection coefficient:

$$|\Delta\Gamma| = |\Gamma_{MIF} - \Gamma_{VNA}|\,, \tag{7}$$

where Γ_{MIF} and Γ_{VNA} are the reflection coefficients measured using the multistate interferometer (MIF) and VNA, respectively.

The results shown in Fig. 5 refer all the reflection coefficients realized using the impedance tuner. The differences between both curves are not very pronounced due to the return loss of the receiver that was higher than 30 dB over the whole frequency range. Two prominent picks seen in the both curves are, perhaps, caused by interference coming from mobile communications bands. Thus except these two bands, the measurement uncertainty is less than 0.025.

6. Conclusions

We have presented a new multistate interferometer system for measuring vectorial reflection coefficient from 50 to 1800 MHz. The interferometer is composed of a four-state phase shifter that was designed in house, a double-directional coupler and a HP 8590L spectrum analyzer with an in-built tracking generator. The generator stimulates the measurement circuit through the shifter and the coupler while the spectrum analyzer measures the interfering waves in the coupler's main line. The reflection coefficient is determined from the measurements made for four phase states of the shifter. A PC controls the system and provides automation of the measurement process.

We described the design of the phase shifter, which was optimized in the whole frequency range to achieve the highest measurement accuracy as well as maintain low cost of the interferometer. The shifter's characteristics agreed well with the designed ones. We introduced also the technique we had developed for calibration of the system. The technique is based on a linear model and a LSQ method accounting for nonlinear constraints, which reduces the number of identified system parameters. We performed reflection coefficient measurements using the system and compared them with similar measurements made using a VNA. The experimental results have validated both the technique and high system's performance.

References

[1] G. F. Engen, "The six port reflectometer: an alternative network analyzer", *IEEE Trans. Microw. Theory Techn.*, vol. MTT-25, pp. 1075–1080, 1977.

[2] L. C. Oldfield and J. P. Ide, "A multistate reflectometer", *IEEE Trans. Instr. Meas.*, vol. 34, pp. 486–489, 1985.

[3] T. Morawski and M. Sypniewski, "AM/PM switched three port reflectometer", in *2nd Int. Symp. Meas. Electr. Quant.*, Warsaw, Poland, 1987, pp. 593–599.

[4] M. Szmidt-Szałowski and W. Wiatr, "A broadband design of a PM/AM switch for reflectometer system", in *Proc. 10th Microw. Conf. MIKON'94*, Książ, Poland, 1994, pp. 165–170.

[5] S. Li and R. G. Bossisio, "Calibration of multiport reflectometers by means of four open/short circuits", *IEEE Microw. Theory Techn.*, vol. 30, pp. 1085–1089, 1982.

[6] G. F. Engen, "Calibrating the six-port reflectometer by means of sliding terminations", *IEEE Trans. Microw. Theory Techn.*, vol. 26, pp. 951–957, 1978.

[7] W. Wiatr, "The multi-state radiometer: a novel means for impedance and noise temperature measurement", *IEEE Trans. Instr. Meas.*, vol. 46, pp. 486–489, 1997.

[8] D. Pieńkowski and W. Wiatr, "Broadband electronic impedance tuner", in *Proc. 14th Int. Microw. Conf. MIKON 2002*, Gdańsk, Poland, 2002, pp. 310–313.

[9] VEE Pro User' Guide. Agilent Techn. Inc., Santa Clara, CA, USA, 2000.



Piotr Szymański received the M.Sc. degree in electronic engineering from Warsaw University of Technology, Poland, in 2003. Since 2001, he has been with Telecommunications Research Institute (PIT), Poland. His current research include microwave circuits analysis and microwave measuerment system design. He is also interested in electronic support measures (ESM) systems and MMIC technology.
e-mail: szymanskip@pit.edu.pl
Telecommunications Research Institute
Poligonowa st 30
04-051 Warsaw, Poland

Wojciech Wiatr – for biography, see this issue, p. 22.

Paper

Absorption of EM energy by human body in the vicinity of the GSM base station antenna

Dariusz Wójcik, Tomasz Topa, and Krzysztof Szczepański

Abstract— A hybrid method is proposed for specific absorption rate analysis in a human body located in the near field of typical GSM base-station panel antenna. The method combines FDTD technique with analytical description of the near field of isolated antenna. The approximate results are found to be in excellent agreement with the results obtained by using the traditional FDTD. The most important advantage of proposed approach is minimization of computer memory requirements and computation time.

Keywords— cellular telephony, GSM, human exposure to EM fields, antennas, near field, specific absorption rate.

1. Introduction

According to International Commission on Non-Ionizing Radiation Protection (ICNIRP) guidelines [1] and IEEE standards [2], to evaluate exposure conditions to EM fields specific absorption rate (SAR) must be calculated. It is advisable to use full-wave numerical methods to evaluate SAR [4]. Finite-difference in time domain (FDTD) method seems to be the most frequently used approach in such cases. The method has been successfully applied to evaluate exposure conditions in far-field of antennas [6], where plane-wave excitation can be assumed. However, evaluation of SAR in the vicinity of GSM base-station antenna using classical FDTD usually cannot be performed due to computational limitations. Since the FDTD domain should enclose antenna as well as human body phantom, while the distance between them increases the computer storage requirements and computational time grow rapidly. To overcome the limitations mentioned above, parallel FDTD tool using super-computing platforms has been proposed [8]. For the same purpose, hybrid method, combining method of moments (MoM) with finite elements method (FEM) has been employed [9].

In this paper, another hybrid approach to evaluation of human exposure conditions in near field of typical GSM base station panel antenna is proposed. The method combines FDTD [7] with analytical description of antenna's near field. To evaluate near field of the antenna, its discrete model is employed [10, 11, 12]. It must be stressed, that proposed approach can be used to evaluate exposure conditions even when antenna's geometry is not exactly known, while all needed parameters of antenna's model can be obtained form the catalogue data only. For proposed hybrid method, computer requirements are independent of the distance between antenna and human body phantom.

2. Method description

In this section proposed hybrid method for evaluation human exposure conditions in near field of GSM antennas is described. The approximate results are compared with those obtained using traditional FDTD method. Because of huge computer memory requirements for traditional FDTD, derivation of the method and its validation is carried out for simple, rectangular box human phantom. Dimensions of the phantom (height $\times$ width $\times$ thickness = $80 \times 50 \times 20$ cm) correspond roughly to dimensions of adult man's trunk, and its electrical parameters ($\varepsilon_r = 42$, $\sigma = 0.97$ S/m) – to average parameters of human body for 900 MHz. The same fantom is recommended for SAR measurement procedure [4].

Let us consider the situation depicted in Fig. 1. The phantom is located centrally in front of 730370 antenna [15]. This antenna is widely used in GSM 900 base-stations. When the human phantom is located close to the source (in near field), significant influence on antenna parameters is expected. To examine this coupling phenomena, input admittance of the antenna as a function of the distance between antenna and phantom has been calculated.

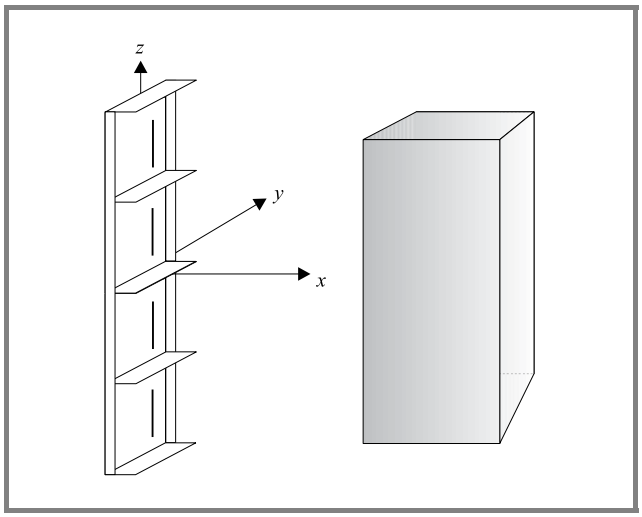


Fig. 1. Rectangular box phantom in the vicinity of GSM panel antenna.

The results are presented in Fig. 2. As can be observed, if the distance is greater then approximately 0.7–0.8 m, the phantom influence can be almost completely omitted.

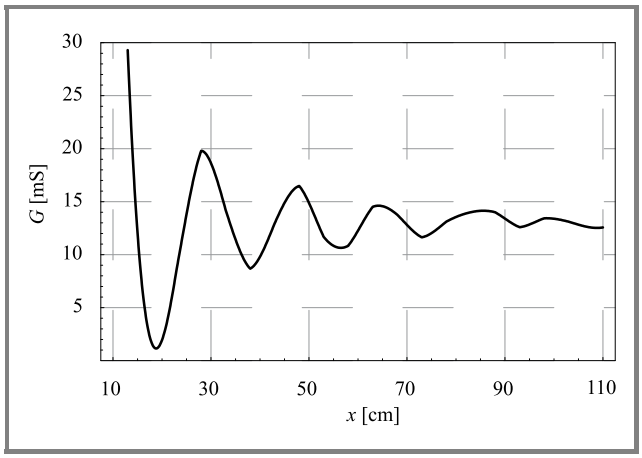


Fig. 2. Input conductance of panel antenna as a function of the distance between antenna and phantom.

The total field in the vicinity of the phantom can be treated as sum of incident field (E^i, H^i), produced by current flowing in the antenna, and scattered field (E^s, H^s), resulted from interaction of incident field with the phantom. If the influence of the phantom is negligible, current distribution in the antenna is such as current distribution in separated antenna. In such cases incident field can by successfully calculated using so-called discrete model [10]. Panel antennas, which seem to be the most popular for GSM 900 MHz as well as for GSM 1800 MHz base stations, are made up of identical "cells" (see Fig. 1). Each cell consists of several dipoles placed in front of a reflector. In discrete model, the original antenna is replaced with discrete linear array, where each cell is modelled by one source. The total field is calculated as a sum of the fields radiated by sources. The field of each source is obtained using far-field formulas. The model gives excellent results if observation point is located at the distance grater then $\sim 2\lambda$ from the antenna. All needed parameters of discrete model can be evaluated from catalogue data of the antenna only [10, 13, 14]. Thus, the model can be used for fast calculation of incident field even if antenna's geometry is not exactly known. To evaluate exposure conditions, knowledge of total field only inside human phantom is needed. Consequently, if discrete model is employed for incident field calculation, problem space for FDTD method can be significantly reduced to the nearest vicinity of the phantom, as it is illustrated in Fig. 3. It results in decrease of needed computer memory and time of computations. In this paper FDTD formulation for total/scattered field is used. Thus, discrete model is employed only for calculation of incident field on the Huygens boundary between regions. To extend FDTD domain to infinity, Berenger's perfectly matched layer (PML) [7] has been used.

In order to validate the proposed method, approximate results has been compared with those obtained using classical FDTD. Calculations has been carried out for numerous distances between antenna and phantom. In Fig. 4, electric field intensity inside the phantom along its symmetry axis is presented. Total power absorbed by the phantom as a function of distance is depicted in Fig. 5. As can be

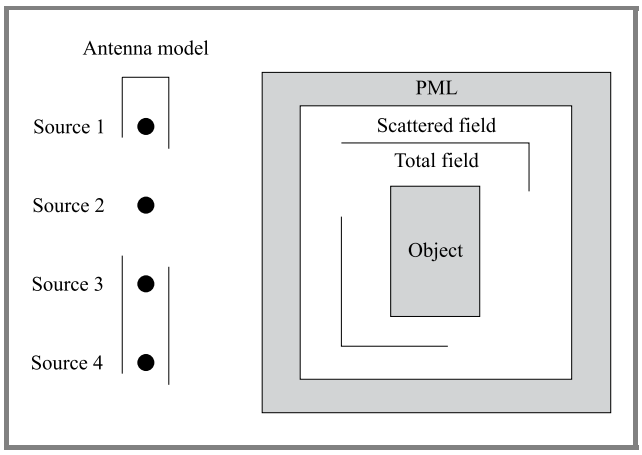


Fig. 3. Problem space for proposed hybrid method.

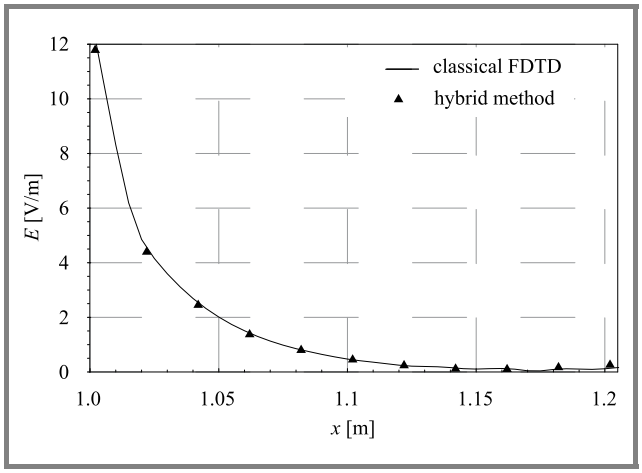


Fig. 4. Electric field intensity [V/m] inside the phantom along its symmetry axis.

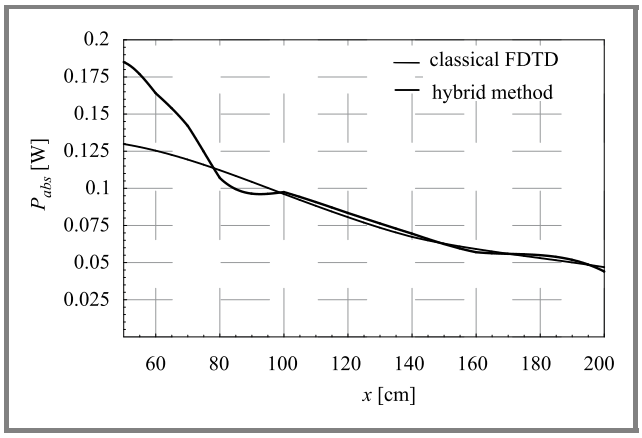


Fig. 5. Total power [W] absorbed by the phantom as a function of the distance ($f = 900$ MHz, $P_{in} = 1$ W).

easily observed, excellent agreement has been obtained for the distances greater then ~ 0.9 m.

3. Results

To study exposure conditions in the near field of base station antenna heterogenous model of man has been used. The computer phantom, which has been developed by visible human data [16] and provided by American National Library of Medicine, carries information about parameters of 39 different types of tissues. Used model is made up of $196 \times 114 \times 626$ voxels with 3 mm resolution.
The following conditions have been considered. The phantom faces the 730370 antenna, so that the maximum of radiated field can be observed at head-level. The distance between the antenna and the phantom was being changed from 0.75 m to 10 m, which is far field boundary according to classical $2D^2/\lambda$ criterion [5], with 0.25 m step. For each distance electric field intensity E in human body was calculated and then SAR distribution was obtained:

$$\mathrm{SAR} = \sigma E^2/\rho\,,$$

where σ and ρ denote conductivity and density of the tissue, respectively. Then, the results was compared to safety guidelines. IEEE and ICNIRP restrictions are based on limitation of whole-body SAR and local SAR for any 10 g [1] or 1 g [2] of continuous tissues. To select a tissue volume of the specified SAR-averaged-mass, the techniques described in [3] has been employed. According to [3] only a 5% deviation of demanded mass is permitted, and a tissue volume must have a cubical shape. It is easy to satisfy such conditions if a 10 g mass averaging is evaluated. Some difficulties may occur when a 1 g mass average SAR evaluations have to be proceeded, because of a 3 mm phantom resolution. If it is not possible to reach the desired value of the required mass in cubical volume, the following method has been developed. All the voxels in the vicinity of centered location [3] have been divided into 27 subvoxels. Each subvoxel has mass equal to 1/27 mass of a basic voxel, and a resolution of 1 mm. Thus, it is possible to create a precise cube with a required mass of tissue. In Figs. 6 and 7 SAR distribution in two cross-sections of the man model located at the distance of 1.5 m are presented for power radiated by the antenna equals to 10 W.

Table 1
Tissues with most intensive power absorption

Part of body	$\mathrm{SAR_{tis}/SAR_{wb}}$				
	Distance [m]				
	0.6	1.5	3.5	6.0	8.0
Eye lens	26.71	40.53	32.52	23.61	19.26
Eye cornea	18.67	27.91	22.24	16.16	13.15
Eye aqueous humor	14.19	22.05	17.70	12.85	10.47
Eye sclera/wall	11.73	18.23	14.82	10.63	8.71
Pituitary gland	10.92	15.81	12.77	9.31	7.62

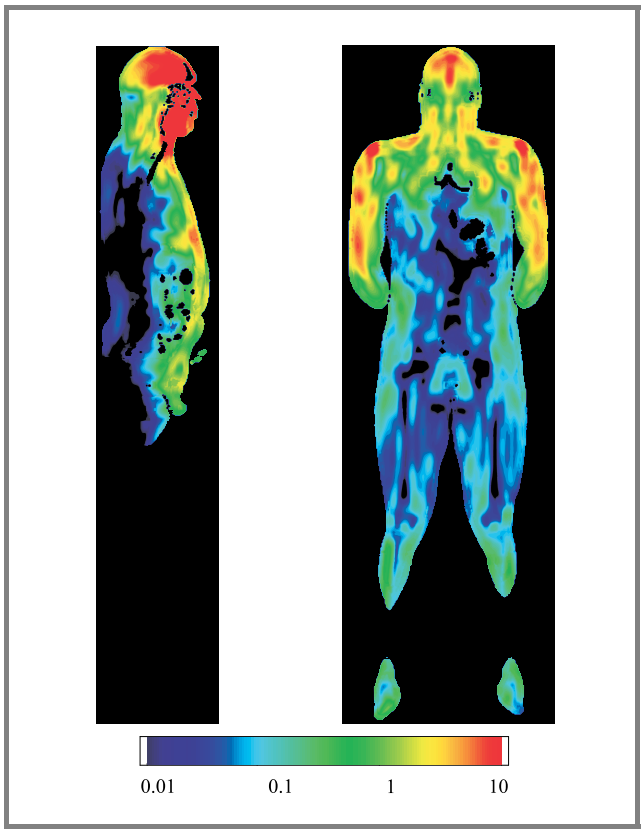


Fig. 6. $\mathrm{SAR_{1g}}$ distribution on sagittal and coronal views for distance 1.5 m ($f = 900$ MHz, $P_{in} = 10$ W).

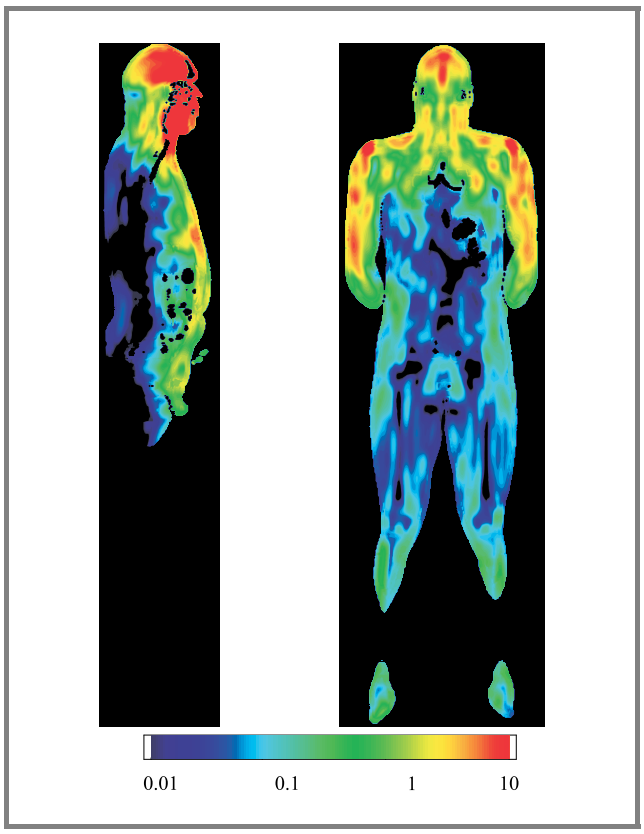


Fig. 7. $\mathrm{SAR_{10g}}$ distribution on sagittal and coronal views for distance 1.5 m ($f = 900$ MHz, $P_{in} = 10$ W).

For each considered distances most of electromagnetic energy is absorbed by muscles ($\sim 40\%$), fat ($\sim 25\%$) and skin ($\sim 5\%$). The investigation also shows that except brain and eyes, the other body organs are strongly protected by tissue layers such as muscle, fat, bone and skin. Some brain and eye-tissues absorb EM energy significantly more intensively compared with the rest of the body, as it is presented in the Table 1. Maximal local SAR values are concentrated around the head and chest, where distinct hot-spots can be observed. For example maximum local SAR is localized in eye when the distance between model and antenna is equal to 1.5 m. When the distance is increased to 8 m maximum local SAR occurs in muscle of chest.

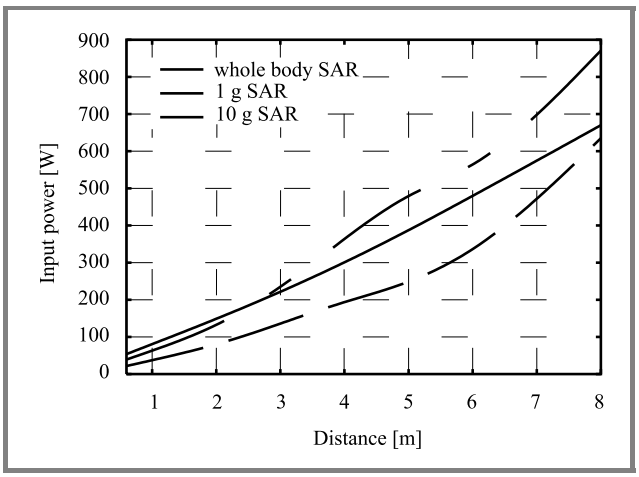


Fig. 8. Antenna input power needed to exceed SAR restrictions.

The results depicted in Fig. 8 show minimal antenna input power which makes the SAR restriction to be exceeded. As can be observed, to reach 1 g SAR restrictions the smallest input power level is sufficient. 10 g restrictions play important role close to antenna only – if the distance is greater then about 3 m whole-body SAR restrictions dominate.

4. Conclusion

In this paper hybrid method for specific absorption rate calculation in near field of GSM panel antenna is proposed. The method combines FDTD technique with analytical description of the near field of isolated antenna. The approximate results are found to be in excellent agreement with the results carried out by using the traditional FDTD. Obtained results show, that comparatively high SAR level can be observed in brain and eye tissues. However, it is also presented, that SAR restrictions can be exceeded if input power of the antenna is relatively high compared to its typical values (about 40 W).

References

[1] "ICNIRP Guidelines. Guidelines for limiting exposure to time-varying electric, magnetic, and electromagnetic fields (up to 300 GHz)", *Health Phys.*, vol. 47, no. 4, pp. 494–532, 1998.

[2] "IEEE Standard for safety levels with respect to human exposure to radio frequency electromagnetic fields, 3 kHz to 300 GHz", IEEE Std. C95.1, 1999.

[3] "IEEE Recommended Practice for Measurements and Computations of Radio Frequency Electromagnetic Fields with Respect to Human Exposure to Such Fields, 100 kHz–300 GHz", IEEE Std. C95.3–2002, 11 Dec. 2002.

[4] "Basic standard for the calculation and measurement of the human exposure to electromagnetic fields from radio base stations and fixed terminal stations for wireless telecommunication systems (110 MHz to 40 GHz)", TC 211, EN 50383.

[5] C. A. Balanis, *Antenna Theory. Analysis and Design*. New York: Wiley, 1997.

[6] P. Bernardi, M. Cavagnaro, S. Pisa, and E. Piuzzi, "Human exposure to radio base-station antennas in urban environment", *IEEE Trans. Microw. Theory Techn.*, vol. 48, no. 11, pp. 1996–2001, 2000.

[7] A. Taflove and S. C. Hagness, *Computational Electromagnetics: The Finite–Difference Time–Domain Method*. Boston, London: Artech House, 2000.

[8] L. Catarinucci, P. Palazzari, and L. Tarricone, "Human exposure to the near field of radiobase antennas – a full wave solution using parallel FDTD", *IEEE Trans. Microw. Theory Techn.*, vol. 51, no. 3, pp. 935–940, 2003.

[9] R. J. Spiegel, M. B. A. Fatmi, S. Stuchly, and M. Stuchly, "Comparison of finite-difference time-domaim SAR calculations with measurements in a heterogeneous model of man", *IEEE Trans. Biomed. Eng.*, vol. 36, no. 8, pp. 849–858, 1989.

[10] M. Bizzi and P. Gianola, "Electromagnetic fields radiaed by GSM antennas", *Electron. Lett.*, vol. 35, no. 11, pp. 855–857, 1999.

[11] R. Mawrey, T. Riley, J. Higgins, and S. Slayden, "Pedicting power density near antennas to met FCC RF safety regulation", *Mob. Radio Technol.*, pp. 36–47, Sept. 1997.

[12] D. Wójcik, "Evaluation of near field of the GSM base station antennas in urban environment", *J. Telecommun. Inform. Technol.*, no. 1, pp. 41–44, 2003.

[13] D. Wójcik, "Near field of the base-station antennas of the cellular thelephony" , Ph.D. thesis, Gliwice, Silesian University of Technology, 2004 (in Polish).

[14] D. Wójcik, "Simply method for evaluation of the near field of the GSM base-station antennas", in *17th Int. Wroclaw Symp. Exhib. Electromagnet. Compat.*, Wrocław, Poland, 2004, pp. 127–130.

[15] "Kathrein – Antennas for Mobile Communications". Version 4, Ed. 05/00.

[16] "The Visible Human Project", http://www.nlm.nih.gov/research/visible/visible_human.html



Dariusz Wójcik was born in Czeladź, Poland, in 1974. He received the M.Sc. degree in telecommunications and Ph.D. degree in radiocommunications from the Silesian University of Technology, Gliwice, Poland, in 1999 and 2004, respectively. His professional interests are primarily in computational electromagnetics (MoM, FDTD, hybrid methods) and radiocommunications.
e-mail: dariusz.wojcik@polsl.pl
Institute of Electronics
Silesian University of Technology
Akademicka st 16
44-100 Gliwice, Poland



Tomasz Topa was born in Tarnowskie Góry, Poland, on April 8, 1977. He received the M.Sc. degree in telecommunications from Silesian University of Technology, Gliwice, Poland, in 2002. His current research interests include electromagnetic field theory, numerical dispersion, perfectly matched layers in FDTD method, the FDTD method, and electromagnetic compatibility.

e-mail: tomasz.topa@polsl.pl
Institute of Electronics
Silesian University of Technology
Akademicka st 16
44-100 Gliwice, Poland



Krzysztof Szczepański was born in Będzin, Poland, in 1978. He received the M.Sc. degree in telecomunications from Silesian University of Technology, Gliwice, Poland, in 2003. His main research interests are computational electromagnetic and electromagnetic compatibility.

e-mail: krzysztof.szczepanski@polsl.pl
Institute of Electronics
Silesian University of Technology
Akademicka st 16
44-100 Gliwice, Poland

Paper

Characterization of an aperture-stacked patch antenna for ultra-wideband wearable radio systems

Maciej Klemm and Gerhard Troester

Abstract— This paper presents, for the first time, the time-domain characteristics of an aperture-stacked patch antenna (ASPA) for ultra-wideband (UWB) wearable devices. The methodology of antennas characterization for UWB radio systems is also outlined. The antenna operates within the 3–6 GHz frequency band. Time- and frequency-domain characteristics of this antenna are presented in transmission mode (Tx), receiving mode (Rx) and for 2-antenna (Tx-Rx) system. The pulse driving the antenna has duration of 0.65 ns. In the Tx mode, pulses radiated in different directions of the H-plane have very similar shapes. Fidelity factors are as high as 91.6–99.9%. For 2-antenna system, pulses received in normal and end-fire-like directions have the fidelity of 69.5%. As it was found, antenna does not behave "reciprocal" comparing Tx and Rx modes. For normal propagation direction, radiated pulse is the 2nd derivative of the input waveform, but in the Rx mode, received pulse is the 1st derivative of the incident plane wave. This antenna can be used for transmission of short-pulses, even 0.65–1 ns in duration. It is also small (patch planar dimensions 32/19 mm) and compact. Microstrip configuration allows further integration of active devices on the same board. Taking into account above results we can say that ASPA is a good candidate for UWB non-invasive wireless body area network (WBAN) applications.

Keywords— ultra-wideband, UWB, ultra-wideband antennas, ultra-wideband communication.

1. Introduction

Ultra-wideband (UWB) communication systems have recently received more and more attention in the wireless world. Their envisioned advantages over conventional wireless communication systems are: extremely low power consumption, high data rates and simple hardware configuration. UWB radio is characterized by a wide signal spectrum and low radiated power spectral density (for FCC regulation refer to [2]). The most interesting approach of the UWB radio system is so-called **impulse radio** [3]. Its basic concept is to transmit and receive very short electromagnetic pulses (few tens of picoseconds to few nanoseconds in duration), where the pulse shape is a crucial information. Antennas play a critical role in UWB communication systems since they influence the complexity of the receiver and transmitter (pulse generator). Generally, ordinary wideband antennas will not transmit short pulses without distortions. Good examples are well-known broadband radiators: log-periodic and spiral antennas. They can be called ultra-wideband in terms of the input matching and radiation characteristics, but since they radiate different frequency components from different parts of the antenna, fast transient waveforms are distorted and stretched out [4, 5]. Other radiators (e.g., bow-ties or dipoles) use resistive loading to improve transient characteristics, but at the cost of the radiation efficiency.

Design of the ultra-wideband antenna for UWB wearable devices is even more challenging. The antenna is mounted on the human body and more aspects are of great importance: antenna dimensions, possibilities of integration into the clothing, human body influence on the antenna characteristics and also on the short-pulses propagation.

Our research interests concern antennas for non-invasive wireless body area networks (WBAN) [1]. WBAN nodes are usually placed close to the body, on or in everyday clothing. It has some distinct features from other wireless networks, which are also constraints for antenna designs: close proximity of the human body (electromagnetic "pollution" should be extremely low), low transmitting power, possibly low radiation towards body. From the practical point of view, aperture-stacked patch microstrip antenna is a very attractive candidate for WBAN applications (is small and compact, do not radiate significant power into the human body). Moreover, its wideband matching and radiation characteristics were reported [6]. To make sure that ASPA is suitable for UWB (pulsed) WBAN wearable radios, we have investigated its transient characteristic.

2. Antennas in UWB systems

Characteristic parameters of antennas for UWB communication differ from those known from the classical antenna theory. The classic concepts of return loss, gain, and radiation pattern are not applicable to pulsed antennas. Return loss still can be useful in guiding the efficiency, but is no longer a useful measure to characterize short-pulse radiation. Typical antenna parameters for UWB radio systems are described in [7, 8].

Figure 1 schematically presents components of a UWB radio link, which can be equally characterised in the time- or frequency-domain. $X(f)$ represents the signal created in the pulse generator, which feeds the transmit (Tx) antenna. Next, we have 3 transfer functions: $H_{tx}(f)$ stands for the Tx antenna transfer function, $h_{ch}(t)$ indicates channel

characteristics, $H_{rx}(f)$ is the receiving (Rx) antenna transfer function. All these functions are not only time (frequency) dependent, but depend also on the direction of the signal propagation.

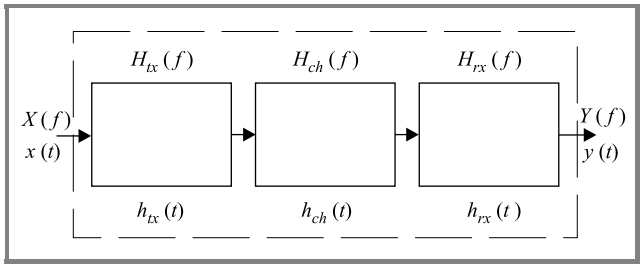


Fig. 1. Schematic of the UWB communication link.

The characteristic feature in the UWB radio systems is that an antenna must be designed taking into account the entire system. For the particular waveform driving different antennas, in the receiver we will get different pulse shapes. Thus, depending on the receiving method, the system performance will vary and in the worst case it can even stop working. This can be the case for the template receiver (e.g., Rake), where the received waveform in compared with the reference pulse. For this kind of receiver, its complexity will depend on the excitation pulse and the antennas

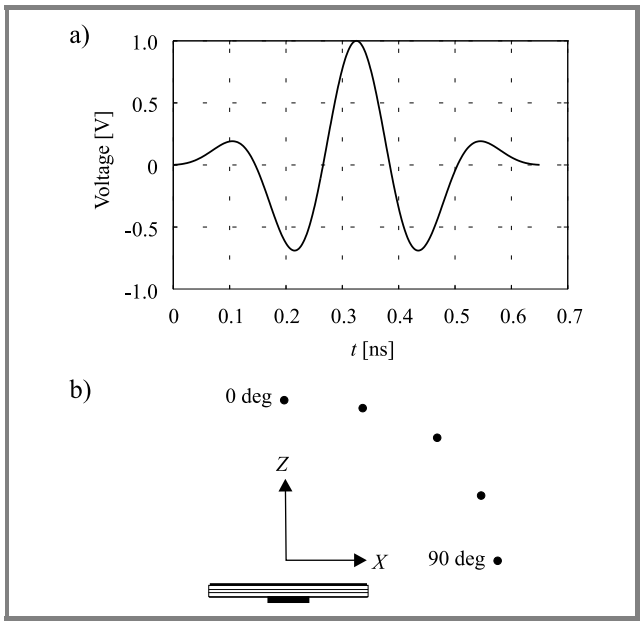


Fig. 2. (a) Excitation pulse driving the antenna; (b) time-domain electric field probes.

used. From the other side, for the same kind of the template receiver, one could assume different approach. To achieve the simplest detection, one can define the received pulse shape $y(t)$, and based on the known function $h(t)$, one could calculate desired excitation $x(t)$. So, in this case we could achieve the simple receiver, but since $x(t)$ can be the arbitrary waveform, pulse generation can become quite complicated. For our investigations we have used the pulse, which comprise trade-off between transmitter and receiver complexities.

Figure 2 presents the excitation pulse (with duration of 0.65 ns and time-domain probes, 20 cm from antenna) used within simulations to find Tx transfer functions for different directions. The pulse was created by the method described in [9]. In this method, for a given duration of the pulse and a limited signal bandwidth we get the set of orthogonal pulses.

3. Antenna design

The geometry of the aperture-stacked patch microstrip antenna is shown in Fig. 3. It differs from typical aper-

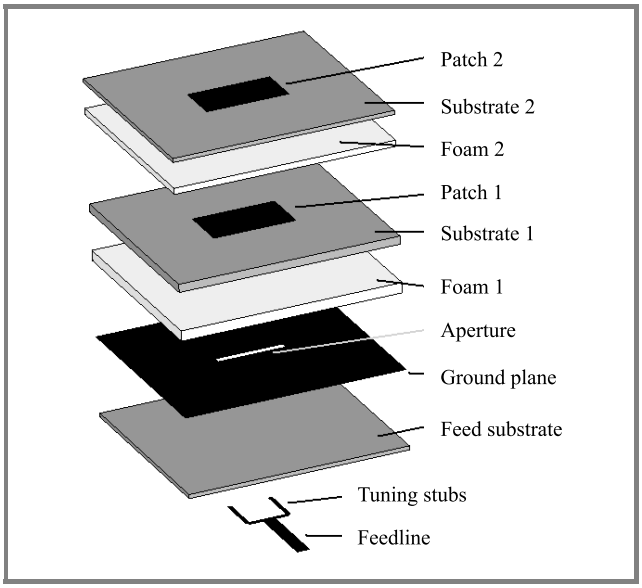


Fig. 3. Geometry of an aperture-stacked patch antenna.

Table 1
Dimensions of the ASPA and materials

Element	h [mm]	ε_r	tan δ
Feed substrate	1.58	2.2	0.0009
Foam substr. 1	4	1.07	0.0009
Substrate 1	3.175	2.2	0.0009
Foam substr. 2	2.4	1.07	0.0009
Substrate 2	1.58	2.2	0.0009
	width [mm]	length [mm]	
Feed-line	4.8	–	
Stubs	1.4	7.4*	
Patch 1	32	19	
Patch 2	32	17	

* Distance from the open-end of a stub to the aperture centre.

ture-coupled patch antennas in that a larger aperture and thicker substrates with low dielectric constants have to be used. Because the aperture in the ASPA is also used as a radiator, dual-offset tuning stubs control the coupling from the feed-line. Length and distance between them are one of the important parameters to achieve broadband characteristics. For our application, we have designed the ASPA for a frequency range from 3 to 6 GHz, considering the input matching. Referring to the antenna geometry from Fig. 3, the antenna dimensions are shown in Table 1.

4. Antenna characteristics

The antenna was designed and analysed with the aid of the commercial time-domain simulator CST microwave studio (finite integration (FI) method). All the necessary frequency domain parameters were calculated applying the Fourier transformation.

4.1. Frequency domain (FD) characteristics

The measured and simulated return losses (RL) of the ASPA (with a ground plane size of 70×70 mm) are shown in Fig. 4. The RL 10 dB bandwidth is from around 3 to 6 GHz, what is sufficient for our application. A small difference between both RL characteristics is a result of the additional SMA connector used in the measurements.

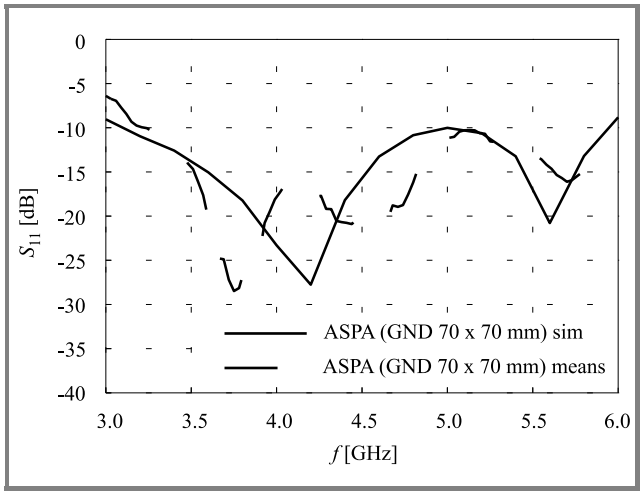


Fig. 4. Measured and simulated input matching of the ASPA.

The $H_{tx}(f)$ transfer function in different radiation directions (see Fig. 2b) is shown in Fig. 5. The 0 deg indicates radiation perpendicular to the patch surface (normal mode), 90 deg is for end-fire-like propagation (what can represent, e.g., communication between antennas placed along the human body). Since the antenna has the linear polarisation, all results are shown for a dominant electric field component. The distance from the antenna to electric field probes is 20 cm.

From Fig. 5a we can see that the transfer function is flat (max. variations 3 dB) within 3–6 GHz bandwidth, for 0–45 deg directions. Together with linear phase for these

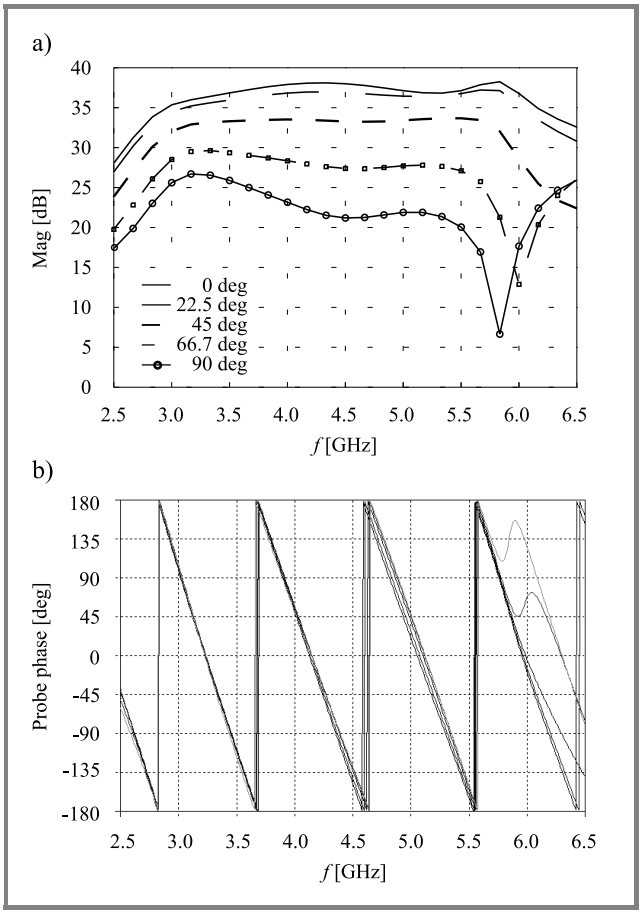


Fig. 5. Antenna FD transfer function $H_{tx}(f)$ in different propagation directions: (a) amplitude; (b) phase.

directions (Fig. 5b) this indicates that the pulse components in this range are radiated without distortions. For radiation at angles between 66.7 and 90 deg, we can see a notch (6 and 5.8 GHz) in the amplitude characteristic of the $H_{tx}(f)$, which causes also nonlinear phase response. The same effect can be seen in Fig. 6, where we have $H_{rx}(f)$ and $H(f)$ (2-antenna) transfer functions. This result probably from the slot radiation. For these directions on the frequencies where the notch occurs, waves radiated from 2 slot edges have aprox. 180 deg phase difference. For the worst case, end-fire-like (90 deg) propagation direction, variations in the amplitude of $H_{tx}(f)$, $H_{rx}(f)$ and $H(f)$ (for 3–6 GHz range) are 20, 30 and 47 dB, respectively. This suggests that the pulse will suffer from distortions. For 0 deg direction, these variations are very small, not higher than 4 dB for all transfer functions ($H_{tx}(f)$, $H_{rx}(f)$ and $H(f)$). Interesting to notice is the fact that $H_{tx}(f)$

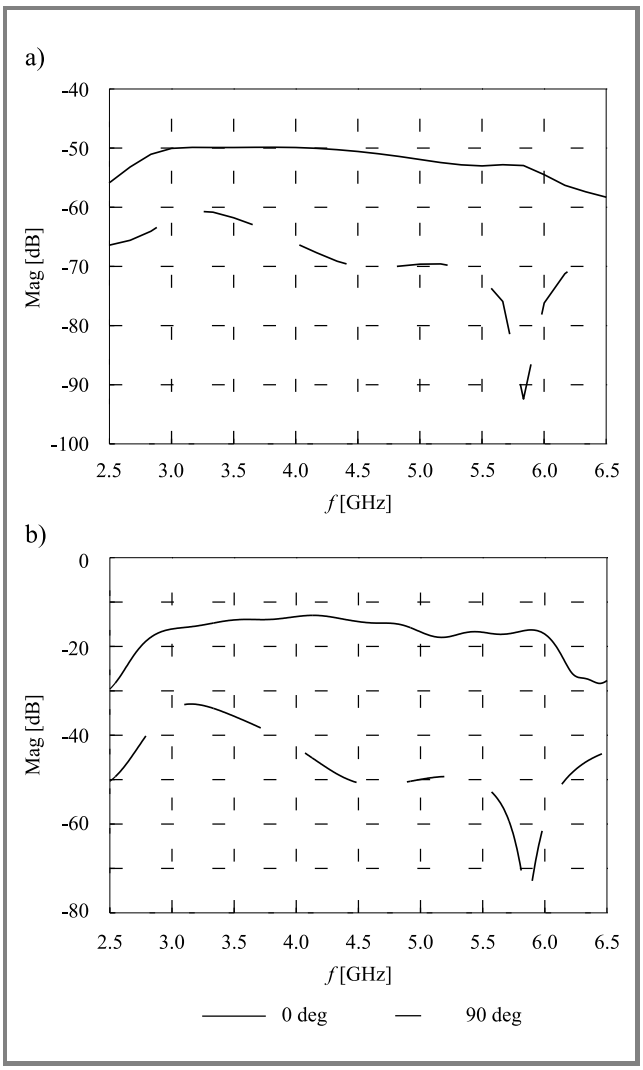


Fig. 6. ASPA transfer functions: (a) $H_{rx}(f)$ – Rx mode; (b) $H(f)$ – 2-antenna system.

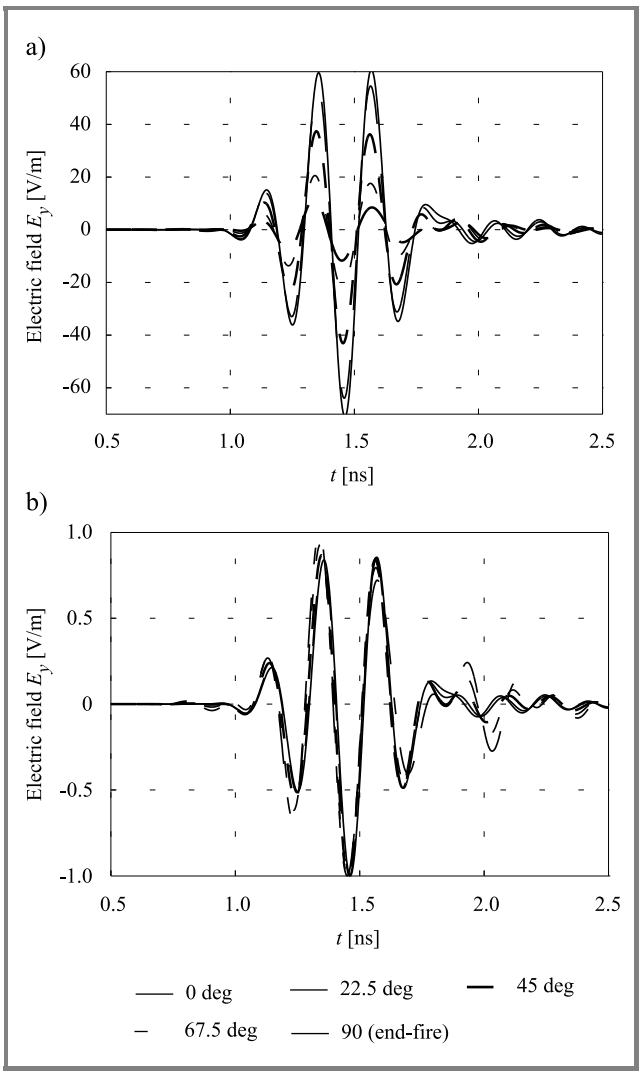


Fig. 7. Radiated pulses (Tx mode): (a) absolute values; (b) normalised values.

and $H_{rx}(f)$ functions are not the same, thus indicating differences in the antenna transmission and reception behaviours. As we will see in the next paragraph this fact has great influence on the pulse shapes.

4.2. Time domain (TD) characteristics

In Fig. 7 we present radiated pulses in five different directions, when the ASPA was excited by the pulse from Fig. 3a. Figure 7 shows absolute and normalized (to the maximum) values of electric field intensity of radiated pulses, respectively. From Fig. 7b we can see the fidelity (pulse shape changes in different propagation directions) of the pulses. Assuming as a reference pulse radiated in a normal direction, the fidelities are 99.9, 99.2, 97 and 91.6% for directions 22.5,45, 66.7 and 90 deg, respectively.

All pulses are very similar, nevertheless for 66.7–90 deg directions we can see the late-time ringing, caused by the notch and nonlinear phase of the Tx transfer function ($H_{tx}(f)$). To avoid pulse distortions, antenna for UWB systems should have the linear phase response. This is even better visible when looking at the pulse shapes (normalized) at the terminals of the receiving antenna (we used the same ASPA in Tx and Rx modes) from Fig. 8. They differ not only in the shape, but also in the duration. Their fidelity is only 69.5%, their duration (counted for the 10% of a V_{max}) is 0.89 and 1.62 ns, for normal and end-fire-like directions, respectively. The longer pulse duration for 90 deg indicates lower achievable data-rates; its complicated shape (more zero-crossing points within the effective duration of the pulse) can make the detection process more difficult (e.g., more fingers for the Rake receiver).

In the UWB transmitter-receiver system, output signals can be (with some assumptions) often approximated by several time derivatives of the input driving pulse (e.g., output waveform from the 2 electrically small Tx-Rx dipoles is a 3rd derivative of the input pulse) [10, 11]. But if the antennas are not electrically small (e.g., horn or reflector antennas) they can have no influence on the pulse shape.

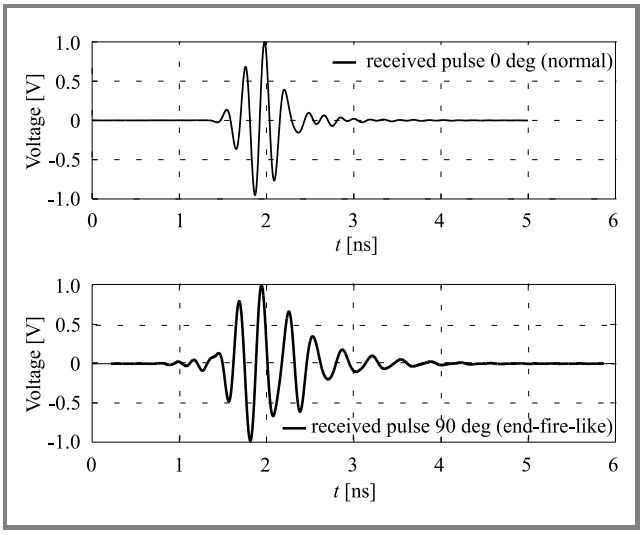


Fig. 8. Received pulses (the same ASPA used for Tx and Rx).

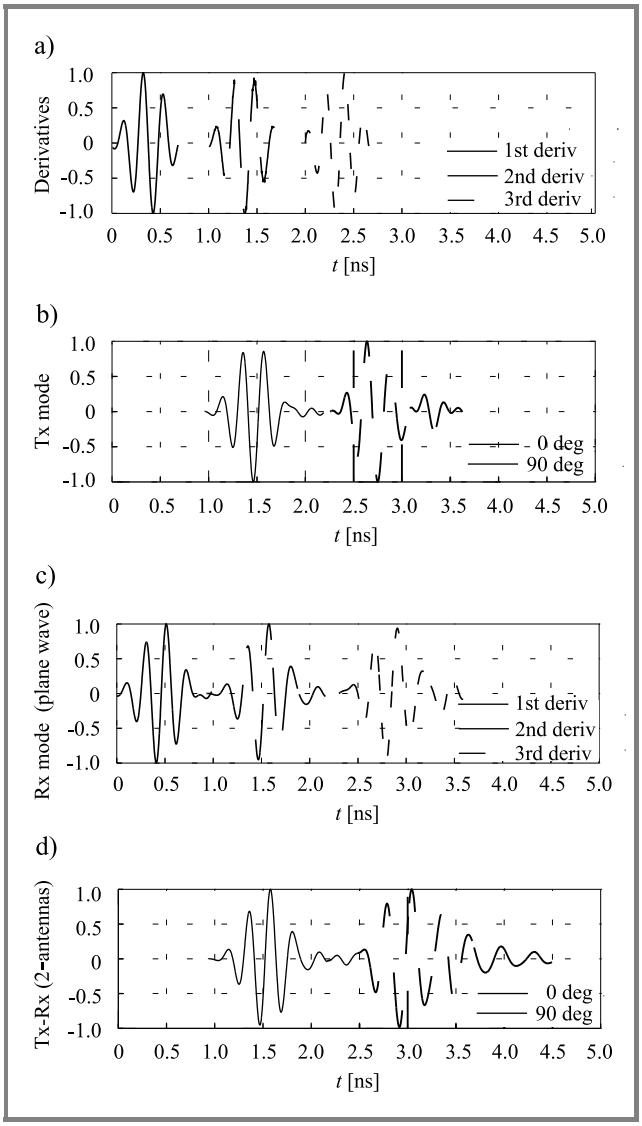


Fig. 9. Comparison between ideal derivatives of the antenna input waveform (Fig. 2a) and its output signal for different operating modes: (a) derivatives of the input pulse; (b) Tx mode; (c) Rx mode; (d) Tx-Rx mode (2 antennas).

Other behaviours, even integrations, are also possible. For that reason we have also investigated this aspect. Figure 9 presents comparison between ideal derivatives of input signal for Tx, Rx (input signal as a plane wave) and Tx-Rx modes. All pulses are normalised so that we can compare their shapes.

In Fig. 9a we have waveforms of the 1st, 2nd, 3rd derivative of the input pulse (Fig. 3a). Figure 9b presents radiated waveforms for 0 and 90 deg directions (the same as in Fig. 7). It can be seen that the pulse radiated in 0 deg direction is very similar to the 2nd derivative of the excitation. For 90 deg direction, excluding late-time distortions, the pulse is a good replica of the 1st derivative of the input waveform. This effect is very interesting, especially if we compare it with the results obtained for the Rx mode. In Rx mode, we have used plane wave excitation with the time shape as for the radiated pulse (Fig. 9b, left) in normal direction (0 deg). The left pulse in Fig. 9c is the 1st derivative of the plane wave pulse, next to it we see 2 received pulses. Unlike in the Tx mode, both pulses are very similar to the 1st derivative of the impinging plane wave. For 90 deg direction, pulse is stretched and distorted at the end, because of the notch in the Rx transfer function. These results show that the antenna is not "reciprocal" in Tx and Rx modes, if we look at the output waveforms (or frequency dependence of the respective transfer functions). Finally, for the entire Tx-Rx system, we can notice that: for 0 deg direction, the received pulse is the replica of the 3rd derivative of the input waveform; for 90 deg direction, the pulse is seriously distorted and stretched in time, and there is no simple relation with any of derivatives. This is the effect of the total system transfer function characteristic $H(f)$ (Fig. 6b, 90 deg). From Fig. 9 we can also say that the reception mechanism has the bigger influence of the pulse distortions, in the end-fire-like transmission direction.

5. Conclusions

In this paper we investigated the ASP microstrip antenna for UWB wearable applications. Based on the general methodology (using TD simulator), the most important parameters of the pulse antenna were found. Their knowledge is necessary to perform simulations of the UWB radio system, including pulse generator, UWB channel model and receiver front-end. It is very difficult to judge the pulse antenna performance, since it cannot be separated from the entire system. There is a clear call for the generator-antenna-receiver co-design in UWB radios. Because of the high fidelity of radiated pulses (above 90%), ASPA could be successfully used for transmitting-only nodes of the WBAN, in the case of on-the-body and body-environment communications scenarios. But it could also be used in both (Tx and Rx) modes, if we could

accept lower data-rates for end-fire-like direction (which is the case for on-the-body placed network nodes). In this case, the template receiver is probably not the best solution. Taking into account all practical requirements (small size and compactness), we can say that ASPA is a good candidate for UWB wearable radio systems. Further investigations will include influence of the human body on the antenna parameters and UWB signals propagation.

References

[1] T. Zasowski, F. Althaus, M. Stäger, A. Wittneben, and G. Tröster, "UWB for noninvasive wireless body area networks: channel measurements and results", in *IEEE Conf. Ultra-Wideband Syst. Technol.*, Reston, USA, 2003.

[2] Federal Communication Commission, "First Order and Report, revision of Part 15 of the Commissions Rules Regarding UWB Transmission Systems", FCC 02-48, Apr. 2002.

[3] M. Z. Win and R. A. Scholtz, "Impulse radio: how it works", *IEEE Commun. Lett.*, vol. 2, issue 2, pp. 36–38, 1998.

[4] W. Soergel, Ch. Waldschmidt, and W. Wiesbeck, "Antenna characterisation for ultra wideband communications", in *2003 Int. Works. Ultra Wideband Syst. IWUWBS*, Oulu, Finland, 2003.

[5] E. K. Miller and J. A. Landt, "Short-pulse characteristics of the conical spiral antenna", *IEEE Trans. Anten. Propagat.*, vol. 25, no. 5, 1977.

[6] S. D. Targonski, R. B. Waterhouse, and D. M. Pozar, "Design of wide-band aperture-stacked patch microstrip antennas", *IEEE Trans. Anten. Propagat.*, vol. 46, no. 9, 1998.

[7] Ch. Robin, S. Bories, and A. Sibille, "Characterisation tools of antennas in the time domain", in *2003 Int. Works. Ultra Wideband Syst. IWUWBS*, Oulu, Finland, 2003.

[8] A. Shlivinski, E. Heyman, and R. Kastner, "Antenna characterisation in the time domain", *IEEE Trans. Anten. Propagat.*, vol. 45, no. 7, 1997.

[9] B. Parr, B. Cho, K. Wallace, and Z. Ding, "A novel ultra-wideband pulse design algorithm", *IEEE Commun. Lett.*, vol. 7, no. 5, 2003.

[10] R. W. Ziolkowski, "Properties of electromagnetic beams generated by ultra-wide bandwidth pulse-driven arrays", *IEEE Trans. Anten. Propagat.*, vol. 40, no. 8, 1992.

[11] C. E. Baum, "General properties of antennas", *IEEE Trans. Electromag. Compat.*, vol. 44, no. 1, 2002.



Maciej Klemm was born in Kwidzyn, Poland, on September 7, 1978. He received the M.S.E.E. degree in microwave engineering from Gdańsk University of Technology, Gdańsk, Poland, in 2002. He is currently working toward his Ph.D. degree in electrical engineering at the Electronics Laboratory of the Swiss Institute of Technology in Zurich, Switzerland. His current research interests include microwave and millimetre-wave circuits design, ultra-wideband antennas, UWB communication systems, MCM technologies, computational electromagnetic methods and simulations.
e-mail: klemm@ife.ee.ethz.ch
Electronics Laboratory
ETH Zurich
Gloriastrasse 35
CH-8092 Zurich, Switzerland



Gerhard Troester received the M.Sc. degree from the Technical University Karlsruhe, Germany, in 1978 and the Ph.D. degree from the Technical University of Darmstadt, Germany, in 1984, both in electrical engineering. He is a Professor and head of the Electronics Laboratory, ETH Zurich, Switzerland. During the eight years he spent at Telefunken Corporation, Germany, he was responsible for various national and international research projects focused on key components for ISDN and digital mobile phones. His field of research includes wearable computing, reconfigurable systems, signal processing, mechatronics, and electronic packaging. He authored and co-authored more than 100 articles and holds five patents. In 1997, he co-founded the spinoff u-blox ag.
e-mail: troester@ife.ee.ethz.ch
Electronics Laboratory
ETH Zurich
Gloriastrasse 35
CH-8092 Zurich, Switzerland

Paper

Spatial power combiner using a planar active transmitarray of stacked patches

Feng-Chi E. Tsai and Marek E. Bialkowski

Abstract—An *X*-band spatial power combiner, which uses a planar transmitarray (TXA) of orthogonally polarized stacked microstrip patches integrated with input and output ports of transistor amplifiers is described. In order to obtain an increased operational bandwidth, the unit cell of the combiner with various stacked patch (SP) configurations is investigated. The configuration showing the smallest insertion losses is chosen for developing a TXA. The constructed spatial combiner includes a 4×4 cell TXA placed between two hard horn antennas. Its performance is assessed experimentally in terms of amplification gain and combining efficiency.

Keywords*— *active antennas, amplifiers, microstrip antennas, planar arrays, power combiners.

1. Introduction

A very rapid growth of terrestrial and satellite communications in the last few decades of the 20th century and the resulting heavy congestion of low microwave bands have been a major driving force for exploring upper microwave and millimetre-wave frequencies. One of the main requirements for a successful shift to the new frequency spectrum is availability of high power solid-state transmitters. Solid-state devices such as diodes or transistors are able to meet such demand when their output signals are combined using spatial power combining methods. These methods avoid conduction losses, which become pronounced at millimetre wave frequencies.

The space-level power combining was first demonstrated by Staiman *et al*. [1] in 1968. Since that time, varieties of spatial power combining structures have been proposed and established [2, 3]. Although at the initial stages both oscillators and amplifiers were considered, most of the recent activities have been devoted to amplifiers. This is because of the ease of their control and tuning. Due to the technological reasons most of recent investigations have been committed to planar, tile and tray, configurations of space-level combiners. The tile configuration offers the fully planar format and ease of development. Its disadvantage is due to narrow-band operation, which is caused by the narrow-band operation of typical planar antenna elements, which are employed in this type of power combiner [4–11].

The goal of the work undertaken here is obtaining an increased operational bandwidth of the tile type power combiner by employing stacked patch (SP) microstrip antennas [12] as receiving and transmitting elements in the active planar transmitarray (TXA). An *X*-band prototype, which can be easily scaled to higher frequencies, is investigated. First, various configurations of SP antennas for integration with amplifiers are studied in the unit cell arrangement. After making suitable selections, 4×4 cell passive and active SP TXA are designed and developed. Two identical hard horn antennas with an approximately uniform aperture field for signal launching and collecting complete the design of this space-level power combiner. Its performance is assessed in terms of amplification gain and combining efficiency.

2. Stacked patch antenna unit cell design

In order to develop an amplifying TXA with an increased operational bandwidth, edge-fed stacked patch (EFSP) and aperture-coupled stacked patch (ACSP) antennas for integration with input and output amplifier ports were selected and studied using the full-wave electromagnetic (EM) commercial simulation software, Ensemble® of Ansoft®. The investigations were performed at 10 GHz by assuming 9.5 GHz as the design frequency. The full design details of the chosen antennas were reported in [13] and are not repeated here. The 10 dB-return loss bandwidths for these antenna elements were 1.9 and 3 GHz respectively, as confirmed both by simulations and measurements [13].

An increased return loss performance of these SP antennas was not sufficient to make the claim that they would be good candidates for developing an active TXA with increased operational bandwidth. In addition to high return loss, these antennas have to provide minium insertion losses when they form the power combiner structure. In order to obtain a more appropriate assessment, these antenna candidates were used to develop three configurations of the unit cell prototype of the planned TXA. Only one of the three investigated configurations of the unit cell provided minimum insertion loss and thus an optimal performance [13]. This configuration has been selected to develop 4×4 element passive and active TXAs. The design and development details of these two antenna systems are presented next.

3. The 4×4 array design

The configuration of an *X*-band power combiner configuration including the 4×4 cell TXA, which is investigated

here, is shown in Fig. 1. In this figure, the transmitting hard horn on the left illuminates the receiving (TXA-R) patch antennas. The signal is received by stacked patches, coupled through the slots in the ground plane, amplified in the feed layer before being reradiated by the transmitting (TXA-T) stacked patch antennas of edge-feed type. As seen in the figure, in each unit cell the TXA-R and TXA-T antennas are placed orthogonally back-to-back to each other. The cross polarized antennas are used purposely in order to increase isolation between input and output ports of the amplifiers. The amplified signal is combined by a pyramidal hard horn, which is orthogonally polarized to its input counterpart. The perspective view of the complete passive unit cell (in which the through connection is used in place of an amplifier) of TXA is shown

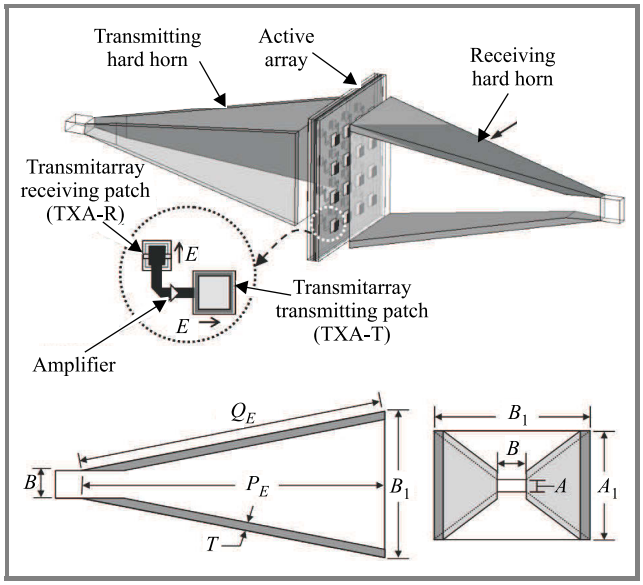


Fig. 1. A stacked patch (SP) transmitarray (TXA) spatial power combiner with transmitting and receiving hard horns. Parameters: $A = 10.16$ mm, $B = 22.86$ mm, $A_1 = 94$ mm, $B_1 = 126$ mm, $P_E = 240$ mm, $Q_E = 248.5$ mm, $T = 7.2$ mm.

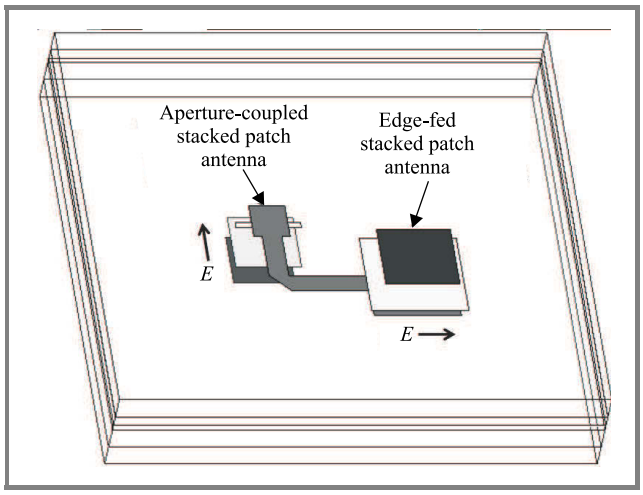


Fig. 2. Perspective view of the SP microstrip antenna unit when a through connection replaces an amplifier.

in Fig. 2. In turn, Fig. 3 reveals the schematic of the active unit cell including the biasing circuitry. The active devices chosen and implemented in the array are 50 Ω-pre-matched ERA-1 low power monolithic amplifier manufactured by Mini-Circuits®. The required bias condition of 3.6 V and 40 mA at the drain of the ERA-1 amplifier are easily accomplished with a bias voltage of 5 V and a 33 Ω biasing resistor. A simple radio frequency (RF) biasing

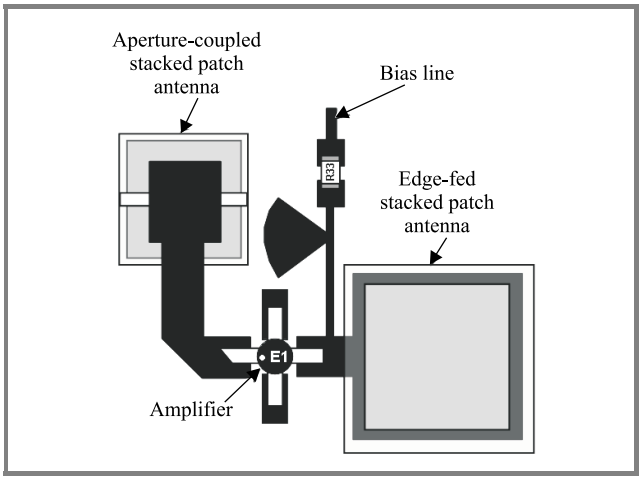


Fig. 3. Active unit cell of the SP TXA.

circuitry consisting of a high impedance line and a fan stub are designed and implemented. Normally, this amplifier is aimed for operation from DC to 8 GHz with gain not worse than 10 dB. The measurements performed on this amplifier revealed that it could be used beyond this band with an acceptable gain of 8.97 dB at 10 GHz.

In order to launch and receive the signal, two identical X-band pyramidal hard horns are designed and manufactured. The chosen aperture dimensions are 126 mm × 94 mm and the axial horn length is 240 mm. Dielectric slabs made using Rogers® RT/duroid® 5880 with $\varepsilon_r = 2.2$ are placed in the inner H-plane walls of the pyramidal horn to create hard surfaces. For operation at the centre frequency of 9.5 GHz, thickness of 7.2 mm was used, as obtained from the formula given in [14]. Parameters of the two hard horns are shown in Fig. 1.

Due to the fact that the computer resources currently available to the authors did not allow for simulating of the entire power combiner, further investigations were carried out using experimental means.

4. Results

First, two co-polarized hard horns spaced by the distance suitable for accommodating a passive or active transmitarray were measured to quantify the level of insertion loss. The average measured insertion loss was found to be 2.7 dB over a bandwidth of 2 GHz from 8.5 to 10.5 GHz. The 10 dB return loss was obtained across the entire X-band.

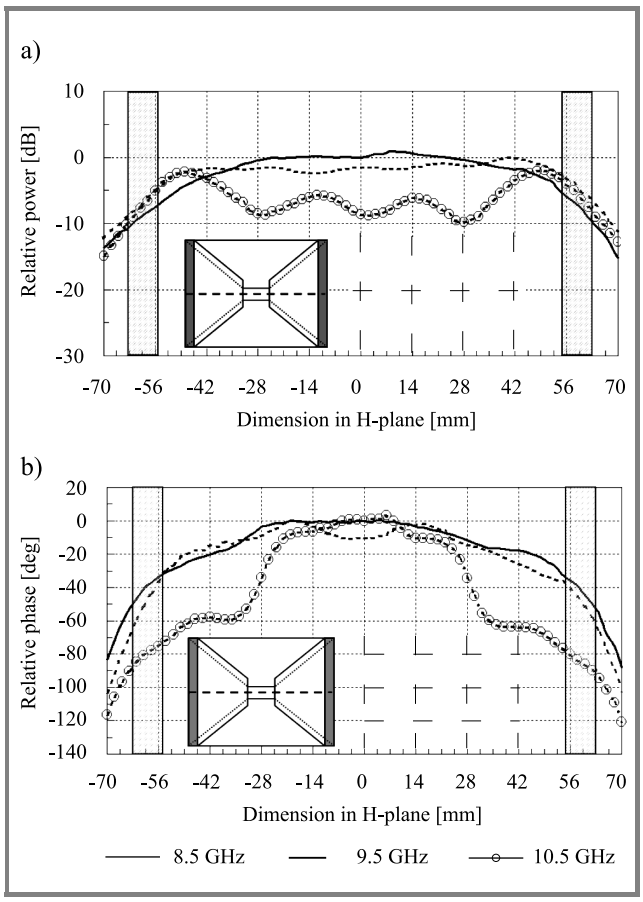


Fig. 4. (a) Magnitude and (b) phase distribution of hard horns along the H-plane cut through the centre of aperture at three selected frequencies. Shaded regions indicate the position and thickness of the dielectric slabs.

The two hard horns were also tested in terms of magnitude and phase uniformity across their apertures over the investigated frequency band. The measured field magnitude and phase distribution in H-plane cut for the horn aperture at three selected frequencies are shown in Fig. 4. From Fig. 4a, it is observed that the designed hard horn provides a uniform field magnitude distribution with less than ± 2 dB variation for more than 90% of the horn aperture at the design frequency of 9.5 GHz. However at 10.5 GHz, a ripple of 7 dB on average is formed over the aperture. In Fig. 4b, it is observed that an approximately uniform phase distribution is obtained at 8.5 and 9.5 GHz. At 10.5 GHz, a sharp change of phase occurs at about half way between the centre to both edges of the hard horn in H-plane cut. This indicates that the workable range for the hard horn, at which uniform magnitude and phase distribution are attained, is limited up to or slightly above the centre frequency at which the dielectric slabs are designed at.

Following the hard horns assessment, a full power combining structure including a passive or active TXA was measured. A 4×4 cell active SP TXA, based on the unit cell configuration of Fig. 3, is shown in Fig. 5. The array element spacing of $0.9\lambda_0$ or 28.42 mm at 9.5 GHz was chosen in order to accommodate the integrated active circuitry.

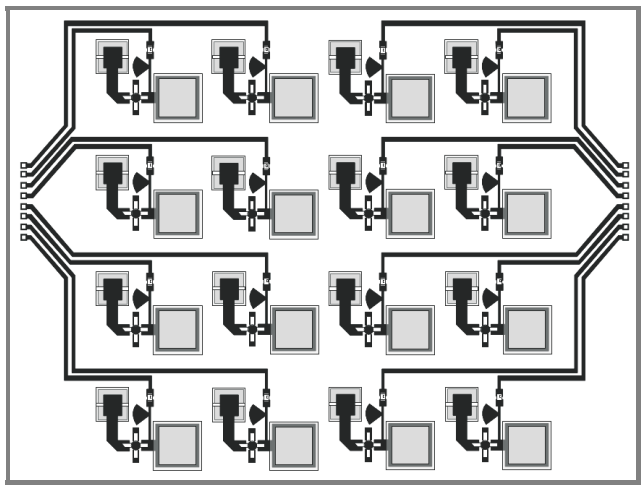


Fig. 5. A complete active 4×4 SP TXA.

In the first step, the structure including a passive 4×4 array was assessed. The array was placed in a horn-to-horn setup between two cross-polarized hard horns on a height adjustable mounting jig along a steel rail. A separation distance of 15 mm between the transmitting/receiving horn and the amplifier array was determined by manually adjusting the distance until good return loss level was achieved over at least 2 GHz bandwidth about the centre frequency of 9.5 GHz. The measured results of the 4×4 passive array are shown in Fig. 6. The minimum insertion loss

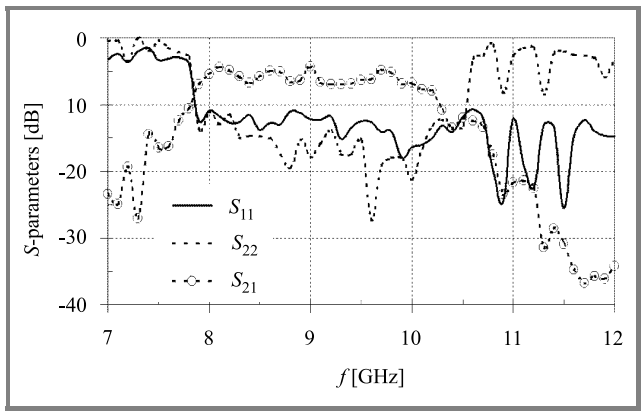


Fig. 6. Measured *S*-parameters of the passive 4×4 SP TXA.

is 4.3 dB at 9 GHz with a 3 dB-gain bandwidth of about 2.2 GHz and a maximum ripple of 2.7 dB across this band. This result indicates that the minimum insertion loss incurred by the passive array is 1.6 dB. However, this value varies with frequency, and the average value across the 3 dB-gain bandwidth is 3.74 dB. Using the same setup, measurements were performed on the active array and results are shown in Fig. 7. The maximum small signal gain is 3.46 dB at 8.7 GHz with a 3 dB-bandwidth of about 1.9 GHz. By taking into considerations of losses associated with the hard horns and passive array, the amplifier gain at 8.7 GHz is 8.53 dB, while the average value across this bandwidth is 7.9 dB. The 3 dB-bandwidth of the active array is reduced by 0.4 GHz, which can be attributed

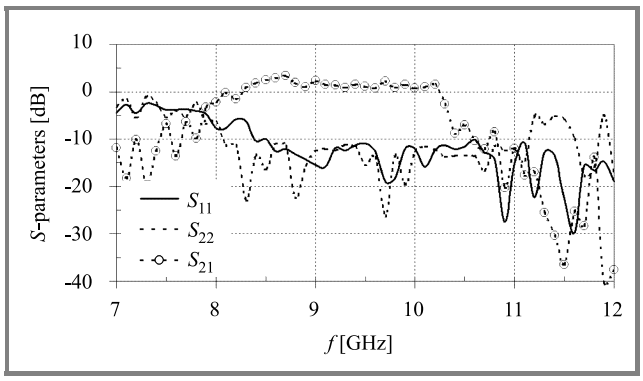


Fig. 7. Measured *S*-parameters of the active 4×4 SP TXA.

to the frequency shift of operation of antenna elements caused by the integration of the amplifier and biasing circuitry into the multi-layer passive TXA.

5. Discussion

The results presented in Figs. 6 and 7 show a reduced amplification gain. This gain reduction is because of insertion losses of the investigated power combining structure. The observed power loss is mainly due to leakage through the edge elements of the active array and is expected because the SPC investigated here is not a fully closed conducting structure. This power loss can be reduced by placing the active TXA into a waveguide between the launching and receiving horn antennas. Alternatively, it could be minimized by increasing the number of active array elements so there would be a smaller (in terms of percentage) group of elements responsible for leaking power outside the receiving horn.

The evaluation of performance of an amplifying power combiner is usually completed by making power compression measurements, in which the 1 dB-compression point is determined [2–9]. For a space level combiner, an alternative approach of assessing the same can be done through the near-field uniformity measurement of the transmitting side of an active aperture. The reason is that the uniform field distribution at the transmitting side of active aperture indicates that all of the elements of the active array are able to efficiently amplify both weak and large level signals. In particular, this condition facilitates simultaneous saturation of individual amplifiers under the large signal scenario. As a result, this condition enables the largest dynamic range of a space-level power combiner.

The measured near-field magnitude distribution across the E- and H-plane cuts at the output side of the 4×4 cell TXA (when the output hard horn is removed) at three selected frequencies is shown in Fig. 8, respectively. As seen in Fig. 8, there is a general degradation of uniformity across both the E- and H-plane of the array aperture at 10.5 GHz. Comparatively, stronger coupling is seen in H-plane, as this is due to the slot radiation of TXA-R, which is orthogonally polarized to TXA-T. Experimental observations of Fig. 8

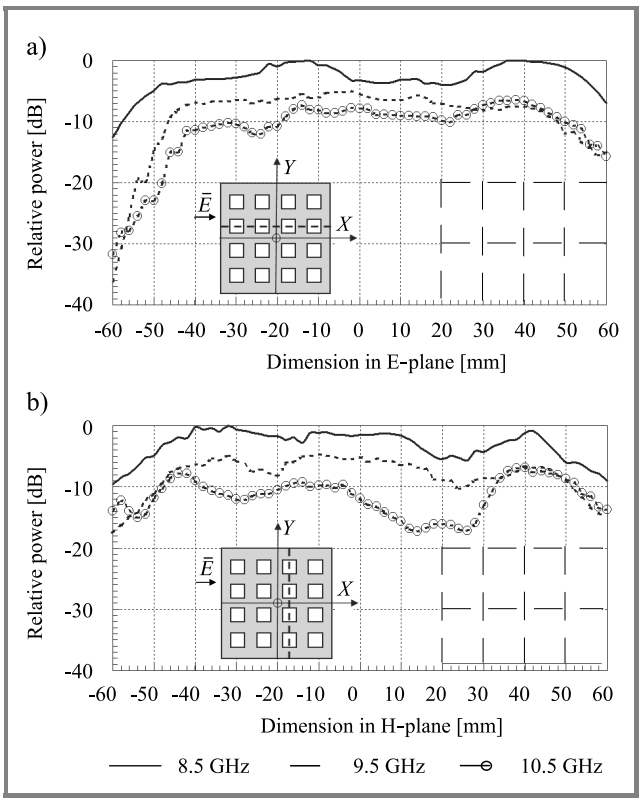


Fig. 8. Measured near-field magnitude distribution in (a) E-plane cut and (b) H-plane cut at the output side of the active 4×4 SP TXA illuminated by a hard horn at three selected frequencies.

follow that of Fig. 4 in which it is found that the hard horn supports uniform field aperture between 8.5 GHz and up to about 10 GHz. The results of Figs. 6 and 7 follow this trend, where it can be seen that the insertion loss performance begins to degrade beyond 10.3 GHz.

6. Conclusion

In this paper, stacked patch antenna elements connected to input and output ports of individual amplifiers have been proposed to increase the operational bandwidth of a space-level combiner employing a planar amplifying transmitarray. Two configurations of a unit cell prototype using three different SP antennas have been designed and investigated. Only the one showing a small insertion loss over an increased operational bandwidth has been used to form a 4 $\times$ 4 cell planar array for an *X*-band power combiner. Two hard horns for signal launching and combining have been designed, manufactured and tested to complete the design of the spatial power combiner. The structure has shown a minimum insertion loss of 4.3 dB at 9 GHz with 3 dB-gain bandwidth of 2.2 GHz when the passive array is placed between the two horns. The combiner with an active array has demonstrated a maximum small signal gain of 3.46 dB at 8.7 GHz, while taking into account all associated losses, with a 3 dB-bandwidth of about 1.9 GHz. This operational bandwidth could not be achieved using a transmitarray of edge-fed microstrip patches.

Acknowledgment

The authors acknowledge the financial support of the Australian Research Council. The first author also acknowledges the support of the IEEE MTT-S through his Graduate Fellowship.

References

[1] D. Staiman, M. E. Breese, and W. T. Patton, "New technique for combining solid-state sources", *IEEE J. Solid-State Circ.*, vol. SC-3, pp. 238–243, 1968.

[2] J. A. Navarro and K. Chang, *Integrated Active Antennas and Spatial Power Combining*. New York: Wiley-Interscience, 1996.

[3] R. A. York and Z. B. Popovic, *Active and Quasi-Optical Arrays for Solid-State Power Combining*. New York: Wiley-Interscience, 1997.

[4] S. Ortiz, T. Ivanov, and A. Mortazawi, "A CPW-fed microstrip patch quasi-optical amplifier array", *IEEE Trans. Microw. Theory Techn.*, vol. 48, no. 2, pp. 276–280, 2000.

[5] H. J. Song and M. E. Bialkowski, "Transmit array of transistor amplifiers illuminated by a patch array in the reactive near-field region", *IEEE Trans. Microw. Theory Techn.*, vol. 49, no. 3, pp. 470–475, 2001.

[6] S. Ortiz, T. Ivanov, and A. Mortazawi, "A transmit-receive spatial amplifier array", in *1997 IEEE MTT-S Int. Microw. Symp. Dig.*, Denver, USA, 1997, vol. 2, pp. 679–682.

[7] T. Ivanov *et al.*, "A passive double-layer microstrip array for the construction of millimeter-wave spatial power-combining amplifiers", *IEEE Microw. Guided Wave Lett.*, vol. 7, no. 11, pp. 365–367, 1997.

[8] A. B. Yakovlev, S. Ortiz, M. Ozkar, A. Mortazawi, and M. B. Steer, "A waveguide-based aperture-coupled patch amplifier array, full-wave system analysis and experimental validation", *IEEE Trans. Microw. Theory Techn.*, vol. 48, no. 12, pp. 2692–2699, 2000.

[9] S. Ortiz *et al.*, "A high-power ka-band quasi-optical amplifier array", *IEEE Trans. Microw. Theory Techn*., vol. 50, no. 2, pp. 487–494, 2002.

[10] N. S. Cheng, T. P. Dao, M. G. Case, D. B. Rensch, and R. A. York, "A 120-W *X*-band spatially combined solid-state amplifier", *IEEE Trans. Microw. Theory Techn.*, vol. 47, no. 12, pp. 2557–2561, 1999.

[11] M. E. Bialkowski, "Spatial power combiners using active planar arrays", in *Novel Technologies for Microwave and Millimeter-wave Applications*, Ed. J.-F. Kiang. Kluwer, 2004, ch. 17, pp. 369–391.

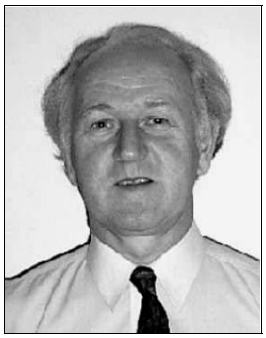
[12] S. D. Targonski, R. B. Waterhouse, and D. M. Pozar, "Design of wide-band aperture-stacked patch microstrip antennas", *IEEE Trans. Anten. Propagat*., vol. 46, no. 9, pp. 1245–1251, 1998.

[13] F.-C. E. Tsai and M. E. Bialkowski, "Investigations into the design of a spatial power combiner employing a planar transmitarray of stacked patch antennas", in *Proc. MIKON 2004*, Warsaw, Poland, 2004, pp. 509–512.

[14] P.-S. Kildal, "Definition of artificially soft and hard surfaces for electromagnetic waves", *Electron. Lett.*, no. 24, pp. 168–170, 1988.



Feng-Chi E. Tsai received the B.E. degree (2000) and the Ph.D. degree (2004) in electrical engineering from the University of Queensland. Between 2001 and 2004, he was a Research Assistant in School of Information Technology and Electrical Engineering of the University of Queensland working in the field of microstrip patch array antennas, RF/microwave circuits for wireless communications, and spatial power combining techniques. He was a recipient of the Best Student Presentation prize at the 7th Australian Symposium on Antennas (2001), the IEEE Microwave Theory and Techniques Society Graduate Fellowship (2003), and the 3rd Student Paper prize awarded by the European Microwave Association (EuMA) at the 15th MIKON Conference, Poland (2004).
e-mail: tsai@itee.uq.edu.au
School of ITEE
University of Queensland
St Lucia, Brisbane
QLD 4072, Australia



Marek E. Bialkowski received the M.Eng.Sc. degree (1974) in applied mathematics and the Ph.D. degree (1979) in electrical engineering from the Warsaw University of Technology, Poland, and the D.Sc. degree (2000) in computer science and electrical engineering from the University of Queensland, Australia. He held teaching and research appointments at universities in Poland, Ireland, Australia, UK, Canada, Singapore, Hong Kong, and Switzerland. At present he is a Chair Professor in the School of Information Technology and Electrical Engineering at the University of Queensland. His research concerns the field of modelling, design, and testing of microwave guiding and radiating structures. His contributions earned him an IEEE Fellow award in 2002.
e-mail: meb@itee.uq.edu.au
School of ITEE
University of Queensland
St Lucia, Brisbane
QLD 4072, Australia

Paper

Application of optical dispersion techniques in phased array antenna beam steering

Marcin Muszkowski and Edward Sędek

Abstract—The paper presents an opto-electronic system for antenna beam control and results of model system measurements.

Keywords—phased arrays antennas, fiber optic, dispersion, laser.

1. Introduction

Active phased arrays antennas [1] play an important role in modern radar systems. This kind of antenna techniques is a flexible way to apply electronic beam scanning in wide angle range without the need for mechanical rotation of the antenna and easy spatial characteristics beam shaping, achieved by independent control of transmitting elements [2].

2. Electronic scanning of antennas beam

Phased array active antennas consist of independent microwave transmitting and receiving elements. Separate control signals are being supplied to them by using independent variable phase shifters or delay lines. The desired direction characteristic of an antenna is achieved by proper power supply and time delay distribution of control microwave signals. Phased array antenna beam steering [3] is based on supplying antenna radiating elements by microwave signals with gradually increasing phases. In the case of one-dimensional active antenna, the phase difference between antenna array consecutive elements required for shifting antenna's beam off an antenna axis by θ angle, can be presented as follows:

$$\alpha = 2\pi \frac{d}{\lambda} \cos\theta \,, \tag{1}$$

where: λ – microwave signal wavelength, d – distance between radiating elements.
Using formula $\lambda = \mathrm{c}/f$, where c is light speed in vacuum, and f – microwave signal frequency, we obtain:

$$\alpha = 2\pi f \frac{d}{\mathrm{c}} \cos\theta \,. \tag{2}$$

The above equation indicates that phase difference of microwave signals depend on microwave signal frequency. It means that varying frequencies are positioned in different directions. This disadvantage limits antenna operation to monochromatic signals, excluding wide band systems implementation.
Substituting in Eq. (2) by formula $\alpha = 2\pi ft$, where t is time while the wave changes phase by α, and transforming this equation, we achieve a simple dependence for delay time of microwave signal distributed to the antenna to generate beam under angle θ:

$$t = \frac{d}{\mathrm{c}} \cos\theta \,. \tag{3}$$

The above equation shows that the time delay of a microwave signal between the consecutive antenna elements, as opposite to phase shift, does not depend on frequency implicating a possibility of wide band operation.

3. Optoelectronic antenna steering system

The concept of developed steering system applies material dispersion phenomenon in single-mode optical fibres to obtain tuned time delay of microwave signals [4, 5] and uses optic fibre sections arranged as binary tree. The scheme of a control system for 16-element linear antenna is presented in Fig. 1. Tuned wavelength laser in range 1520 – 1600 nm and 10 mW optical output power has been used as an optic signal source. The optic signal is routed to electro-optic modulator. The applied modulator operates in a third optic window, allowing for 10 GHz optical signal modulation. A specialised microwave amplifier has been applied as a modulator control unit.
Microwave input signal, following relevant amplification in a driver, is routed to the modulator electric input. Thus, an optic signal on the modulator output is amplitude modulated with the envelope compatible to the control microwave signal from RF generator. Next, the modulated optic signal is distributed to a binary tree introducing the relevant microwave signal delays on individual outputs of the system. Delayed signals are attenuated by fibre optic attenuators to obtain required power distribution. Next, they are routed to the inputs of 16 optical receivers, performing optic to electric signal conversion and finally distributed to the microwave amplifiers, thus additional amplifying

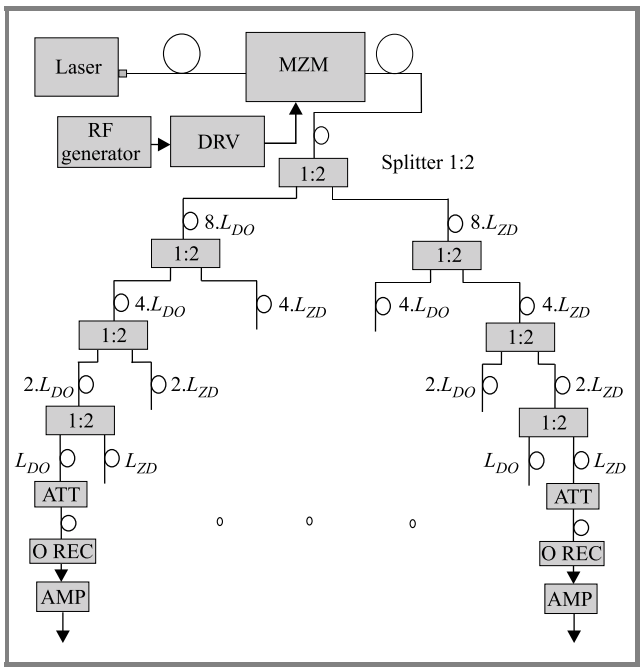


Fig. 1. Antenna control system scheme.

of 22 dB is performed. Antenna beam control system requires selection of high dispersion fibre optic length L_D and zero dispersion fibre optic length L_{ZD}, according to operation laser wavelength range, to obtain the desired antenna beam scanning range.

4. Control system measurements

The system maximum amplification is 25 dB for laser output power equal 10 dB. All optic link bandwidth reaches 8 GHz. Measurement results of microwave signal

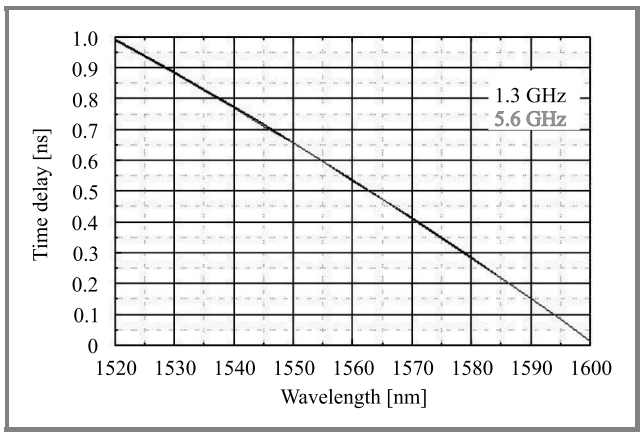


Fig. 2. Microwave signals time delay change versus laser wavelength.

time delay changes of the control system output, for the microwave signals frequencies 1.3 GHz and 5.6 GHz are presented in Fig. 2.

Ideal compatibility between those two diagrams conducted for two varying frequencies can be observed – black curve exactly covers the grey one. This indicates no frequency dependence of signals time delay. The obtained results correspond to the theory very well. In both cases, tuning the laser wavelength by 80 nm brings microwave signal time delay change of about 970 ps. The propagation time change resolution of 1.2 ps can be achieved for the applied fibre length equal 790 m.

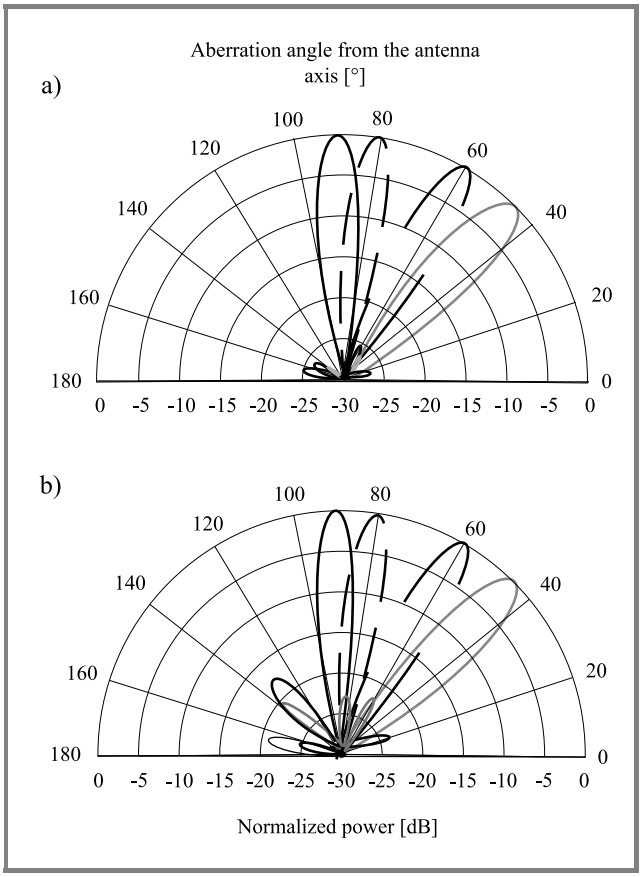


Fig. 3. Elevation characteristics of 16 elements antenna row: (a) calculated in theory; (b) calculations based on measurements.

Detail measurements of the developed system are based on measurements of output signals power distribution and microwave signals delay, between a modulating signal and 16 outputs signals of the control system. The measurements have been done on microwave network analyzer HP8720B. Power and phase of microwave signal have been measured. The phase was converted into time delay for signal frequency equal 5 GHz. The antenna elevation characteristics have been calculated on the base of obtained results. The characteristics have been developed for 4 optic signal wavelengths. Antenna beam scanning in the range of $0°-45°$, has been achieved. Elevation characteristics of an antenna, calculated theoretically (a) and based of measurements (b) for the distribution of output power like $\cos^2 x + 0.4$ are presented in Fig. 3. Presented radiation characteristics of the 16 elements antenna row, performed

for non-uniform signals power distribution at the control system outputs prove considerable compatibility to theoretical simulations.
The developed system ensures an opportunity of the beam propagation direction control with an excellent accuracy 0.1°. This allows to achieve an ideal agreement of the antenna beam propagation angle according to desired direction. For 16 antenna elements the beam width reaches 6.3° for 0° propagation angle and 9° for 45° propagation angle. The side lobes level is –25 dB related to the main lobe in the simulation, while real characteristics side lobes level is about –17 dB. This difference can be reduced by applying higher precision optic attenuators.

5. Conclusions

The paper describes a concept of the optoelectronic components application for the construction of the system targeted at steering 16 element antenna row. On the base of the obtained measurement results excellent optic parameters have been achieved: low optic losses at the level of 15.5 dB, light source power high stability allowing operation at the power level of +8 dB for the wide wavelength tuning range, negligible dependence between the fibre optic links attenuation and laser wavelength. Electric parameters: amplification of single link over 25 dB and 5 dB of the whole control system, dynamic range over 70 dB, 8 GHz signal bandwidth have been achieved. Microwave signal delay resolution measurement, accompanied by changing the optical carrier wavelength, generated by the semiconductor laser, is better than 1.2 ps. Thus, very high resolution and an excellent accuracy of the antenna beam positioning have been achieved.

References

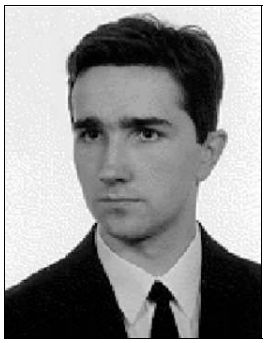
[1] R. J. Mailloux, *Phased Array Antenna Handbook*. Boston, London: Artech House, 1994.

[2] H. Zmuda and E. N. Toughlian, *Photonic Aspect of Modern Radar.* Boston, London: Artech House, 1994.

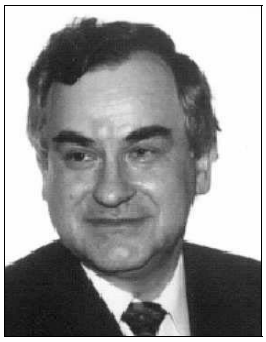
[3] A. J. Seeds, "Application of opto-electronic techniques in phased array antenna beamforming", in *Microw. Phot., Tech. Dig., MWP*, Duisburg/Essen, Germany, 1997.

[4] R. Soref, "Optical dispersion technique for time-delay beam steering", *Appl. Opt.*, vol. 31, no. 36, p. 7395–7397, 1992.

[5] M. Y. Frankel and R. D. Esman, "True time-delay fibre-optic control of an ultra wide band array transmitter/receiver with multibeam capability", *IEEE Trans. Microw. Theory Techn.*, vol. 43, pp. 2387–2394, 1995.



Marcin Muszkowski was born in Ryki, Poland, in 1968. He received the M.Sc. degree in optoelectronic engineering from Warsaw University of Technology on Technical Physic and Apply Math Faculty, Warsaw, Poland, in 1993, and Ph.D. degree in microwave engineering form Telecommunications Research Institute, Warsaw, Poland, in 2003. His research interests are optoelectronic applications in phased array antennas, development of fibre optic test equipment and dedicated digital fibre optic links.
e-mail: muszmarc@pit.edu.pl
Telecommunications Research Institute
Poligonowa st 30
04-051 Warsaw, Poland



Edward Sędek received the M.Sc. and Ph.D. degrees in electronic engineering from the Warsaw University of Technology, Warsaw, Poland, in 1968 and 1980, respectively. In 1968, he joined the Telecommunications Research Institute, Warsaw, and become an Assistant Professor in 1980. His primary research interests are microwave ferrite devices, CAD method of waveguide, stripline, microstrip circulators and isolators and ferrite phase shifters. His other research interests include planar antenna techniques and optoelectronics method for scanning radar beam. In recognition of his contributions in the area of design, modeling and testing of microwave ferrite devices he received the Doctor of engineering degree (higher doctorate) from Warsaw University of Technology in 1990. In March 1991 he was appointed scientific Director for Telecommunications Research Institute. In the years 1994–1998 Dr. Sędek was Chapter Chairman of Poland Section of MTT. He is a organizing chair of International Conference on Microwaves, Radar and Wireless Communications MIKON in Poland and vice chairman of MIKON Technical Program Committee. The MIKON is the biggest regional microwave and radar conference in the East Europe. He is a member of Polish Academy of Sciences (PAN) Electronic and Telecommunication Committee and member of Microwave Section of this Committee.
e-mail: sedek@pit.edu.pl
Telecommunications Research Institute
Poligonowa st 30
04-051 Warsaw, Poland

Paper

A lightweight planar antenna element with optimized feed for use onboard spacecraft

Krzysztof Wincza and Paweł Kabacik

Abstract—This paper is a report on low gain antennas (LGAs) manufactured with bonded lightweight materials. These antennas can sustain large temperature variations and are capable of functioning in modern miniature spacecraft, mainly in the telemetry, command and ranging (TC&R) links. When made of cheaper materials, the proposed circularly polarized antenna can be widely used in the base stations of short-range wireless systems. The recommended operating frequencies are between 1 and 8 GHz. One major technical consideration is obtaining the required high quality of circular polarization with as low space demands as possible. A lightweight 90° polarizer, printed on a dielectric membrane and operating over a broad bandwidth, is proposed for the antenna feed. Owing to the bandwidth advantage of the polarizer and the use of carefully designed aperture coupled feed, the electrical characteristics maintain good properties over a wide frequency range (15%).

Keywords— microstrip antennas, spaceborne antennas, circularly polarized antennas.

1. Introduction

The presented lightweight patch antenna is intended to operate in two main applications: the telemetry, command and ranging (TC&R) links of small spacecraft and radio interfaces of short range wireless systems. Regardless of the spacecraft, an ideal TC&R antenna should feature radiation properties which do not give rise to more than a tolerable risk of problems with TC&R signals, irrespective of problems with the orbital position of the given minisatellite [1]. Antennas with a deployment mechanism are regarded as too troublesome in minisatellites, as they add an unacceptable complexity. As minisatellites are characterized by low volume and dense packing of components, TC&R low gain antennas (LGAs) should be planar antennas suitable for mounting on a wall. They should be manufactured from various derivatives of microstrip technology, and be preferably mounted directly onto the walls of minisatellites [2]. In wireless systems, among the several properties key for market success are broadband operation, low weight and polarization properties capable of improving the link budget.

2. Lightweight broadband patch elements

The patch shape and the feed are responsible for broadband operation. The beamwidth is similar, at least in the case of the most popular patch shapes. However, in order to achieve broadband impedance match and high quality circular polarization, patch shape requires special attention. It is very important that the patch should retain the symmetry which is one of the primary conditions for achieving a good axial ratio in circularly polarized antennas. Patch feed is a key technical issue [3]. Generally, the use of feed via through-slot coupled lines is unavoidable, and fortunately, such a feed ensures a low profile for the radiating part of the LGA. When optimizing aperture through-slot coupling, the use of differently shaped slots may result in high isolation, which is required to achieve excellent circular polarization. An important advantage is that aperture-coupled antennas offer a great flexibility in terms of modeling their electrical parameters.

The various parts of the lower S-band are the primary target for the described antenna design. To provide the necessary bandwidth for all operational conditions in the uplink or in the downlink at the S-band, the height of the patch should approach 10 mm when a substrate with a dielectric constant close to one is used. A conceptual sketch of an LGA displaying the desired merits is depicted in Fig. 1. The antenna is fed with slot-coupled microstrip lines. We found that the stripline feed is possible to match to 50 Ω with the extra slots in the enclosing ground of the stripline.

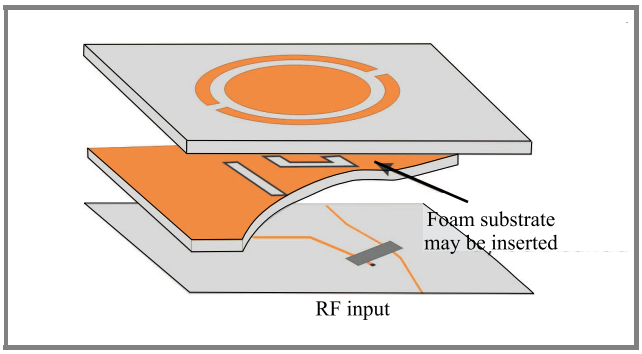


Fig. 1. The circular patch investigated in the course of our studies. It features a high quality of circular polarization as field is favorably modified by parasitic semicircular strips.

An advantage of lightweight LGAs is that their parts combine electromagnetic and structural functions. Tiny elements generate weak loads which can be borne by a simple structure. Two basic structural designs for the patch were studied. In one concept, the patch substrate was a honeycomb composite, and in the other, it was foam [4].

The honeycomb composite has a dielectric constant close to 1.1, while the foam has a broader range of dielectric constant values, usually up to 1.8 (Rohacell foam has $\varepsilon_r \approx 1.05-1.1$). In our view, honeycomb composite has become of great value in larger antennas which should have high structural strength. In honeycomb panels, the electrical properties of the bonding layers become difficult to control after curing. That is the main reason why in our opinion, the honeycomb structure is far less suitable for small microstrip LGAs than foam. It is worth mentioning that our investigation into the thermal behavior of patch antennas showed that some types of foam display excellent thermal properties. One such type of foam is quartz fiber composite, which shows a high resistance to temperature variation [5]. The bonding system applied is essential for achieving adequate mechanical strength and good electrical properties.

3. Broadband generation of circular polarization in patch elements

We focused on two separated slots responsible for orthogonal modes in the LGA feeding (Fig. 2). For the needs of circular polarization generation, the two slots must be fed with in-quadrature signals of equal power. Various pairs of

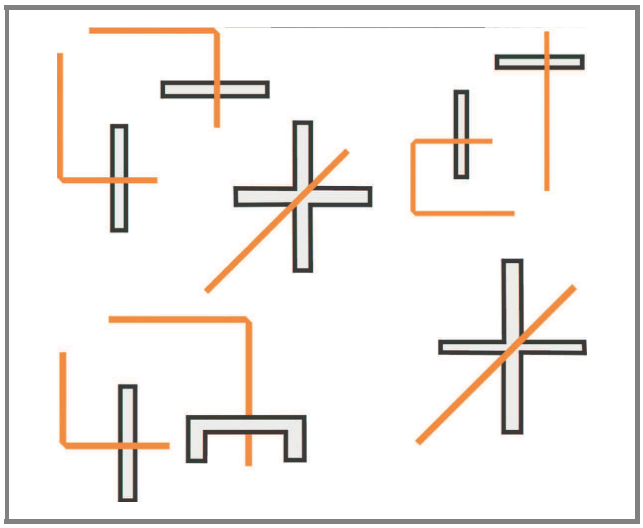


Fig. 2. A variety of slot shapes enabling the generation of circular polarization (a line shows the arrangement of the microstrip feed line).

slot shapes were investigated: rectangular, and C-, X- and H-shaped. Another considered shape of coupling aperture was a single cross slot. A cross slot requires a balanced feed of two orthogonal slot branches [6]. The application of cross slots has little demand on space [7]. However, the width of the feed lines varies continuously over the coupling section. It is important that such a method results in good radiation properties when patches are clustered into modules, as the concept fails to produce good circular polarization with a single element.

As shown in the course of our studies, the optimum energy transmission is when the rectangular slots extrude outside the patch outline (an optimum displacement is of 12% of a slot length). The widths of slots ensuring efficient excitation of the patch account for roughly 10% of the patch resonant length [8]. A slight displacement of the transmission line off the slot center gives another noticeable improvement. In order to keep the pair of slots entirely under the patch, other shapes must be used (e.g., C-shaped slot).

We found that two rectangular slots feature low isolation between ports and that this shortcoming is difficult to overcome unless the displacement between the ends of the feed lines resembles a "T". Further improvement can be obtained via a combination of a rectangular and a C-type slot [9]. In our simulations, the improvement in isolation was by 12 dB. In order to have a good line coupling to the patch, the width of the C-slot must be relatively large; however, this complicates its application with thick substrates.

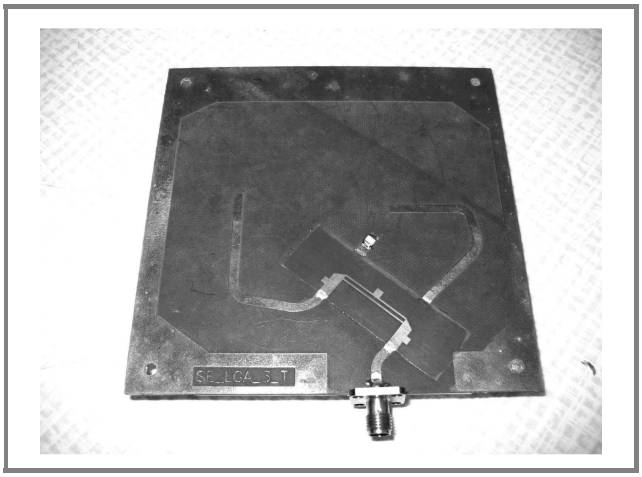


Fig. 3. A three-strip line directional coupler made on a thin dielectric membrane (125 μm) bonded to a 31 mil thick microwave laminate.

A minute area occupied by the polarizer is a prerequisite of LGA miniaturization. In our LGA, we used a three-strip coupler (Fig. 3). The coupler was thoroughly investigated by Sachse and Sawicki [10]. The compensation of phase velocity is achieved with conductive bridges in the middle of the coupling structure; thus, no troublesome superlayer dielectric bars are required. Usually, the core part of a coupling circuit is made on a 1 to 5 mil-thick laminate, and this circuit is bonded to a typical microwave laminate. By consequence, there is virtually no extra volume required for such a polarizer, apart from the unavoidable spacing around the coupler diminishing undesired external couplings. Such thin dielectric laminates are flexible. Polyimide films are good for such applications. A three-strip coupler is a quarter wavelength long, and has a total width which is approximately that of two 50 Ω microstrip lines. Thus,

the three-strip directional coupler has 8-times smaller area requirements than a branch or Gysel coupler for the same center frequency. A further decrease in coupler dimensions requires the application of non-uniform coupling circuits. Roughly, the total volume of the RF part of the described LGAs operating at 2 GHz ranges between 100 cm^3 and 200 cm^3 (Fig. 4).

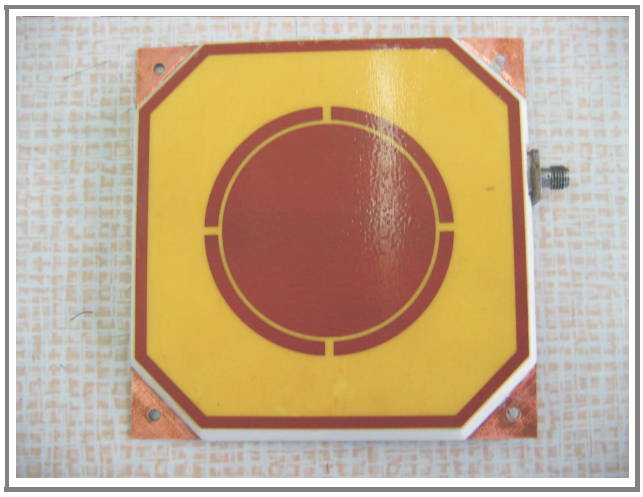


Fig. 4. A model of a lightweight broadband antenna developed in the course of our research.

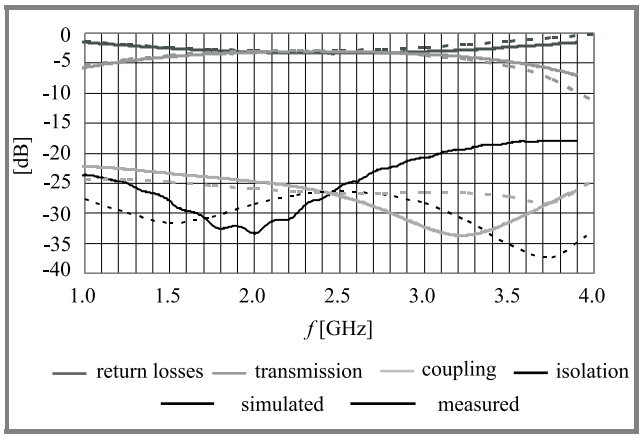


Fig. 5. The calculated and measured characteristics of the three-strip directional coupler shown in Fig. 3.

The electrical properties of the coupler used in one of our LGAs are presented in Fig. 5. The coupler features extremely broadband operation, a typical property of this coupler type. Losses in the antenna feed due to such a coupler are generally not greater than 0.25 dB. This loss can be difficult to obtain at times, particularly when membrane properties are poorly determined. The coupler is capable of handling RF powers much above those which are generated by the few Watt power amplifiers (typically used) onboard minisatellites. The measured impedance characteristics for one of LGA prototypes is plotted in Fig. 6. Our studies showed that to combine a good impedance match with a high quality circular polarization, it is necessary to

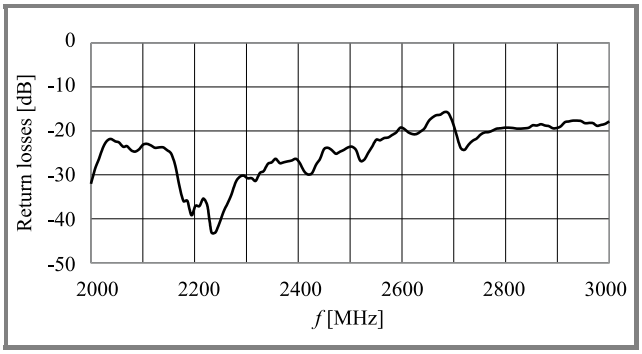


Fig. 6. The measured return loss for the presented circularly polarized antennas. The calculated and measured impedances match each other.

maintain a good balance of the directional coupler and its coupling to the slots. Among the most attractive advantages of the described antennas is their high gain value (8 to 9 dB on average) and good axial ratio. In all the considered antenna designs, the axial ratio was not greater than 1.5 dB over a wide frequency range (broadside direction) and remains good in a wide angular range.

4. Conclusions

Lightweight, circularly polarized antennas manufactured in microstrip technology are attractive for use in small spacecraft and in base stations of short-range wireless systems. A major technical challenge lies in generating circularly polarized waves with a minute feed circuit. Standard approaches are too cumbersome and they do not ensure broadband operation. Some types of directional couplers printed on a piece of thin dielectric, such as a three-strip design, show good electrical properties over a wide band and are recommended for integration into the feed of the circularly polarized LGA. Owing to the advantages of such a polarizer, it is possible to develop a broadband antenna in a lightweight technology. The optimization of the electrical properties requires careful analysis of the aperture through slot coupled feed.

References

[1] M. Rybakowski and K. Wincza, "Integrated S-band antenna for the ESEO minisatellite". M.Sc. thesis, Wrocław: Wrocław University of Technology, 2003.

[2] K. Wincza, M. Osys, L. Dudziński, and P. Kabacik, "Lightweight low gain microstrip antennas for use in minisatellites", in *XV Int. Conf. Microw., Radar Wirel. Commun. MIKON 2004*, Warsaw, Poland, 2004.

[3] G. Jaworski and V. Krozer, "A design of feeding network for a dual-linear polarization, stacked, probe-fed microstrip patch antenna array", in *XV Int. Conf. Microw., Radar Wirel. Commun. MIKON 2004*, Warsaw, Poland, 2004.

[4] P. Kabacik, K. Sachse, A. Sawicki, G. Jaworski, and M. Bialkowski, "Airborne radar antenna modules using lightweight temperature-resistant materials", in *IEEE Int. Conf. Phas. Array Syst. Tech.*, Dana Point, USA, 2000.

[5] P. Kabacik and M. Bialkowski, "The temperature dependence of substrate parameters and their effect on microstrip antenna performance", *IEEE Trans. Anten. Propagat.*, vol. 47, no. 6, pp. 1042–1049, 1999.

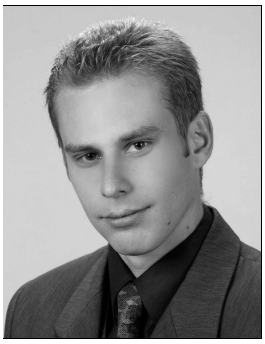
[6] S. D. Targoński and D. M. Pozar, "Design of wideband circulalry polarzied microstrip antennas", *IEEE Trans. Anten. Propagat.*, vol. 41, no. 2, pp. 214–220, 1993.

[7] D. Löffler, W. Wiesbeck, M. Eube, K.-B. Schad, and E. Ohnmacht, "Low cost conformal phased array antenna using high integrated SiGe-technology", in *IEEE APS Int. Symp.*, Boston, USA, 2001, pp. 334–337.

[8] P. Kabacik, M. Rybakowski, K. Wincza, and M. Bialkowski, "A circularly polarized antenna element for highly integrated array antennas", in *INICA 2003 – Int. ITG-Conf. Anten.*, Berlin, Germany, 2003.

[9] S. K. Padhi, N. C. Karmakar, C. L. Law, and S. Aditya, Sr., "A dual polarized aperture coupled circular patch antenna using a C-shaped coupling slot", *IEEE Trans. Anten. Propagat.*, vol. 51, no. 12, pp. 3295–3298, 2003.

[10] K. Sachse and A. Sawicki, "Quasi-ideal multilayer two- and three-strip directional couplers for monolthic and hybrid MIC", *IEEE Trans. MTT* (special issue on multilayer circuits), vol. 47, no. 9, pp. 1873–1882, 1999.



Krzysztof Wincza was born in Wałbrzych, Poland, in 1979. He received the M.Sc. degree in electrical engineering, specialization in telecommunication from the Department of Electrical and Computer Engineering, Wrocław University of Technology, Poland, in 2003. Currently he carried on studies towards the Ph.D. degree at Wrocław University of Technology. His scientific interests include lightweight and highly integrated antenna arrays, conformal antennas, spaceborne antennas, reconfigurable arrays and satellite communication. The Technical Committee of the 10th National Symposium of Radio Sciences URSI (2002) awarded him the Youth Award of URSI Symposium for a paper "Optimisation communication links of the ESEO minisatellite". He is a recipient of the 3rd Award in the competition organized by the Polish Chapter of the IEEE for the Best M.Sc. Thesis in the field of microwave, antenna and radiolocation technique and technology. He has worked as a system engineer in the Student Space Exploration and Technology Initiative project since 2001. The project is executed under the supervision of the European Space Agency and its aim is to develop a series of minisatellites and a lunar rover.

e-mail: Krzysztof.Wincza@pwr.wroc.pl
Institute of Telecommunications and Acoustics
Wrocław University of Technology
Wybrzeże Wyspiańskiego st 27
0-370 Wrocław, Poland



Paweł Kabacik was born in Wrocław, Poland, on 1 January 1963. He received the M.Sc. degree in telecommunications (highest honors) from Wrocław University of Technology in 1986. In 1996 he received the Ph.D. in electrical engineering (award). In January 1987, he joined the Institute of Telecommunications and Acoustics, Wrocław University of Technology. He was a visiting scholar to the Technical University of Denmark (1991/1992) and to the University of Queensland (1997 and 2001). He chaired the Mulitband Antennas and Conformal Array Mini-Team acting within the COST 260 Project and he chairs one of four research tasks in the current COST 284 Project. He is an expert of European Commission. His research interests include highly integrated antenna arrays, conformal antennas, terminal antennas, phased arrays, advanced antenna measurements and communication subsystems of small spacecraft. He was a Principal Investigator to several contracts funded by the National Research Council, Poland, and by industry. He is a member of Technical Committees at several international conferences. He received several recognitions for his research work, of which the most valuable is the *2000 Harold A. Wheeler Applications Prize Paper Award Honorable Mention* of the IEEE. In 1993 he received the Award for Young Scientists at the 7th National URSI Symposium, Poland. He was listed in five editions of *Marquis's Who's Who in Science and Engineering.*

e-mail: Pawel.Kabacik@pwr.wroc.pl
Institute of Telecommunications and Acoustics
Wrocław University of Technology
Wybrzeże Wyspiańskiego st 27
0-370 Wrocław, Poland

Paper

Applying the radiated emission to the specific emitter identification

Janusz Dudczyk, Marian Wnuk, and Jan Matuszewski

Abstract—During the last years we have observed fast development of the electronic devices and electronic warfare systems (EW). One of the most principal functions of the ESM/ELINT system is gathering basic information from the entire electromagnetic spectrum and its analysis. Simultaneously, utilization of some tools of artificial intelligence (AI) during the process of emitter identification is very important too. A significant role is played by measurement and signature intelligence (MASINT) based on non-intentional emission (calls-radiated emission). This emission is a source of knowledge about an analysed emitter due to its incidental "chemical", "spectral" traces and non-communication emitter's characteristics. The process of specific emitter identification (SEI) based on extraction of distinctive radiated emission features is presented by the authors. Specially important is utilization of a database (DB) in the process of identifying a detectable radar emission.

Keywords— radiated emission, distance and homology function, measurement and signature intelligence, specific emitter identification.

1. Introduction

A radiated emission is presented by accessible sources of information in the context of electromagnetic compatibility (EMC). The condition which prevails when telecommunications (communication-electronic) equipment is collectively performing its individually designed functions in a common electromagnetic environment without causing or suffering unacceptable degradation due to electromagnetic interference to or from other equipments/systems in the same environment is defined and required by electromagnetic compatibility [8, 11]. A radiated emission is defined as a non-intentional (undesired) energy in the form of electromagnetic waves, which is propagated through into environment. Such an emission is called "radiated emission/interference" if it is parasitic radiation. It is an effect of electronic device working.

The evaluation of parasitic radiation level, generated by radio-electronic devices is realized by:

- qualification of mechanisms of radiated emission penetration into surrounding environment;
- measurement of radiated emission;
- measurement of conducted emission;
- creation of EMC strategy and international cooperation.

The present electronic intelligence system acquires basic information from different spheres of activities, e.g., signal intelligence (SIGINT), imagery intelligence (IMINT), human intelligence (HUMINT) and MASINT [1, 5, 6, 12]. Conventional electronic warfare support measures (ESM) systems measure some basic parameters of incoming radar signals. These basic (typical) parameters are as follows: radio frequency (RF), time of arrival (ToA), pulse width (PW), angle of arrival (AoA), amplitude (A) or pulse repetition interval (PRI). The characteristic of present battle-field electromagnetic environment, the process of acquisition and transformation data shows, that measured basic parameters are not enough during the process of source identification. Utilization of some specific properties of electronic devices functioning, e.g., radiated emission, can cause heightening probability of a correct identification.

2. Some methods of radiated emission analysis

The analysis of radiated emission propagated by electronic devices is based on checking, in a given frequency band, its radiation characteristic and qualification of components, i.e., electric and magnetical, of electromagnetic field or alternatively on determination of its radiated power on direction of maximum radiation [11].

Such measurement of radiated emission has been standardized (normalised) for many years and may be realized using open area test site (OATS) [2, 7, 11]. An OATS consists of the following elements: a ground plane fitted with integral turntable, a power connection, a scanning antenna dielectric mast with polarity switching and remote control (Fig. 1).

An open area test site exploitation (utilization) is determined by high costs of building and maintenance of OATS

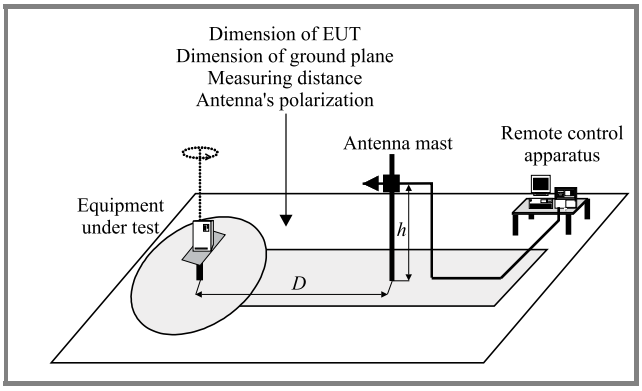


Fig. 1. Testing of radiated emission based on OATS.

and a permanent atmospheric influence. In this case, the measurement of radiated emission is realized using anechoic chambers, e.g., full and semi-anechoic chambers. Generally EMC chambers are used to test equipment for electromagnetic compatibility and susceptibility criteria. An anechoic chamber is a resonant cavity and by loading a chamber with specific loss absorber material and specially protective screen, a cavity and its associated resonances can be controlled. Thanks to using, for example, a hybrid ferrite-foam absorber, space of well-known and controlled conditions of electromagnetic waves propagation is obtained.

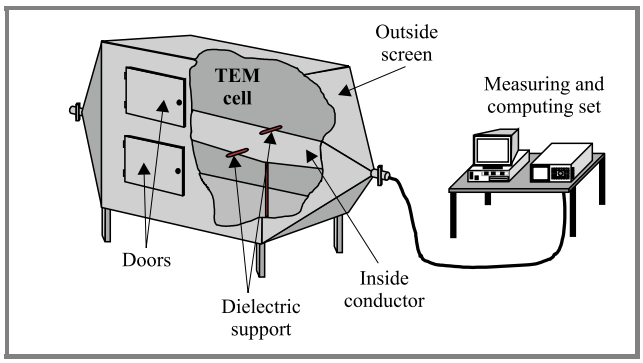


Fig. 2. Testing of radiated emission based on TEM cell.

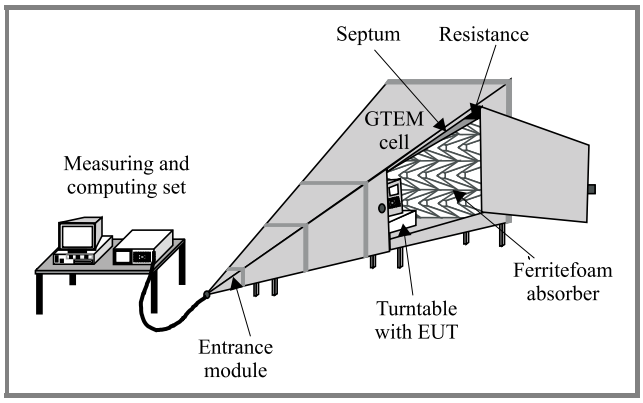


Fig. 3. Testing of radiated emission based on GTEM cell.

Sometimes some methods of radiated emission measurement are realized by using alternative manners, for example: a method based on transverse electromagnetic cell (TEM) or a method based on gigahertz transverse electromagnetic cell (GTEM). An alternative method calculates source parameters by determining its supplementary model of its emission (Figs. 2 and 3) [9, 10, 11].

3. The method of radar source identification based on using the radiated emission

The described method shown here is based on extracting some distinctive features from radiated emission, which identify an emission source. Applied prepared measuring method permits to get the set of frequency values, on which radar signals were registered. Gathered set of points is correlated with individual measured points and reflects the level of parasitic radiation. The set of measured points P is subordinated in the form of measured vectors, i.e., right-sided $\mathbf{p}^{\mathrm{p}}$ and left-sided $\mathbf{p}^{\mathrm{l}}$. These vectors are transformed into two-dimensional Euclidean space (Fig. 4).

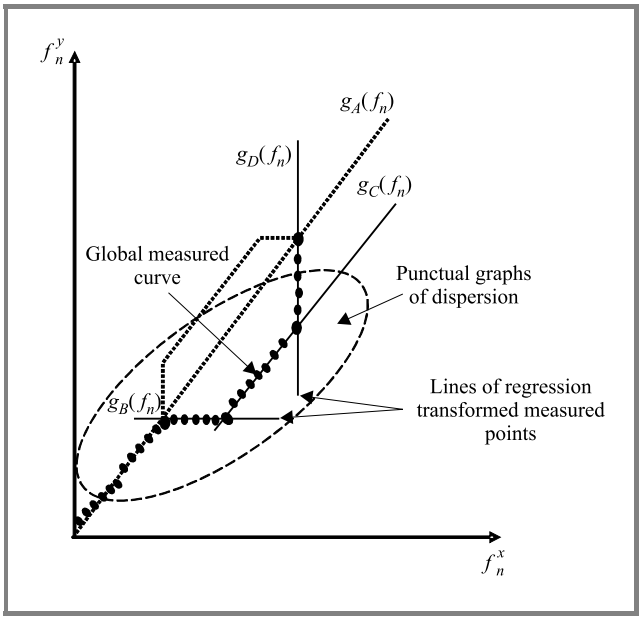


Fig. 4. The graphic image of measured points dispersion after transformation into two-dimensional Euclidean space.

Applying the regression analysis of second kind permits to specify some characteristic points. The global measured function $\hat{K}(f_n)$ is determined by calculated points P_n, where $n = 0, 1, \ldots, k_{gr}$. Figure 5 illustrates the shape of global measured function. The $\hat{K}(f_n)$ function is used to extract some radiated emission features, which modify

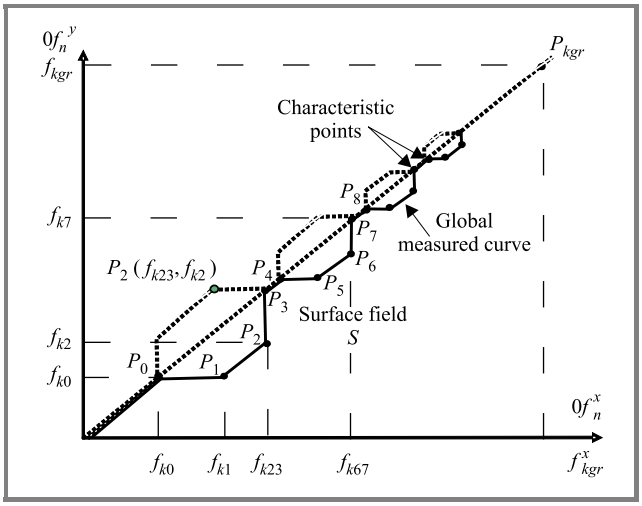


Fig. 5. The graphic image of generalized measured function crossing through appointed characteristic points.

structure of the extended vector parameters (EVP). At the end of the procedure, a radar emitter source identification is performed. During the final part of emitter identification process some distance functions (e.g., Euclidean, Mahalanobis, Hamming) are applied. The process of recognition is connected with the database, which is an important element in the modern electronic intelligence system. Some distinctive features extracted from radiated emission are used for special "radar signature" description in the database [4].

The global measured $\hat{K}(f_n)$ function in the form of a Lagrange polynomial k-degree, specified through $k+1$ characteristic points can be performed in the following way:

$$\hat{K}(f_n) = a_k f_n^k + a_{k-1} f_n^{k-1} + a_{k-2} f_n^{k-2} + \ldots + a_0, \qquad (1)$$

where: $a_k, a_{k-1}, \ldots, a_0$ – some characteristic parameters of global measured function.

The $\hat{S}$ feature, defining the surface field value, extending from the figure of the generalized measured function $\hat{K}(f_n)$ in selected band $\langle f_n^{\min}, f_n^{\max}\rangle$ into the axis $0\, f_n^x$ will be expressed by appropriate equation:

$$\hat{S} = \int_{f_n^{\min}}^{f_n^{\max}} \hat{K}(f_n)\, d f_n$$

$$= \int_{f_n^{\min}}^{f_n^{\max}} \left(a_k f_n^k + a_{k-1} f_n^{k-1} + a_{k-2} f_n^{k-2} + \ldots + a_0\right) d f_n. \qquad (2)$$

Simultaneously, the arc length of $\hat{K}(f_n)$ function as a distinctive $\hat{L}$ feature of radar emission will be expressed in accordance with appropriate equation:

$$\hat{L} = \int_{f_n^{\min}}^{f_n^{\max}} \left[1 + \left(\frac{\partial \hat{K}(f_n)}{\partial f_n}\right)^2\right]^{\frac{1}{2}} d f_n$$

$$= \int_{f_n^{\min}}^{f_n^{\max}} \left[1 + \left(k a_k f_n^{k-1} + (k-1) a_{k-1} f^{k-2} + \ldots + a_1\right)^2\right]^{\frac{1}{2}} d f_n. \qquad (3)$$

An acquaintance of characteristic points $\left(P_0, P_1, P_2, \ldots, P_{kgr}\right) \in \hat{K}(f_n)$ makes its possible to calculate a Lagrange polynomial approximation of a k-degree. In this way the structure of basic radar vector parameters is modified by calculated features $\hat{S}$ and $\hat{L}$.

4. Conclusion

The analysis of a field size under the measuring function $\hat{K}(f_n)$ and calculation of a length of its arc into selected band $\langle f_n^{\min}, f_n^{\max}\rangle$ introduces to the radar signature additional features which modify the structure of basic parameters vector. These features in the form of $\hat{L}$ and $\hat{S}$ are executed by measurement and analysis of the radar radiated emission. A modern electronic intelligence system should utilize the above mentioned non-intentional property of electronic devices during the process of their identification. For these reasons some requirements connected with parasitic radiation of electronic devices belong at present to the basic category of requirements such as resistance to mechanical or climatic exposures. Taking all these points into consideration, applying the radiated emission to the specific emitter identification is an essential element in the formation of the examined system. The capability of an ESM/ELINT system to correctly identify detectable radar emissions in a dense environment is a key to their application in modern command, communication and control system. The problem of radiated emission is essential with respect to electromagnetic compatibility.

References

[1] "C21: The Intelligence Community in the 21st Century. MASINT: Measurement and Signatures Intelligence", http://www.fas.org/irp/congress/1996_rpt/ic21/ic21007.htm

[2] "Limits and methods of measurement of electromagnetic disturbance characteristic of industrial, scientific and medical, radio-frequency equipment". CISPR Publication 11, 1990.

[3] L. Crawford and J. Workman, "Using a TEM cell for EMC measurements of electronic equipment", NBS Technical Note 1013, US Department of Commerce, Washington, 1981.

[4] J. Dudczyk, J. Matuszewski, and M. Wnuk, "The relational modelling approach to designing the emitter database", in *Proc. 3rd Int. Conf. Complem. Lad. Rad.*, Prague, Czech Republic, 2002.

[5] L. Francart, "Mastering information", in *Proc. 3rd Int. EW Conf. Expos.*, Zurich, Switzerland, 2000.

[6] "Intelligence collection", http://lga-inc.com/products/dali/example.htm

[7] PN-EN 55022:2000, "Kompatybilność elektromagnetyczna (EMC). Urządzenia informatyczne. Charakterystyki zaburzeń radioelektrycznych. Poziomy dopuszczalne i metody pomiaru", (and: PN-EN 55022:2000 / A1:2002 (U); PN-EN 55022:2000 / A1:2003; PN-EN 55022:2000 / A2:2004), (in Polish).

[8] W. Rotkiewicz, *Electromagnetic Compatibility in Radio-technique*. Warszawa: WKŁ, 1978.

[9] L. Sreenivasiah, D. C. Chang, and T. M. Ma, "Emission characteristics of electrically small radiating sources from tests inside a TEM cell", *IEEE Trans. EMC*, vol. EMC-23, no. 3, pp. 113–121, 1981.

[10] W. Więckowski, D. Bem, and Z. Jóskiewicz,"GTEM cell in the emission tests for electronic equipment", in *Proc. Int. Symp. EMC*, St. Petersburg, Russia, 1995.

[11] T. Więckowski, *The Radiation Measurement of Electric and Electronic Equipment*. Wrocław: Wrocław Polytechnic Press, 1997.

[12] L. Zachary, "The measure of MASINT", http://www.fas.org/MASINT_JED.htm



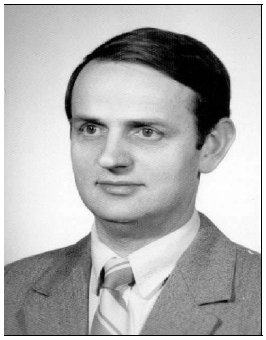
Janusz Dudczyk received the M.Sc. degree in electronics engineering from the Military University of Technology, Warsaw, Poland, with a first class honours. He studied at the electronics and cybernetics faculties (1992–1997). In 2004 he received Ph.D. degree from Military University of Technology (Electromagnetic Compatibility Faculty) with a first class honours, also. His primary research interests include sophisticated process of emitter sources classification and identification, radar signal processing and application an artificial intelligence to radar signal recognition. But especially, his research activity and interests are in the areas of electromagnetic compatibility, utilization of relational modelling to the emitter database design and applying the radiated emission to the specific emitter identification (SEI).

e-mail: jdudczyk@wp.pl
Military Unit 4159 Skierniewice
Kilińskiego st 27
96-100 Skierniewice, Poland



Marian Wnuk was born in Lublin, Poland, in 1943. He studied measure systems at Technical University of Warsaw, Poland, where he received the M.Sc. degree in 1968. In 1987 and 1999, he received the Ph.D. and D.Sc. degrees, respectively, from Military University of Technology (MUT) both in communications systems. From 2000 he has been a Professor at MUT. He is a member of IEEE, Electromagnetic Academy in MIT, and AFCEA of present the v-ca president of the Polish Chapter of AFCEA. He is a member of many research councils of the polish universities and research industrial institutes. Dr. M. Wnuk specialises in problem concentration of the antenna field analyses and construction of the antenna on a dielectric layer as well as in the electromagnetic compatibility of communications systems. He has received awards of the Minister of National Defence for his outstanding scientific achievements and practical application of their results.

e-mail: mwnuk@wel.wat.edu.pl
The Institute of Telecommunication Systems
Military University of Technology
Gen. S. Kaliskiego st 2
00-908 Warsaw 49, Box 50, Poland



Jan Matuszewski was born in Cekcyn, Poland, in 1948. In 1972 having earned a M.Sc. degree he graduated from the Military University of Technology, where he studied at the Cybernetics Faculty (1967–1972). In 1984 he obtained a scientific degree of Ph.D. He has been working at the Military University of Technology for 30 years, where now is a lecturer of electronic warfare. His subject of interests is everything that is connected with electronic warfare but especially radar signal processing, emitter classification and identification, designing emitter data base, application of neural network and expert systems to radar signal recognition. He has published 65 papers in the proceedings of conferences which were held in different towns in Poland and abroad. He completed from the "Overseas Officers Electronic Warfare Course" in Royal School of Signals in Blandford Camp in England in 1996. Since 1999 he has taken part in EW conferences that are organised by EW Section of SHAPE. He is also a member of NEDBAG (NATO Emitter Data Base Advisory Group).

e-mail: jmatuszewski@wel.wat.edu.pl
The Institute of Radioelectronics
Military University of Technology
Gen. S. Kaliskiego st 2
00-908 Warsaw 49, Box 50, Poland

Paper

Broadside coupled stripline with double-side UC-PBG structure

Paweł Meissner and Marek Kitliński

Abstract—A stripline waveguide with double-side UC-PBG pattern is considered. To verify usefulness of the stripline structure with UC-PBG a 3 dB coupler has been designed and fabricated. Reduction of the coupler size (due to slow wave effect) has been predicted and observed. Numerical and experimental investigation confirmed enhanced backward coupling phenomena.

Keywords— UC-PBG, uniplanar photonic bandgap, coupler, 3 dB coupler, broadside coupled line coupler, stripline coupler, slow-wave effect, photonic , PBG bandgap, electromagnetic bandgap, EBG.

1. Introduction

A large number of papers treating about uniplanar compact photonic bandgap (UC-PBG) have been presented recently. By affecting continuity of solid metallic ground plane there is possibility to influence wave propagation in the waveguide. It gives another degree of freedom in designing microwave devices. Usage of microstrip with UC-PBG has been well investigated [1–8]. In order to explain a shape and physical meaning of the etched structure the process of developing of the UC-PBG unit cell can be presented in few stages. In the first stage one can divide the ground plane to square patches (Fig. 1a). Adjacent edges of patches make a capacitance in the ground plane. In the second stage, in order to achieve certain inductance one can join adjacent edges of patches with narrow strips (Fig. 1b). Finally, it is possible to increase its inductive effect by making an insets in the patches (Fig. 1c) [2–4]. The microstrip line with a ground plane consisting of a two-dimensional periodic pattern in ground plane reveals slow-wave property and exhibits cut-off frequency [2]. Above the cut-off the propagation of electromagnetic wave vanishes (Fig. 5). It is possible to control cut-off frequency and slow-wave effect by changing dimensions of the structure (influencing inductance and capacitance per unit length of microstrip line [2, 3]). The series reactive elements combined with the shunt capacitances determine the propagation constant of the microstrip with UC-PBG. The propagation coefficient is higher than that of conventional microstrip line; this can be expressed in higher value of the effective permittivity ε_{eff} [1–3]. It was also shown that cut-off frequency and slow-wave factor SWF $= (\beta/k_0)$ are almost independent of alignment of the strip above the ground plane pattern. Moreover it was presented [2, 3] that insertion loss of the line is comparable to the classical microstrip. Additionally it was proved that slow-wave factor changes with frequency and achieves quite high values near cut-off frequency of UC-PBG structure [1–7]. For small frequencies SWF is higher than for microstrip with solid ground plane and is almost linear. In consequence low dispersion is ensured and the structure is suitable for broadband operation. For devices working near cut-off it is possible to obtain high degree miniaturization. Taking into account certain similarity of microstrip and stripline structures, the stripline waveguiding structure with UC-PBG operating below cut-off frequency is considered. To confirm usefulness of this modified waveguiding structure the stripline broadside coupler with UC-PBG periodic ground plane on both sides is presented. In the design procedure the enhanced backward coupling and a shortage of the $1/4\lambda$ section has been assumed.

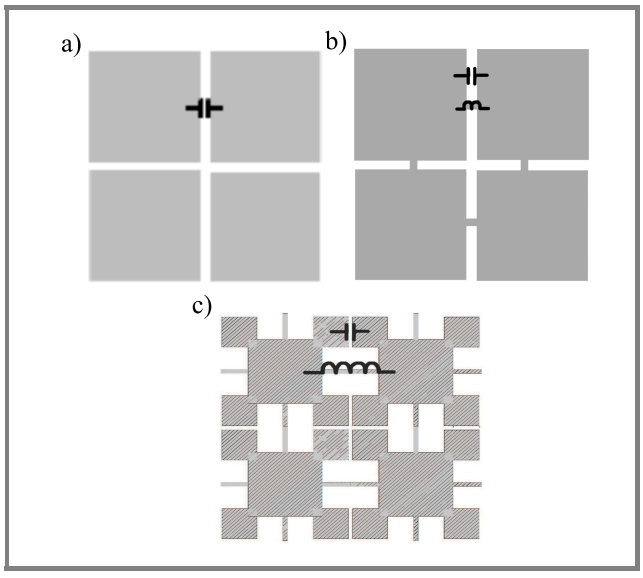


Fig. 1. An idea of developing four adjacent cells of 2D periodic pattern of UC-PBG: (a) adjacent edges of patches make a capacitance in the ground plane; (b) in the second stage, in order to achieve certain inductance one can join adjacent edges of patches with narrow strips; (c) finally, it is possible to increase its inductive effect by making an insets in the patches.

2. Broadside coupled stripline with UC-PBG – designing procedure

The slow wave effect and cut off frequency of UC-PBG depends mainly on the lattice dimensions. Simulation used in the construction is based on square lattice developed in UCLA [2], although the dimensions of lattice are

results obtained for microstrip line can be adopted as a first step for designing process. The slow-wave structure slightly changed to achieve lower cut-off frequency, i.e., $f_c \approx 8.5$ GHz. Cut-off is defined as the frequency for which the insertion loss of the structure falls below –3 dB.

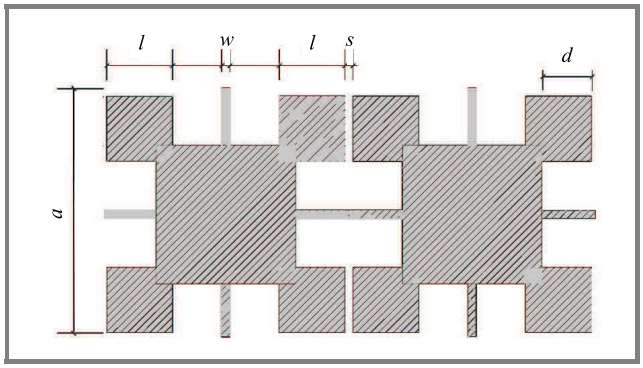


Fig. 2. Two adjacent UC-PBG cells. Dimensions: $a = 3$ mm, $d = 0.6$ mm, $l = 0.8$ mm, $s = w = 0.1$ mm.

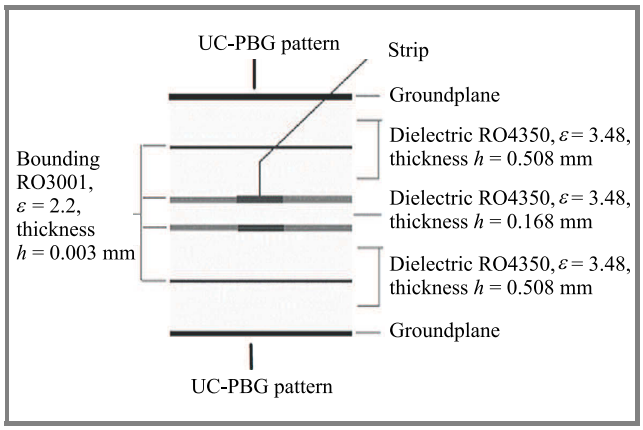


Fig. 3. A cross-section of the coupler, dielectric and metal layers.

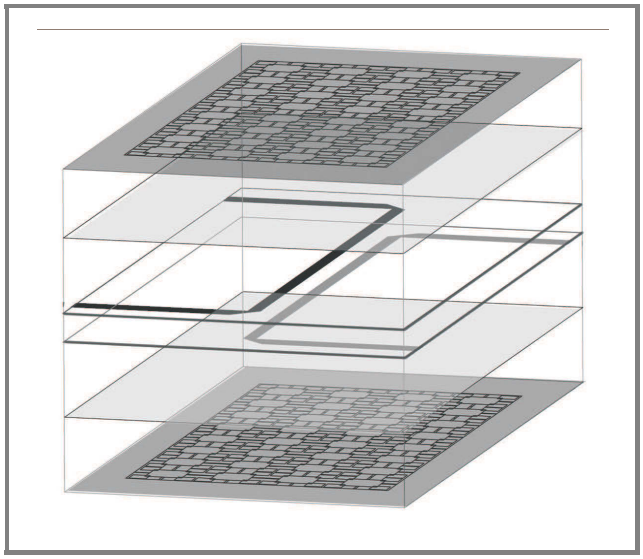


Fig. 4. A multilayer coupler with UC-PBG lattices etched in ground planes.

Spacing between cells and strips width (Fig. 2) are equal $s = w = 0.1$ mm, while in [2] $s = w = 0.25$ mm.
To prove usefulness of the broadside coupled stripline with UC-PBG a multilayer coupler has been designed and fabricated (Figs. 3 and 4). The main advantage of usage of the UC-PBG structure is the size reduction due to slow-wave phenomenon existing in the structure.
Measured cut-off frequency of the waveguide with lattice (Fig. 2) is about 8.5 GHz (Fig. 5). The center operating frequency of the coupler has been chosen as 1.4 GHz, which can ensure low dispersion (broadband operation).

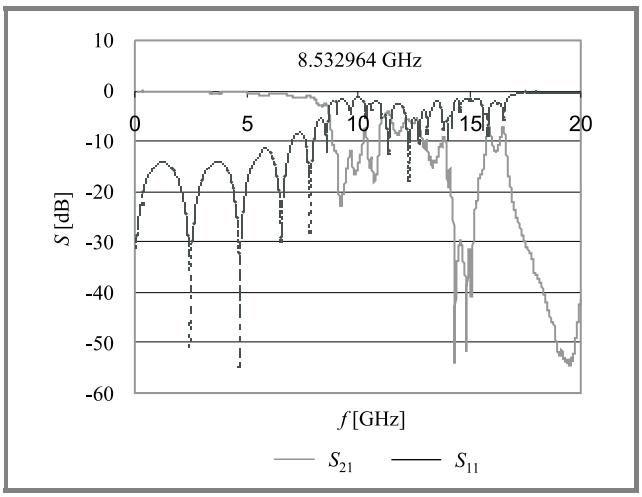


Fig. 5. Measured scattering parameters of the waveguide with the UC-PBG lattice dimensions from Fig. 2.

At the same time the slow-wave factor is relatively small, but measurements of the coupler shows that even for operating frequency far below the cut-off it is possible to obtain 20% miniaturization in comparison to a classical structure.

3. Electromagnetic simulations

Analyses has been performed using full-wave electromagnetic simulator Sonnet EM 9.52. Although the moment's method incorporated in the Sonnet EM is useful it requires

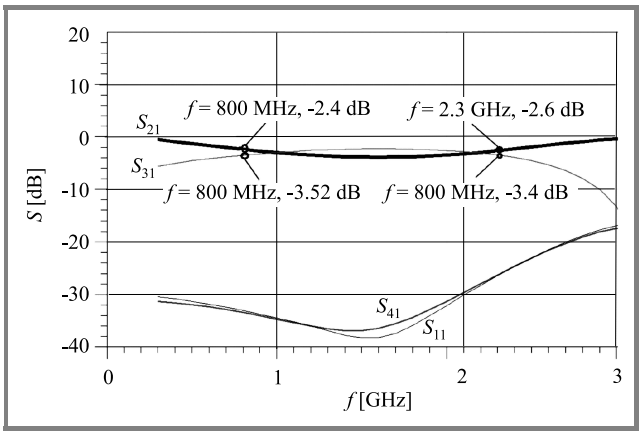


Fig. 6. Simulated characteristics of the stripline coupler with UC-PBG lattice in both ground planes.

a lot of RAM and time [9]. For obtaining some numerical results in reasonable time period (i.e., several hours for single frequency) whole structure has been divided into 4 symmetrical parts. Only one of them has been simulated using Sonnet EM 9.52 and then whole scattering matrix has been determined using circuit analysis (Agilent ADS 2002C [10]). Simulation results are presented in Fig. 6. To overcome influence of the package on the coupler performance some electromagnetic simulations have been done and minimal distance between UC-PBG and metal wall has been found as 2 mm (0.01λ in free space).

4. The coupler construction

The coupler consists of broadside-coupled striplines with UC-PBG lattice on the both ground planes. The dielectric layer between strips has been assumed as $h = 168$ mm thick Rogers substrate RO4350B. Dielectric layers relative permittivity is $\varepsilon = 3.48$ and bonding permittivity is $\varepsilon = 2.2$. The lattice dimensions are as follows (Fig. 2): $a = 3$ mm, $d = 0.6$ mm, $l = 0.8$ mm, $s = w = 0.1$ mm. Feeding sections has been considered as offset stripline with solid ground plane. The overall dimensions of the structure are 15.8 mm $\times$ 32.3 mm $\times$ 2.212 mm (Figs. 7 and 8). Layers were laminated under pressure with bonding RO3001 made by Rogers Co. Layers before lamination process are presented in Fig. 7. The connection of both ground plane layers is done on the edge of the structure.

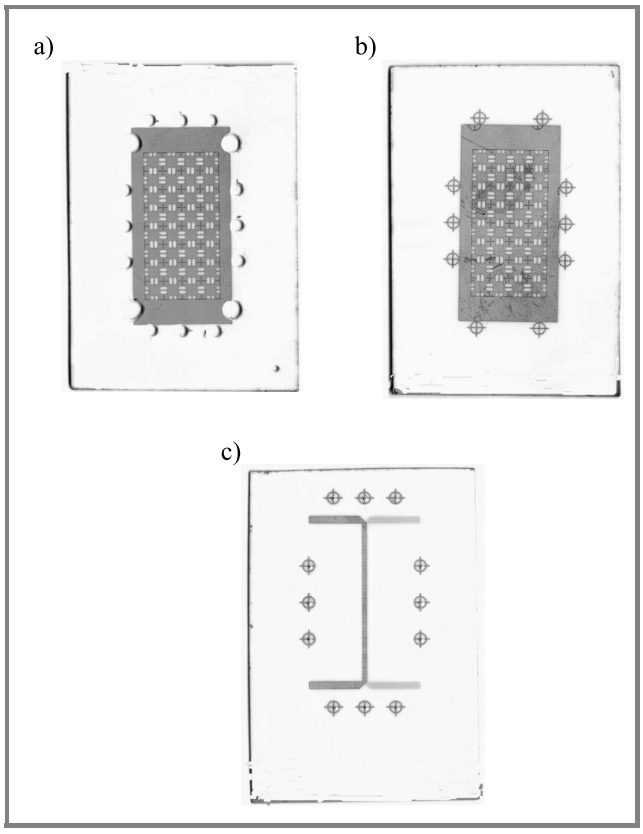


Fig. 7. Photographs of fabricated layers of coupler before lamination process: (a) and (b) UC-PBG lattice on 0.508 mm thick substrate; (c) strips on 0.168 mm thick substrate. Dimensions of the ground plane layer are: 15.8mm $\times$ 32 mm. Length of the coupled lines section is 26 mm.



Fig. 8. Photography of fabricated coupler with SMA connectors prepared for measuring.

There is no need for via holes. Fabricated and prepared for measurement coupler structure is presented in Fig. 8.

5. Measurements

In Fig. 9 measured characteristics of the stripline coupler with UC-PBG lattice are demonstrated. The measurements have been performed by Wiltron 37269A VNA. The results

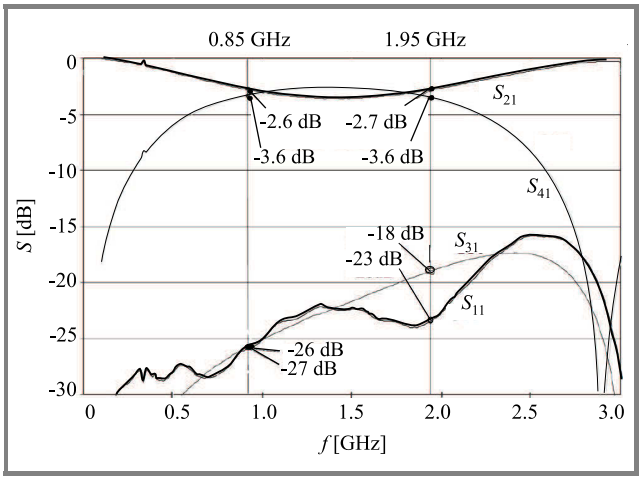


Fig. 9. Measured S – parameters of the broadside stripline coupler with UC-PBG.

show enhanced bandwidth up to 78% in comparison to 70% bandwidth of classical solid ground plane structure with the center frequency of 1.4 GHz. It is achieved by increasing of the coupling in the middle of the band. This structure has a 3 dB-coupling operating band (with +/–0.5 dB variation of the coupling coefficient) from 0.85 GHz to 1.95 GHz. The structure is about 20% shorter than comparable solid ground plane structure. It is necessary to underline that reduction of size is caused by the slow-wave effect generated by UC-PBG pattern.

6. Conclusions

Usefulness of the coupled stripline structure with UC-PBG lattice operating below cut-off frequency has been verified. Existing of slow-wave phenomena has been predicted end verified experimentally. Even for low operating frequency (far below cut-off, i.e., 1.4 GHz) it is possible to obtain 20% reduction of device size. Moreover one can expect that by choosing higher center frequency one can increase size reduction ratio. The package influence on stripline coupler characteristics was investigated. The results show that it is negligible if the distance between UC-PBG and metal wall is at least 0.01λ (center frequency) in the free space.

A 3 dB broadside coupled stripline coupler with UC-PBG was designed and fabricated. The coupler length is reduced 20% due to the slow wave effect. Results of simulation and measurement exhibit enhanced bandwidth up to 78% with center frequency 1.4 GHz. In addition the results confirm increasing of the coupling coefficient up to 2.5 dB in the center of the band.

References

[1] F. R. Yang, K. P. Ma, Y. Qian, and T. Itoh, " A uniplanar compact photonic-bandgap (UC-PBG) structure and its applications for microwave circuits", *IEEE Trans. Microw. Theory Techn*., vol. 47, no. VIII, pp. 1509–1514, 1999.

[2] C. C. Chang, R. Coccioli, Y. Quian, and T. Itoh, "Numerical and experimental charakterization of slow-wave microstrip line on periodic ground plane", *IEEE MTT-S Int. Microw. Symp. Dig*., 2000, vol. III, pp. 1533–1536.

[3] V. Radisic, Y. Qian, R. Coccioli, and T. Itoh, "Novel 2-D photonic bandgap structure for microstrip lines", *IEEE Microw. Guided Wave Lett.*, vol. VIII, pp. 69–71, 1998.

[4] Y. Qian and T. Itoh, "Planar periodic structures for microwave and millimeter wave circuit applications", *MTT-S Int. Microw. Symp. Dig.*, 1999, vol. IV, pp. 1533–1536.

[5] F. R. Yang, Y. Qian, and T. Itoh, "A novel uniplanar compact PBG structure for filter and mixer applications", in *MTT-S Int. Microw. Symp. Dig.*, 1999, vol. VIII, pp. 919–922.

[6] C. C. Chang, Y. Quian, and T. Itoh, "Enhanced forward coupling phenomena between microstrip lines on periodically patterned ground plane", in *IEEE MTT-S Int. Microw. Symp. Dig.*, 2001, vol. III, pp. 2039–2042.

[7] F. R. Yang, R. Coccioli, Y. Qian, and T. Itoh, "Analysis and application of coupled microstrip on periodically patterned ground plane", in *IEEE MTT-S Int. Microw. Symp. Dig.*, 2000, vol. III, pp. 1529–1532.

[8] K. P. Ma, J. Kim, F. R. Yang, Y. Qian, and T. Itoh, "Leakage suppresion in stripline circuits using a 2D photonic bandgap lattice", in *IEEE MTT-S Int. Microw. Symp. Dig.*, 1999, vol. 1, pp. 73–76.

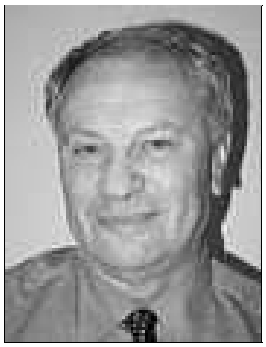
[9] Sonnet EM 9.52. Application notes, 2003.

[10] Agilent ADS 2002c. Application notes, 2003.



Paweł Meissner was born in Gdańsk, Poland, in 1978. He received the M.Sc. degree in microwave engineering from the Gdańsk University of Technology. From 2003 was working on EBG/PBG structures at Department of Microwave and Antenna Engineering Gdańsk University of Technology. He takes a post of constructor in Vector Company now.

e-mail: p.meissner@vector.com.pl
Department of Microwave and Antenna Engineering
Gdańsk University of Technology
Narutowicza st 11/12
80-952 Gdańsk, Poland



Marek Kitliński was born in Sopot, Poland, in 1947. He received the M.Sc.E.E., Ph.D., and habilitation degrees from the Gdańsk University of Technology, Gdańsk, Poland, in 1969, 1975 and 1987, respectively. From 1984 to 1987 he was a Researche Associate with the Kernforschungszentrum Karlsruhe, Karlsruhe, Germany. Since 1987 he is an Associate Professor with Gdańsk University of Technology, Gdańsk, Poland. His research interests include ferrite devices, integrated circuits for microwave and millimeter wave applications, integrated antennas for wireless communication.

e-mail: maki@eti.pg.gda.pl
Department of Microwave and Antenna Engineering
Gdańsk University of Technology
Narutowicza st 11/12
80-952 Gdańsk, Poland

Paper

All-optical intensity noise suppression for solid-state and semiconductor lasers

Márk Csörnyei, Tibor Berceli, and Tamás Marozsák

Abstract—This paper will report on a new all-optical technique of relative intensity noise (RIN) suppression for solid-state and semiconductor lasers. The new scheme we have used is based on an unbalanced Mach-Zehnder interferometer (UMZI), which is able to cancel the intensity noise enhancement at relaxation resonance. Although the relaxation oscillations frequency and the level of the corresponding noise maximum are extremely different concerning solid-state microchip lasers and semiconductor laser diodes, the proposed passive noise suppression is well suited for both types of laser sources used in telecommunication. The UMZ fiber interferometer solution for solid-state lasers demonstrated hereunder was generalized and deployed in case of semiconductor lasers as well.

Keywords— laser noise, neodymium:solid lasers, optical communication, semiconductor lasers.

1. Introduction

The optical generation of microwaves by using two-frequency solid-state lasers (SSLs) presents an efficient way of generating and transmitting high quality local oscillator signals in fiber-radio and radar systems. Diode pumped microchip lasers like Nd:YVO_4 can operate in two or three longitudinal modes with a frequency difference defined by the crystal geometry. After optical detection these modes provide beat notes in the microwave and millimeterwave range, which can be used as high-purity signals for further processing in telecommunication systems.

Due to their outstanding phase-noise characteristics and high output power, rare-earth doped solid-state lasers can be put to use in distribution networks and common antenna television (CATV) systems as well.

However they show a significant intensity noise enhancement at the relaxation oscillations quite close to the optical carrier. In order to reduce this resonance term in the relative intensity noise (RIN) spectrum, a number of opto-electronic feedback loops have been reported in the literature. Kane [1] and Harb [2] have designed electronic feedback systems for intensity noise reduction in diode pumped Nd:YAG lasers. In the same way, Geronimo [3] and Taccheo [4] have examined the RIN reduction in an ytterbium-codoped erbium glass laser. Concerning our previous report, Csörnyei *et al*. [5], significant noise suppression was achieved by using opto-electronic feedbacking in case of a Nd:YVO_4 microchip laser.

In this paper we present a new all-optical solution for intensity noise suppression. Instead of using an electronic control loop, an unbalanced Mach-Zehnder fiber interferometer (UMZI) with a free spectral range (FSR) of 2 MHz is employed to put down the noise peak at the relaxation resonance.

The new passive noise cancellation scheme we have mentioned in the preceding discussions can be universalized and applied concerning semiconductor laser diodes as well. Similarly to microchip lasers the RIN is one of the most important impairments in laser diode based optical transmitters too. In that case the relaxation oscillation has got much higher frequency and damping which results in a quite broad and flat noise increment in the microwave domain. Due to these characteristics the laser diode intensity noise is not a limiting factor in optical generation of high quality microwave signals like in solid-state lasers, but significantly raises the overall noise floor of the optical link. Concerning this motivation it is also worth dealing with RIN suppression of laser diodes by using an extended version of an unbalanced fiber interferometer.

The paper consists of two parts. In the first part possible noise reduction is discussed in case of a Nd:YVO_4 microchip laser, the second shows the extension of our approach to semiconductor laser diodes. The structure is as follows. Section 2 presents the optical subsystem containing a Nd:YVO_4 SSL and the all-optical noise suppression. Sections 3 and 4 describes the measurement and simulation results of a laser diode RIN reduction. Section 5 summarizes the results so far and further possible efforts in this field.

2. UMZI for noise suppression of Nd:YVO_4 microchip laser

2.1. Characterization of the Nd:YVO_4 SSL system

The laser system we considered and the optical spectrum of the two frequency microchip laser output can be seen in Figs. 1 and 2, respectively. The two longitudinal modes of our Nd:YVO_4 crystal laser are 60 GHz apart. This dual wavelength operation makes use of this type of solid-state lasers in optical generation of microwave and millimeterwave signals.

The laser crystal is pumped optically by an SCT100-808-Z1-01 high power laser diode at a wavelength of 808 nm.

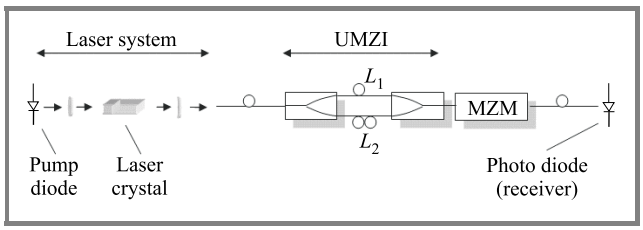


Fig. 1. Diode pumped solid-state laser followed by an UMZI for intensity noise cancellation. The information signal to be transmitted can be modulated on to the optical carrier by a Mach-Zehnder modulator. (The photodiode represents one of the possible receivers in the optical network.).

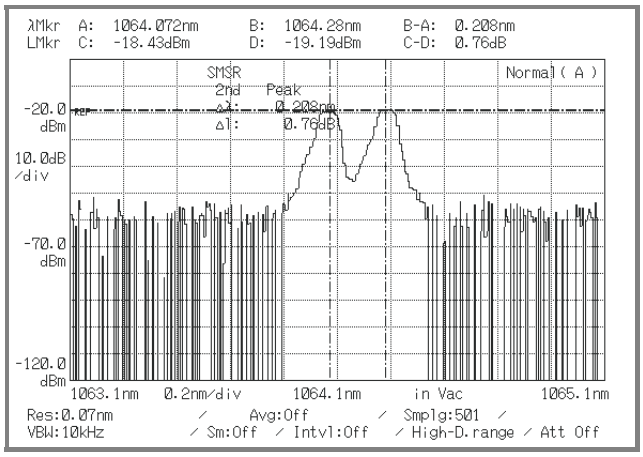


Fig. 2. The two longitudinal modes of the Nd:YVO_4 solid-state laser with a frequency difference of 60 GHz. It was captured by an Anritsu MS9710B optical spectrum analyzer. Measurement conditions: wavelength – 1064 nm, resolution bandwidth – 0.7 nm.

The pump diode is temperature stabilized by a Peltier element and an LDT-5412 temperature controller. The laser diode had a maximal output power of 1.4 W. The pumping light is focused on the laser crystal input mirror by a Thorlabs C440TM-B lens. Being pumped the Nd:YVO_4 crystal produces an output power of 200 mW at the wavelength of 1064 nm, which is focused into the optical fiber.

Figure 3 shows the measured relative intensity noise peak of the solid-state laser. The noise level at the relaxation oscillations is 40 dB higher than one outside the resonance region. The noise peak was captured by an InGaAs photodiode followed by a 5 kΩ gain transimpedance amplifier. The detector was illuminated by a 10 mW fraction of the crystal output power. The maximum value of the noise curve was –50 dBm on the 50 Ω input impedance spectrum analyzer. Taking account of the 5 kΩ transimpedance of the receiver, the 10 kHz resolution bandwidth of the spectrum analyzer, and the $\eta = 0.8$ quantum efficiency of the InGaAs photodiode material at 1064 nm, a relative intensity noise value of –70 dBc/Hz can be evaluated. Both the frequency of the relaxation oscillations and the power of the noise peak depend on the laser diode pump power. In Fig. 3 pumping the solid-state laser by a diode power of 350 mW the intensity noise maximum had a frequency

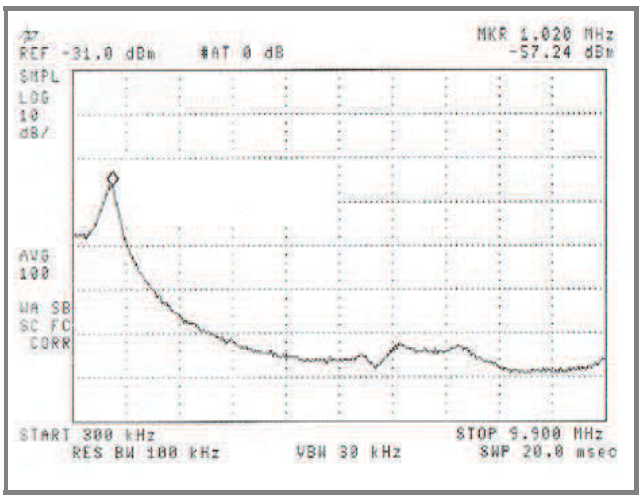


Fig. 3. Intensity noise at the relaxation frequency of 1020 kHz. The pump power was 350 mW (600 mA bias current across the pump diode). The measurement conditions are: resolution BW = 100 kHz, video BW = 30 kHz, 100 point video averaging, input attenuation = 0 dB.

difference of 1 MHz to the optical carrier. When using a constant pump power, as in normal applications, the frequency of the relaxation oscillations does not change, and thus an interferometric noise reduction is feasible.

2.2. UMZI design considerations and suppression results

Concerning the noise suppression scheme in Fig. 1, the laser output is coupled into an unbalanced Mach-Zehnder interferometer. The input 3 dB coupler divides the laser signal into the two arms of the UMZI. Properly setting the time delay difference between the two signal paths the output 3 dB coupler combines the signals with a phase shift of 180° at the relaxation oscillations frequency. Exploiting this time delay difference, the intensity noise peak can be appreciably reduced. To obtain a 0.5 μs delay difference for noise suppression at the 1 MHz resonance frequency of SSL, we considered an UMZI with a free spectral range of 2 MHz. Equation (1) shows the required fiber lengths difference for such purposes [6]:

$$\tau = T_2 - T_1 = \frac{n}{c}(L_2 - L_1) = \frac{1}{\mathrm{FSR}} \Rightarrow \Delta L = \frac{c}{n}\ 0.5\ \mu\mathrm{s} = 100\ \mathrm{m}. \tag{1}$$

According to Eq. (1) we need a 100 m fiber length difference in case of common fiber materials (refractive index: $n = 1.5$). The transfer function of the UMZI is depicted in Fig. 4. By appropriate tuning of the FSR the rejection frequency is selected at 1 MHz. Passing through the delay lines the noise enhancement at the relaxation resonance is canceled in the output 3 dB coupler. The suppression ratio at the rejection frequencies is defined by the attenuation difference of the two arms in the UMZI. Keeping this difference low an optical rejection of 30 dB is feasible. Figure 5 shows the possible intensity noise reduction at the relaxation oscillations of the Nd:YVO_4 solid-state laser.

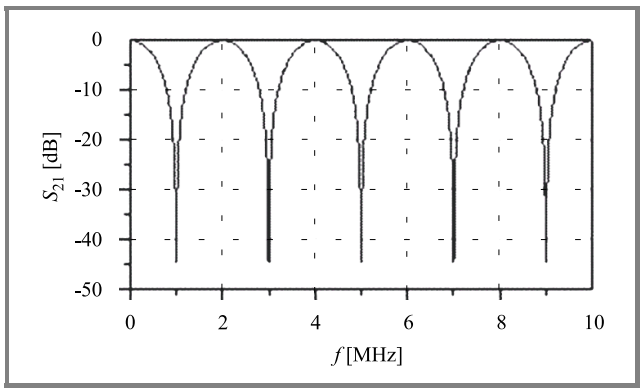


Fig. 4. The transfer function of an unbalanced Mach-Zehnder interferometer (FSR = 2 MHz) for noise reduction in Nd:YVO_4 SSLs. The required fiber length difference calculating with a refractive index of $n = 1.5$ is: $\Delta L = 100$ m.

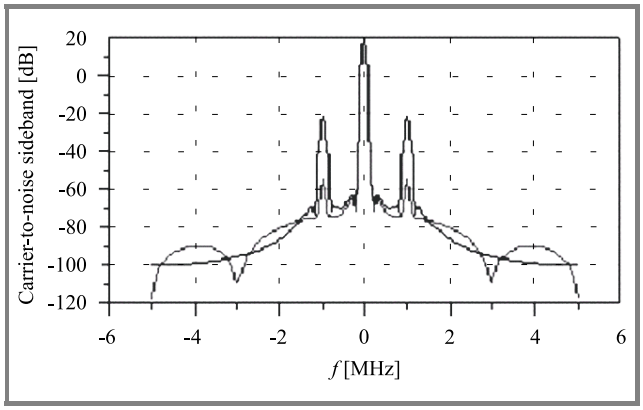


Fig. 5. The feasible intensity noise suppression at the frequency of the relaxation oscillations. There is a possible suppression of 30 dB. The further improvement is limited by the attenuation difference of the two arms in the fiber interferometer and by the damping in the photon density impulse response of the Nd:YVO_4.

The relative intensity noise peak we are dealing with can be characterized by the photon density impulse response which is a reply to small perturbations in the laser population inversion. As it is shown in Eq. (2) the photon density impulse response is a damped sinusoidal function which results in a spectral broadening around the relaxation oscillations frequency (Fig. 3):

$$\Delta\phi \approx \exp\left(\frac{\sigma c\phi}{2}\right) t \sin\left[\sigma c(\phi n)^{1/2} t\right]. \qquad (2)$$

In Eq. (2) σ is the emission crossection, n the electron population density and ϕ the photon density. Based on Eq. (2) the frequency of the oscillation can be expressed by the intercavity power density, $I = c\phi h\nu$, and the photon decay time: τ_c [9]. The frequency of the relaxation oscillations is represented in Eq. (3):

$$\omega = \sqrt{\frac{\sigma I}{\tau_c h\nu}}. \qquad (3)$$

Table 1 presents the parameters necessary to the impulse response calculations in case of the Nd:YVO_4 crystal laser.

The calculated photon density impulse response is depicted in Fig. 6. Due to the spectral broadening caused by the damped look of the impulse response there is a slight difference to the ideal suppression in Fig. 5.

Table 1
Parameters of 1.1% doped Nd:YVO_4

Attenuation	Threshold power	Emission crossection	Photon decay time	Calculated power density*)
α [1/cm]	P_{ib} [mW]	σ [cm^2]	τ_c [s]	I [W/cm^2]
9.2	78	$7 \cdot 10^{-19}$	$3.623 \cdot 10^{-12}$	4.33
*) Considering the crossection area (0.6 mm × 3 mm) of the crystal.				

Equation (3) shows the dependence of the relaxation resonance frequency on the pump power (I: intercavity power density is proportional to the pump power). In our solution compared to the optoelectronic suppression techniques the pumping rate is kept constant and thus a noise reduction fixed to an effective pumping rate is feasible.

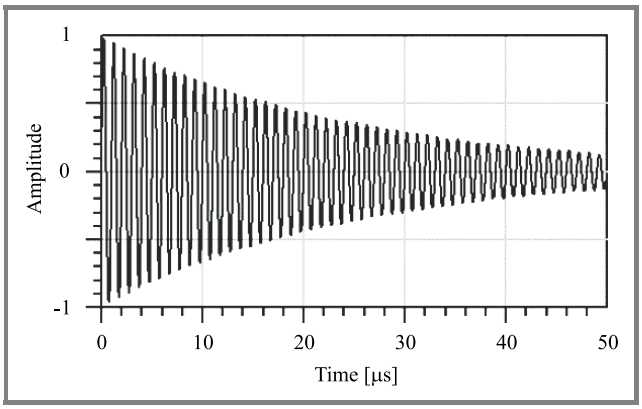


Fig. 6. The photon density impulse response of the Nd:YVO_4 solid-state laser crystal. Damping causes spectral broadening at the relaxation oscillations frequency.

The noise cancellation subsystem is followed by a Mach-Zehnder modulator (MZM) in Fig. 1. Placing the external modulator after the UMZI the information to be transmitted can be modulated on to the high quality noise reduced optical carrier.

3. UMZI for noise suppression of laser diodes

The unbalanced Mach-Zehnder interferometer based intensity noise suppression scheme for laser diodes is depicted in Fig. 7. In that structure we have utilized an InGaAsP multi-quantum well (MQW) Fabry-Perot laser diode. The output power and the operation wavelength were 0.1–2 mW and 1310 nm, respectively. The pigtailed output of the laser

diode was connected to the interferometer, which consisted of two Kamaxoptic 3 dB (50/50) splitter modules and two SMF-28 type single mode optical fiber in-between.

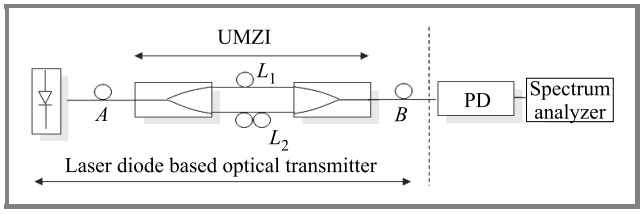


Fig. 7. Two paths unbalanced Mach-Zehnder interferometer for intensity noise suppression of semiconductor laser diodes. The fiber length difference is 1 m.

The intensity noise maximum defined by the relaxation oscillation is at 2 GHz exciting the diode by a bias current of 10 mA. According to Eq. (1) an UMZI path length difference of 0.05 m is required in order to reduce the noise at 2 GHz. A fiber interferometer with a free spectral range of 200 MHz (path length difference: 1 m, $n = 1.5$) was chosen instead because of its higher number of resonance frequencies. Increasing the path length difference between the two fiber arms of the interferometer we will end up with an increased number of suppression points in the noise spectrum, which means a higher average noise reduction.

Actually the UMZI is an optical finite impulse response (FIR) filter which has got only two taps and both of the filter coefficients are +1. Since we only have positive values for the filter coefficients the UMZI behaves as an optically

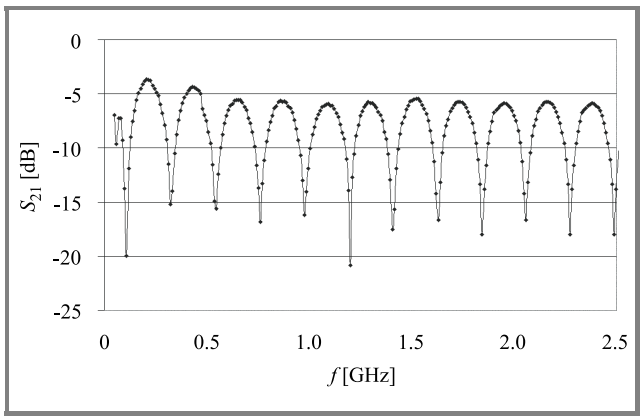


Fig. 8. The measured transfer function of the 200 MHz free spectral range unbalanced Mach-Zehnder interferometer (from *A* to *B* in Fig. 7). The fiber length difference of the two SMF-28 type optical fiber was 1 m. The measurement was taken by an HP8722D 50 MHz–40 GHz network analyzer. The measurement signal of the network analyzer was modulated on to the optical carrier by an HP83422A lightwave modulator at point *A* (Fig. 7) and detected by an HP11982A lightwave converter (1200–1600 nm) at point *B* (Fig. 7). The UMZI has an average attenuation of around 6 dB which comes from the attenuation of the optical fibers and connectors inside the interferometer. As it is shown there is a noise reduction capability of 15–20 dB at selected resonance frequencies of the UMZI.

realized low-pass filter with multiple transmission and attenuation bands. The low-pass characteristic is of prime importance because it ensures that the optical carrier itself will not be filtered out.

Figures 8 and 9 show the measured transfer function of the interferometer discussed above and the achieved noise

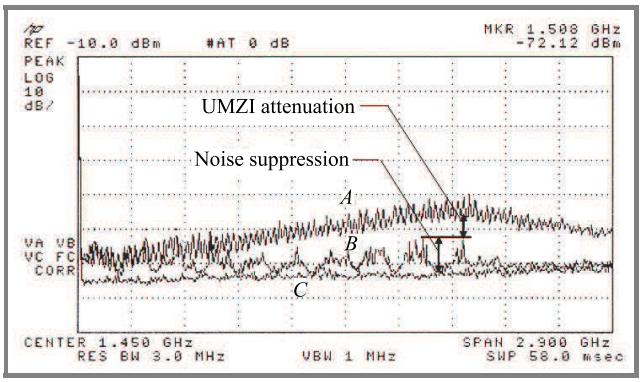


Fig. 9. The measured noise suppression of the UMZI of Fig. 7. *A* – the relative intensity noise of the investigated Fabry-Perot semiconductor laser diode around 2 GHz (point *A* in Fig. 7); *B* – the measured interferometric noise suppression (point *B* in Fig. 7); there is a periodic noise reduction of 8 – 9 dB, the periodicity corresponds to the 200 MHz FSR of the UMZI; *C* – the noise level of the measurement system. The results were captured by an HP8593E spectrum analyzer under the following conditions: resolution BW = 3 MHz, no video averaging, input attenuation = 0 dB.

reduction respectively. As it is shown in Fig. 8 the interferometer has an attenuation of about 6 dB which comes from the attenuation of optical connectors between the laser pigtail, the 3 dB couplers and the fibers. Taking account of this attenuation there is a noise reduction of 8–9 dB at the UMZI resonance frequencies around 2 GHz in Fig. 9. The further suppression is possible at the selected frequencies but the measurement is limited due to the spectrum analyzer noise floor.

4. Opto-microwave filter

In case of solid-state lasers the noise peak at the relaxation oscillations frequency is limited in a quite narrow bandwidth (noise peak linewidth: 10–50 kHz) and thus interferometric noise cancellation is a good solution. However concerning semiconductor lasers the noise enhancement is a flat and broad maximum around the relaxation resonance. Using UMZI, noise reduction is only possible at selected resonance frequencies of the interferometer (Fig. 9). To achieve overall noise suppression around the relaxation oscillations of the laser diode, the interferometer should be extended with additional fiber arms. It means we should increase the tap number in our optical FIR filter. Placing new lines with different optical delays will result in spectral broadening of the attenuation bands in the filter transfer function.

Figures 10 and 11 present the structure and the calculated transfer function of such an interferometer with three optical paths. As it is shown setting the relative delay of the new arm to 250 ps (fiber length difference: 0.05 m) the broadening of the attenuation band around 2 GHz is feasible.

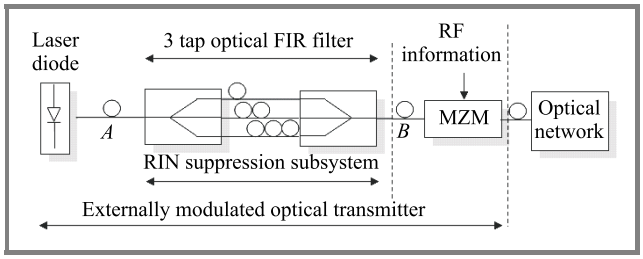


Fig. 10. Three paths interferometric noise suppression system for semiconductor laser diodes. The laser light passing through the interferometric filter can be modulated externally and sent to the optical communication network.

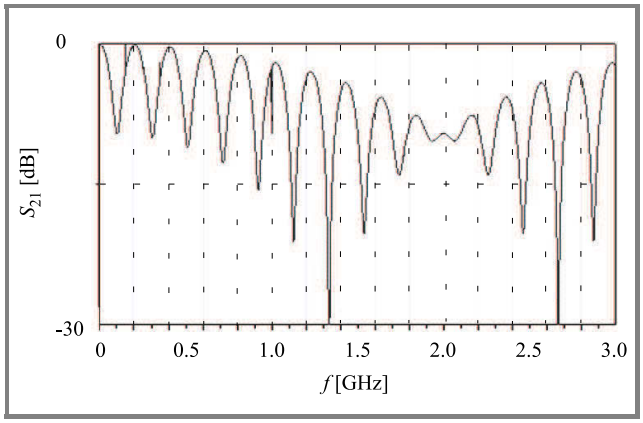


Fig. 11. The calculated transfer function of the interferometric noise cancellation system shown in Fig. 10. There is a 10 dB suppression capability around 2 GHz.

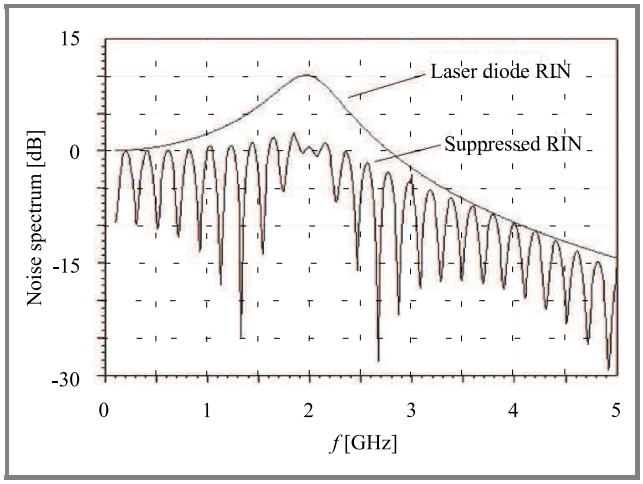


Fig. 12. The calculated noise suppression of a three paths UMZI (Fig. 10). The spectral density function of the laser diode RIN was approximated by the transfer function of a linear system [5]. The possible noise power reduction in this interferometer is 10 dB.

The possible intensity noise suppression by using the discussed interferometer is depicted in Fig. 12. The spectral density function of the laser diode relative intensity noise was approximated by a simple transfer function [5].

When applying additional arms in the interferometric filter, significant improvement takes place in the noise suppression capability of the proposed scheme. Figure 12 shows a 200 MHz attenuation band around the relaxation oscillations which is five times wider than when we use a simple two paths interferometer.

5. Conclusion

In our paper a new method of relative intensity noise suppression for both solid-state lasers and semiconductor laser diodes has been demonstrated.

As we have seen in Section 2, all-optical relaxation resonance cancellation is feasible for solid-state microchip lasers in case of applying an unbalanced Mach-Zehnder interferometer in the laser transmitter section. If the adequate time delay difference between the two arms of the UMZ fiber interferometer is adjusted the noise sidebands of the optical carrier almost disappear.

Concerning the case of semiconductor laser diodes, additional efforts have to be made in the field of filter design in order to achieve sufficient suppression in the band of the noise maximum.

Compared to the optoelectronic suppression techniques there is no need for electronic circuit design and maintainance in our scheme. Since there are only passive devices, the design of biasing and supply systems and the corresponding power consumption is avoidable as well. Due to the all-optical solution, the problem of electromagnetic interference does not need to be faced, which – owing to the low frequency (LF) radio broadcasting – causes major impairments. Furthermore, due to the feedbacking, the application of the well known optoelectronic system causes some noise enhancement outside the suppression region [2, 5], which falls out of our newly introduced approach.

In order to be able to achieve a robust system, precise temperature stabilization of the optical devices is required. In this aspect, integrated optical realization can provide considerable advantages, since the use of simple Peltier-elements will be possible.

Lithium niobate based integrated optics can deliver other benefits as well. Due to the voltage dependence of the refractive index in this material [10], tuning of the delay lines in the unbalanced Mach-Zehnder interferometer by applied voltage is feasible. According to this property a more flexible operation is realizable, where the interferometer can follow the changes caused by the pump power (SSL) or bias current (laser diode) variation of the relaxation oscillation frequency. The requirement of using tunable noise suppression systems can occur in dynamic optical networks where the number of optical nodes and thus the required transmitter power has to be changed.

Acknowledgment

The authors acknowledge the grant of the "National Research Foundation" (OTKA) no. T042557, and the grant of the "Foundation of the Industry for Modern Engineering Education" (IKMA).

References

[1] T. J. Kane, "Intensity noise in diode-pumped single-frequency Nd:YAG lasers and its control by electronic feedback", *IEEE Photon. Technol. Lett*., vol. 2, no. 4, 1990.

[2] C. C. Harb, M. B. Gray, H.-A.Bachor, R. Shilling, P. Rottengatter, I. Freitag, and H. Welling, "Suppression of the intensity noise in a diode-pumped neodymium: YAG nonlinear ring laser", *J. Quant. Electron.*, vol. 30, no. 12, pp. 2907–2913, 1994.

[3] G. De Geronimo, S. Taccheo, and P. Laporta, "Optoelectronic feedback control for intensity noise suppression in a codoped erbium-ytterbium glass laser", *Electron. Lett.*, vol. 33, pp. 1336–1337, 1997.

[4] S. Taccheo, P. Laporta, O. Svelto, and G. De Geronimo, " Intensity noise reduction in a single-frequency ytterbium codoped erbium laser", *Opt. Lett*., vol. 21, no. 21, pp. 1747–1749, 1996.

[5] M. Csörnyei, T. Berceli, and P. R. Herczfeld, "Noise suppression of Nd:YVO4 solid-state lasers for telecommunication applications", *J. Lightw. Techn*., vol. 21, iss. 12, pp. 2983–2988, 2003.

[6] B. Cabon, V. Girod, and G. Maury, "Optical generation of microwave functions", in *Proc. OMW2000 Summer School,* Autrans, France, 2000.

[7] T.-Der Ni, X. Zhang, and A. S. Daryoush, "Experimental study on close-in to microwave carrier phase noise of laser diode with external feedback", *IEEE Trans. Microw. Theory Techn.*, vol. 43, no. 9, 1995.

[8] W. D. Jemison and E. Funk, "Fiber radio link with microchip laser source", in *Proc. Int. Top. Meet. Microw. Photon., MWP2003*, Budapest, Hungary, 2003, pp. 23–26.

[9] W. Koechner, *Solid-State Laser Engineering.* Berlin, Heidelberg: Springer-Verlag, 1999.

[10] B. P. Pal, *Fundamentals of Fibre Optics in Telecommunication and Sensor Systems*. New York: Wiley, 1993.



Márk Csörnyei was born in Budapest, Hungary, in 1977. He received the M.Sc. degree in electrical engineering from the Budapest University of Technology and Economics, Budapest, Hungary, in 2000. He is currently studying towards the Ph.D. degree in electrical engineering at the Budapest University of Technology and Economics. His research interest include laser noise suppression and analysis of nonlinearities in fiber radio systems.
e-mail: mark.csornyei@mht.bme.hu
Department of Broadband Infocommunication Systems
Budapest University of Technology and Economics
Goldmann György st 3, H-1111
Budapest, Hungary



Tibor Berceli was a Visiting Professor in the United States, United Kingdom, Germany, France, Finland, and Japan. He is currently Professor of electrical engineering at the Budapest University of Technology and Economics, Budapest, Hungary. He has published more than 170 papers in the field of microwave and optical communications and has written six books and received 26 patents. His present research activity is in microwave photonics.
e-mail: berceli@mht.bme.hu
Department of Broadband Infocommunication Systems
Budapest University of Technology and Economics
Goldmann György st 3, H-1111
Budapest, Hungary



Tamás Marozsák was born in Hungary in 1971. He received the M.Sc. degree in electrical engineering from the Technical University of Budapest, Budapest, Hungary, in 1995. Since 1998, he has been an Assistant Professor with the Department of Broadband Infocommunication Systems, Budapest University of Technology and Economics, Budapest, Hungary. He is author or co-author of more than 50 technical papers in the field of optical communications and microwave photonics.
e-mail: marozsak@mht.bme.hu
Department of Broadband Infocommunication Systems
Budapest University of Technology and Economics
Goldmann György st 3, H-1111
Budapest, Hungary

Paper

Mesh-free approach to Helmholtz equation based on radial basis functions

Piotr Kowalczyk and Michał Mrozowski

Abstract—Recently, a radial basis functions (RBFs) method, which was originally proposed for interpolation problems, has been developed and applied to solve partial differential equations and eigenproblems. Properties of that method (mesh-free algorithm) allows one to use it in many areas, including electromagnetics. In this paper the mesh-free RBF method for solving Helmholtz equation was applied and a new adaptive algorithm for defining the set of interpolation centers was proposed. Using the proposed approach the cutoff wavelengths and the field distribution in cylindrical waveguides of arbitrary cross-section were calculated with a high accuracy.

Keywords—Helmholtz equation, radial basis functions, mesh-free method, cylindrical waveguides.

1. Introduction

Radial basis functions (RBFs) were originally proposed for a multidimensional interpolation problem of scattered data [1]. The RBFs method is similar to the most of the interpolation methods and involves the same general idea: for a given set of distinct points $\{\mathbf{x}_j\}_{j=1}^N \in \Omega \subset \mathbb{R}^d$ (called interpolation points) the corresponding values are known $\{\Psi(\mathbf{x}_j)\}_{j=1}^N$ and the interpolant $\Psi(\mathbf{x})$ (where $\mathbf{x} \in \Omega$) is chosen such that the interpolation conditions are fulfilled. The expression for the interpolant has a following form:

$$\Psi(\mathbf{x}) = \sum_{i=1}^{N} \alpha_i \phi(||\mathbf{x} - \mathbf{y}_i||)\,, \tag{1}$$

where $||\cdot||$ is the Euclidean norm, the set $\{\mathbf{y}_i\}_{i=1}^N \in \mathbb{R}^d$ is a set of interpolation centers (usually, the same set of points is used for centers and interpolation) and finally $\phi(\cdot)$ is the radial basis function. It has to be noted that $\phi(\cdot)$ is one-argument function $\phi : \mathbb{R}_+ \to \mathbb{R}$.

There is many different types of RBFs. However, as mentioned before, choosing a particular form of RBF depends on the type of the problem. A few of the most commonly used RBFs include: the Gaussian function $\phi(r) = \mathrm{e}^{-r^2}$, the multiquadric function $\phi(r) = \sqrt{1+r^2}$ or the Wendland function which will be described later [2–4].

The argument r of the function $\phi(\cdot)$ is usually scaled by the factor c: $r \to \frac{r}{c}$, where $c \in \mathbb{R}_+$ is called a shape parameter. If c is properly selected, the accuracy of the method increases, but despite intensive research [4] the choice of the parameter c remains an unsolved problem.

For a given form of RBF, the value of the parameter c and centers distribution $\{\mathbf{y}_i\}$, one gets the interpolant from substitution of given data to Eq. (1):

$$\Psi(\mathbf{x}_j) = \sum_{i=1}^{N} \alpha_i \phi(||\mathbf{x}_j - \mathbf{y}_i||), \qquad j = 1, ..., N. \tag{2}$$

Using a matrix notation $\mathcal{A}\boldsymbol{\alpha} = \boldsymbol{\Psi}$, where $\boldsymbol{\alpha} = [\alpha_1, \cdots, \alpha_N]^T$, $\boldsymbol{\Psi} = [\Psi(\mathbf{x}_1), \cdots, \Psi(\mathbf{x}_N)]^T$ and the elements of the matrix $\mathcal{A}$ have a form $[\mathcal{A}]_{i,j} = \phi(||\mathbf{x}_i - \mathbf{y}_j||)$ for $i, j = 1, \ldots, N$.

Recently RBFs have been also applied to solve partial differential equations [5] and eigenproblems [3]. The standard numerical methods such as the finite element method or the finite-difference method require mesh generation, which often is very burdensome task, especially when the contour of the domain is of complex geometry. The RBFs method is based on extrapolation of scattered data, therefore it is very suitable schemes for problems defined in irregular geometries; its algorithm is totally grid-free.

In this paper we further develop the technique proposed in [6] to find the cutoff wavelengths and the field distribution in cylindrical waveguides of arbitrary cross-section shapes. Instead of defining the set of centers *a priori*, we propose a new adaptive algorithm.

2. Formulation

Let us assume that the wave propagates in the z-direction inside a homogeneous and uniform cylinder of arbitrary but homogeneous cross-section Ω. The problem is governed by the scalar Helmholtz equation:

$$\nabla^2 \Psi(\mathbf{x}) + k^2 \Psi(\mathbf{x}) = 0\,, \tag{3}$$

where $\nabla^2 = \dfrac{\partial^2}{\partial x^2} + \dfrac{\partial^2}{\partial y^2}$ and k is the cutoff wavenumber. For TM modes $H_z = 0$, $E_z = \Psi(\mathbf{x})$ and function $\Psi(\mathbf{x})$ satisfies the Dirichlet conditions imposed on boundary $\partial\Omega$, whereas for TE modes $E_z = 0$, $H_z = \Psi(\mathbf{x})$ and $\Psi(\mathbf{x})$ satisfies the Neumann conditions.

The problem can be solved by applying a modified form of the interpolant [6]:

$$\Psi(\mathbf{x}) = \sum_{i=1}^{n} \alpha_i \phi(||\mathbf{x} - \mathbf{y}_i||) + \sum_{i=n+1}^{N} \alpha_i (\mathbf{x} - \mathbf{y}_i) \cdot \nabla \phi(||\mathbf{x} - \mathbf{y}_i||)\,, \tag{4}$$

where the set of centers $\{\mathbf{y}_i\}_{i=1}^N \in \bar{\Omega}$ ($\bar{\Omega}$ consists of Ω and boundary $\partial\Omega$) are chosen arbitrarily, but in such a way

that n of y_i are inside Ω and the rest of them are on boundary $\partial\Omega$. The second term in Eq. (4) is due to the first-order approximation by the Taylor series expansion and it is included to improve the accuracy of the derivatives. Function $\phi(\cdot)$ is the Wendland radial basis function of the following form

$$\phi(r) = (1-r)_+^8 (32r^3 + 25r^2 + 8r + 1), \tag{5}$$

where $(1-r)_+ = \begin{cases} 1-r, & r \in (0,1) \\ 0, & otherwise \end{cases}$.

Substituting Eq. (4) into Eq. (3) one gets

$$\begin{aligned} &\sum_{i=1}^{n} \alpha_i \nabla^2 \phi(||\mathbf{x}-\mathbf{y}_i||) \\ &+ \sum_{i=n+1}^{N} \alpha_i \nabla^2 \left[(\mathbf{x}-\mathbf{y}_i)\cdot\nabla\phi(||\mathbf{x}-\mathbf{y}_i||)\right] \\ &= -k^2 \left[\sum_{i=1}^{n} \alpha_i \phi(||\mathbf{x}-\mathbf{y}_i||) \right. \\ &\left. + \sum_{i=n+1}^{N} \alpha_i (\mathbf{x}-\mathbf{y}_i)\cdot\nabla\phi(||\mathbf{x}-\mathbf{y}_i||)\right]. \end{aligned} \tag{6}$$

Taking the set of interpolation points identical to the set of centers and substituting the inner points $\{\mathbf{x}_j\}_{j=1}^{n} \in \Omega$ to Eq. (6) one gets the system of equations which in a matrix notation have a form

$$\mathcal{L}_I \boldsymbol{\alpha}_I + \mathcal{L}_B \boldsymbol{\alpha}_B = -k^2 (\mathcal{A}_I \boldsymbol{\alpha}_I + \mathcal{A}_B \boldsymbol{\alpha}_B). \tag{7}$$

Analogously, for $\{\mathbf{x}_j\}_{j=n+1}^{N} \in \partial\Omega$ substituted into Dirichlet or Neumann conditions one gets

$$\mathcal{B}_I \boldsymbol{\alpha}_I + \mathcal{B}_B \boldsymbol{\alpha}_B = 0, \tag{8}$$

where $\mathcal{B}_I$ and $\mathcal{B}_B$ have a different form for TM modes or TE modes. Eliminating $\boldsymbol{\alpha}_B$ in Eq. (7) using Eq. (8) one gets the following (n-dimensional) generalized eigenproblem

$$\begin{aligned} &\left[\mathcal{L}_I - \mathcal{L}_B\left(\mathcal{B}_B^{-1}\mathcal{B}_I\right)\right]\boldsymbol{\alpha}_I \\ &= -k^2\left[\mathcal{A}_I - \mathcal{A}_B\left(\mathcal{B}_B^{-1}\mathcal{B}_I\right)\right]\boldsymbol{\alpha}_I. \end{aligned} \tag{9}$$

The field distribution represented by Eq. (4) can be obtained from eigenvectors $\boldsymbol{\alpha}_I$ (and $\boldsymbol{\alpha}_B = -\mathcal{B}_B^{-1}\mathcal{B}_I\boldsymbol{\alpha}_I$) and the cutoff wavenumbers from the eigenvalues of Eq. (9), $\lambda = \dfrac{2\pi}{k}$.

3. Self-adaptive algorithm for choosing the set of interpolation centers

The main aim of that method is to generate the set of interpolation points which for a small number of points gives the highest accuracy of the solution.

In the first step one has to solve eigenproblem for the initial set of points – obtaining the initial eigenvalue and the corresponding initial eigenvector. It is equivalent to obtaining initial function $\Psi(\mathbf{x})$ defined for an an arbitrary point in $\overline{\Omega}$. In the next step one has to take a new arbitrary (usually larger) set of points $\{\widetilde{\mathbf{x}}_m\}_{m=1}^{M} \in \overline{\Omega}$ different than $\{\mathbf{x}_j\}$. For any point $\widetilde{\mathbf{x}}_m$ inaccuracy of the initial solution can be checked – if $\widetilde{\mathbf{x}}_m \in \Omega$, then the interpolation error can be obtained from substituting it into Eq. (3)

$$E_I(\widetilde{\mathbf{x}}_m) = \nabla^2\Psi(\widetilde{\mathbf{x}}_m) + k^2\Psi(\widetilde{\mathbf{x}}_m), \tag{10}$$

when $\widetilde{\mathbf{x}}_m \in \partial\Omega$ the error can be expressed by

$$E_B(\widetilde{\mathbf{x}}_m) = \Psi(\widetilde{\mathbf{x}}_m) \tag{11}$$

for TM modes or

$$E_B(\widetilde{\mathbf{x}}_k) = \mathbf{n}\cdot\nabla\Psi(\widetilde{\mathbf{x}}_k) \tag{12}$$

for TE modes. Using a matrix notation

$$\mathbf{E}_I = \left[\widetilde{\mathcal{L}}_I - \widetilde{\mathcal{L}}_B\mathcal{B}_B^{-1}\mathcal{B}_I + k^2\left(\widetilde{\mathcal{A}}_I - \widetilde{\mathcal{A}}_B\mathcal{B}_B^{-1}\mathcal{B}_I\right)\right]\boldsymbol{\alpha}_I \tag{13}$$

and

$$\mathbf{E}_B = \left[\widetilde{\mathcal{B}}_I - \widetilde{\mathcal{B}}_B\mathcal{B}_B^{-1}\mathcal{B}_I\right]\boldsymbol{\alpha}_I. \tag{14}$$

The values of elements of the vectors $\mathbf{E}_I$ and $\mathbf{E}_B$ correspond to inaccuracy of the initial solution at given points. Selecting elements whose values exceed the assumed inaccuracy one gets a subset of points $\widetilde{\mathbf{x}}_m$ which should be added to the initial set.

This algorithm is computationally by far more efficient than solving the eigenproblem for a set of points consisting of sets: $\{\mathbf{x}_j\}$ and whole $\{\widetilde{\mathbf{x}}_m\}$. It has to be noted that the operation can be repeated until the assumed accuracy is achieved.

4. Numerical results

Numerical tests were made for a few chosen shapes of waveguide cross-sections for which analytical results are known:

- circular waveguide of the radius $R = 1$;
- elliptical waveguide of the eccentricity $e = 0.9$ and the semimajor axis $a = 1$;
- rectangular waveguide of the width $a = 2$ and the height $b = 1$.

As it was noted, the results depend on the distribution of points (the set of centers) as well as shape parameter c. In the results presented, the initial set of the centers has a regular distribution (Fig. 1) and shape parameter $c = 3$.

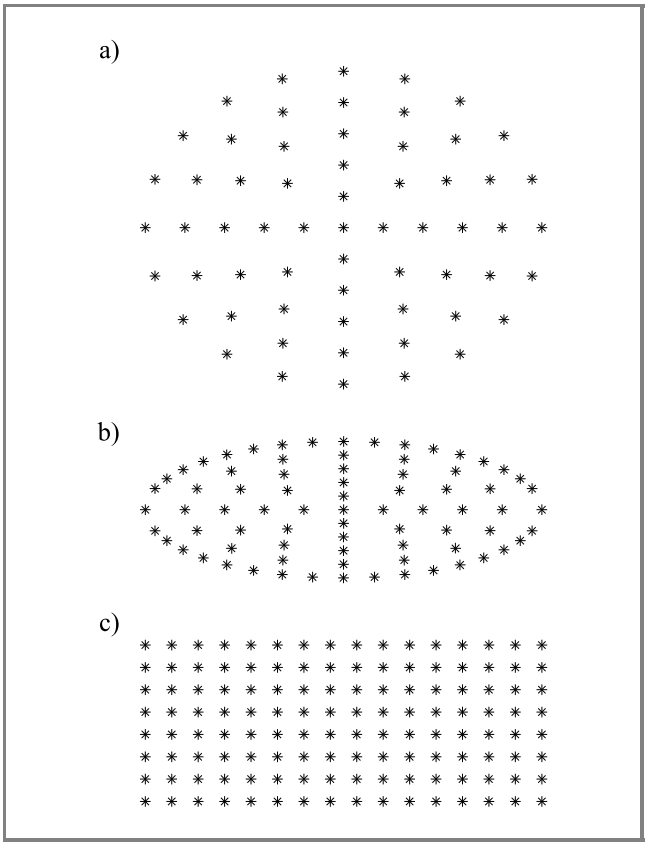


Fig. 1. The initial sets of points for: (a) circular ($N = 61$, $n = 41$); (b) elliptical ($N = 61$, $n = 41$); (c) rectangular ($N = 128$, $n = 84$) waveguides.

After using the self-adaptive algorithm, the density of points increased in regions where the accuracy was too low (Fig. 2).

Tables 1–3 shows the cutoff wavelengths for a few low order TM modes for considered shapes obtained from the standard RBFs method and the RBFs method with a self-adaptive algorithm. Analytical solutions are collected in the last column.

Table 1

The cutoff wavelengths for three lowest order TM modes for circular waveguide

RBF method	RBF with S-A	Analytical
2.6129	2.6127	2.6127
1.6420	1.6400	1.6397
1.2284	1.2238	1.2234

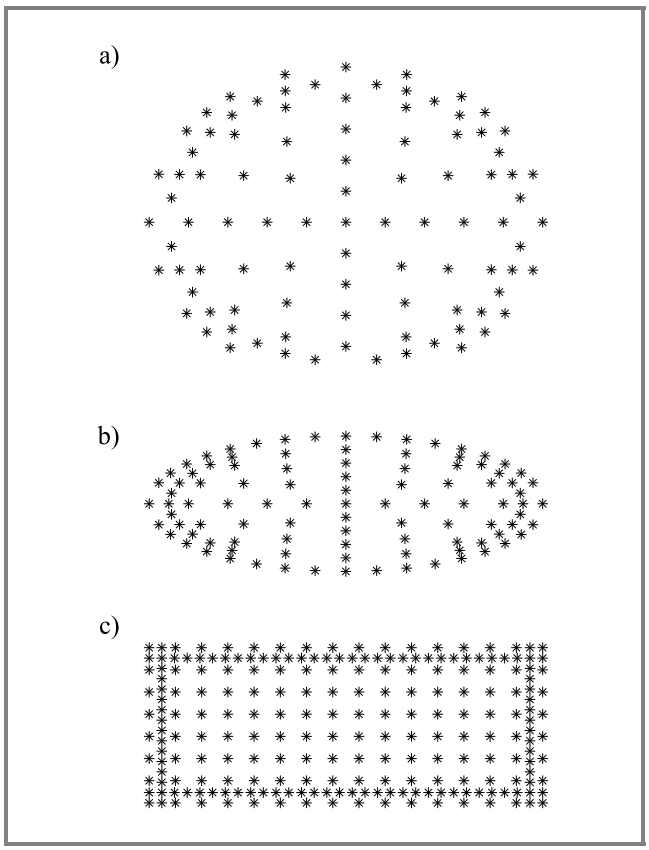


Fig. 2. The enriched (self-adapted algorithm) sets of points for: (a) circular ($N = 113$, $n = 73$); (b) elliptical ($N = 99$, $n = 63$); (c) rectangular ($N = 220$, $n = 168$) waveguides.

It can be seen that more nodes are needed for domains with corners to achieve the required accuracy.

Table 2

The cutoff wavelengths for three lowest order TM modes for elliptical waveguide

RBF method	RBF with S-A	Analytical
1.4912	1.4904	1.4906
1.1619	1.1605	1.1607
0.9420	0.9378	0.9375

Table 3

The cutoff wavelengths for three lowest order TM modes for rectangular waveguide

RBF method	RBF with S-A	Analytical
1.7896	1.7889	1.7889
1.4167	1.4143	1.4142
1.1085	1.1096	1.1094

5. Conclusions

The numerical tests shown in this paper are focused on TM modes analysis, however, it has to be noted that TE modes as well as TM can be found. The proposed method is applicable not only to waveguides of arbitrary cross-section, but also for any 3D structures. However, for regions of complex geometry (especially with re-entrant corners) number of interpolation points can be very large and method may be computationally not efficient (because of matrices which occur in eigenproblem are dense).
One of the essential problems of RBFs method is also selecting a value of a shape parameter c. The parameter c is of great importance for convergence and accuracy of the obtained solutions. Inappropriate choice of c can reduce accuracy or cause ill-conditioning of matrices.

References

[1] R. Frank, "Scattered data interpolation: test of some methods", *Math. Comput.*, vol. 38, pp. 181–199, 1972.

[2] E. J. Kansa and Y. C. Hon, "Circumventing the ill-conditioning problem with multiquadric radial basis function: applications to elliptic partial differential equations", *Comput. Math. Appl.*, vol. 39, pp. 123–137, 2000.

[3] R. B. Platte and T. A. Driscoll, "Computing eigenmodes of elliptic operators using radial basis functions", University of Delaware, 2003 (preprint).

[4] S. Rippa, "An algorithm for selecting a good value for parameter c in radial basis function interpolation", *Adv. Comput. Math.*, vol. 11, pp. 193–210, 1999.

[5] E. Larsson and B. Fornberg, "A numerical study of some radial basis function based solution methods for elliptic PDEs", *Comput. Math. Appl.*, vol. 46, pp. 891–902, 2003.

[6] P.-L. Jiang, S.-Q. Li, and C. H. Chan, "Analysis of elliptical waveguides by a meshless collocation method with the Wendland radial basis functions", *Microw. Opt. Technol. Lett.*, vol. 32, pp. 162–165, 2002.



Piotr Kowalczyk received the M.Sc. degree in applied physics from the Gdańsk University of Technology (GUT), Poland, in 2001. Currently he is working toward the Ph.D. degree in microwave and antenna engineering at the GUT. His research interests include numerical methods for microwave and photonic applications.
e-mail: kowal@yapipapi.eti.pg.gda.pl
Department of Electronics, Telecommunications and Informatics
Gdańsk University of Technology
Narutowicza st 11/12
80-952 Gdańsk



Michal Mrozowski received his M.S.E.E. and Ph.D., D.Sc. degrees with honors in microwave engineering from the Gdańsk University of Technology (GUT), Poland, in 1983, 1990 and 1994, respectively. Since 2001 he has been a Full Professor at the Gdańsk University of Technology. His interests are with computational electromagnetics and filed theory. He published over 50 reviewed journal papers and 2 monographs on computational electromagnetics and guided electromagnetic waves. He is a member of Electromagnetics Academy and Chairman of the Polish joint AES/AP/MTT Chapter.
e-mail: mim@pg.gda.pl
Department of Electronics, Telecommunications and Informatics
Gdańsk University of Technology
Narutowicza st 11/12
80-952 Gdańsk

Paper

FDTD analysis of magnetized plasma using an equivalent lumped circuit

Artur Moryc and Wojciech Gwarek

Abstract— The paper describes a new approach to electromagnetic analysis of magnetized plasma using finite difference time domain (FDTD) method. An equivalent lumped circuit describing an FDTD cell filled with plasma is developed and applied in the analysis. Such a method is proved more effective than previously reported methods. The new approach is verified on a canonical example of known analytical solution.

Keywords— FDTD, tensor permittivity, dispersive, anisotropic.

1. Introduction

Finite difference time domain (FDTD) method is one of the most useful methods in modeling of electromagnetic problems [1, 2]. Since its original formulation in the sixties it has been a subject of thousands of publications. One of important problems considered by FDTD researchers is effective analysis of dispersive media. Several approaches to this problem have been reported [3], but the one which seems to be most frequently used now is that of Kuntz and Luebbers [2]. In that approach the frequency dependence of the material properties is transformed into time domain through a convolution. It is shown [2] that an effective recursive updating of the convolution terms is possible. The convolution approach has been also applied to dispersive anisotropic media like magnetized plasma and magnetized ferrites [2, 4, 5]. It proved to be more effective than formerly published approaches like [6]. Recently the authors of this paper have developed an alternative approach to the analysis of magnetized ferrites [7]. A lumped equivalent circuit for ferrite-loaded FDTD cell has been developed and it has been applied to electromagnetic modeling algorithm. It proved simpler and more effective than previously reported algorithms. In this paper we extend application of that approach to the case of magnetized plasma. An equivalent lumped circuit describing an FDTD cell filled with plasma is developed and applied to electromagnetic modeling. Example of application shows perfect agreement with analytical solution of a canonical 1D example. The new approach is shown to be computationally more effective than formerly reported approaches [4, 5, 6] in the case of 2D and 3D circuits.

2. Plasma and its RLC models

The magnetized plasma is characterized in frequency domain by tensor permittivity which may be written as:

$$\varepsilon = \begin{pmatrix} \varepsilon_{xx}(\omega) & j\varepsilon_{xy}(\omega) & 0 \\ -\mathrm{j}\varepsilon_{yx}(\omega) & \varepsilon_{yy}(\omega) & 0 \\ 0 & 0 & \varepsilon_{zz}(\omega) \end{pmatrix}, \tag{1}$$

$$\varepsilon_{xx}(\omega) = \varepsilon_{yy}(\omega) = 1 - \frac{(\frac{\omega_p}{\omega})^2[1-\mathrm{j}\frac{\nu_c}{\omega}]}{[1-\mathrm{j}\frac{\nu_c}{\omega}]^2 - (\frac{\omega_b}{\omega})^2}, \tag{2}$$

$$\varepsilon_{yx}(\omega) = \varepsilon_{xy}(\omega) = \frac{(\frac{\omega_p}{\omega})^2 \frac{\omega_b}{\omega}}{[1-\mathrm{j}\frac{\nu_c}{\omega}]^2 - (\frac{\omega_b}{\omega})^2}, \tag{3}$$

$$\varepsilon_{zz}(\omega) = 1 + \frac{(\omega_p)^2}{\omega(\mathrm{j}\nu_c - \omega)}, \tag{4}$$

where ω_p is plasma frequency, ω_b is cyclotron frequency (proportional to the static filed H_0), and ν_c is the electron collision frequency, which describes the losses of the plasma medium.

Let us start from considering a 2-dimensional case of a TM wave propagating between two magnetic planes situated at $z = 0$ and $z = h$. Such a wave has two E-field components (E_x, E_y) and one H-field component (H_z). We can associate with them magnetic voltage $V = aH_z$ and magnetic current $J = -i_z E$. Under such assumptions the Maxwell equations can be written in form of (5) and(6) dual to the form of TE wave case considered in [8]:

$$\bigtriangledown V(x,y,t) = -L\frac{\partial J(x,y,t)}{\partial t}, \tag{5}$$

$$\bigtriangledown J(x,y,t) = -C\frac{\partial V(x,y,t)}{\partial t}. \tag{6}$$

Using FD discretization of space with cell size a and assuming $h = a$, these equations can be expressed for lossless case in a form:

$$-\mathrm{j}\omega C V^{m,n} = I_x^{m+0.5,n} - I_x^{m-0.5,n} + I_y^{m,n+0.5} - I_y^{m,n-0.5}, \tag{7}$$

$$-\mathrm{j}\omega L I_x^{m+0.5,n} = V^{m+1,n} - V^{m+1,n}, \tag{8}$$

where $V^{m,n} = aH_z(x = ma, y = na)$, $I_x^{m,n} = -aE_y(x = ma, y = na)$, $I_y^{m,n} = aE_x(x = ma, y = na)$, $C = \varepsilon a$ and $L = \mu a$.

Let us note that *LC* parameters have unusual meaning, i.e., L is related to electric field and C is related to magnetic field. We start from considering the case of isotropic cold plasma described by isotropic permittivity given by Eq. (4) (as in [3]). Figure 1 presents an equivalent lumped

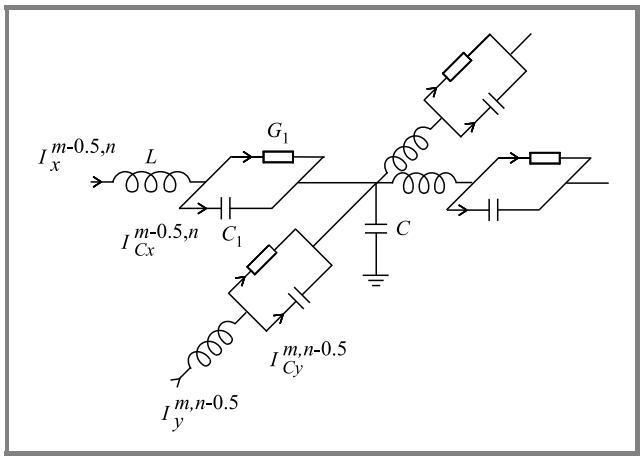


Fig. 1. Lumped equivalent circuit for isotropic plasma.

circuit describing such a medium. Then we switch to the magnetized plasma case. We consider a plasma material in which electric field E is related to displacement vector **D** by permittivity tensor given by Eqs. (1)–(4). Equation (7) does not change while Eq. (8) needs to be modified to the form of:

$$V^{m+1,n} - V^{m,n} = -\mathrm{j}\omega h\varepsilon_0 \left[(1+\chi) I_x^{m+0.5,n} - \mathrm{j}\frac{\frac{w_b}{w}}{1-\mathrm{j}\frac{v_c}{\omega}} \chi I_y^{m+0.5,n} \right], \quad (9)$$

where c can be expressed as:

$$\chi = \frac{w_p^2 \left(1 - \mathrm{j}\frac{R_1/L_1}{\omega}\right)}{(G_1 R_1 + 1)\omega_b^2 - \omega^2 + \mathrm{j}\omega\left(\frac{G_1}{C_1} + \frac{R_1}{L_1}\right)}, \quad (10)$$

where $\omega_b^2 = \dfrac{1}{L_1 C_1}$, $\omega_p^2 = \dfrac{1}{LC_1}$, $G_1 = C_1 v_c$ and $R_1 = L_1 v_c$.

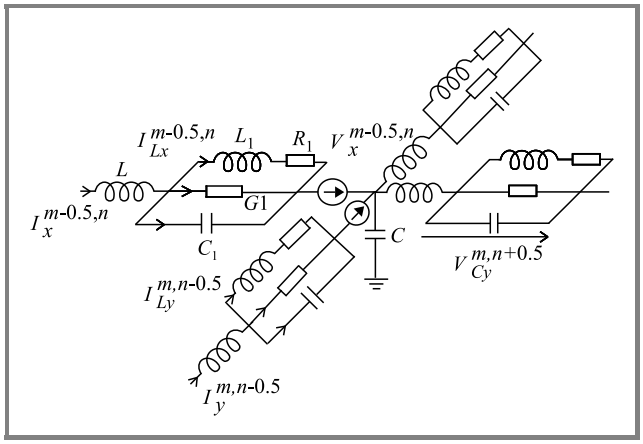


Fig. 2. Lumped equivalent circuit for anisotropic plasma.

Let us note that term (10) corresponds to parallel LC circuit resonating at the angular frequency ω_b and term $V_{cx}^{m+0.5,n} = -\dfrac{\mathrm{j}\omega L}{j\omega L_1 + R_1}\chi I_x^{m+0.5,n}$ describes voltage across the parallel LC circuit. The current $I_{Lx}^{m+0.5,n}$ flowing through the inductance arm is proporctional to this voltage multiplied by the admitance of the L_1R_1 conection. Thus we can describe our 2D FDTD cell filled with magnetized plasma by the lumped circuit of Fig. 2 with the source V_x driven by the current I_{Ly}.

3. Algorithm

The sequence of time-domain updating of FDTD equations for E_x and E_y fields needs to be carefully considered since in the equations containing the effects of off-diagonal anisotropy it is assumed that we should know at the same instant of time E_x to calculate E_y and E_y to calculate E_x. The problem has been solved by performing the updates in the following sequence:

1. E_x^{k+1} update based on E_x^k, $H_z^{k+0.5}$ and E_y^k components.
2. E_y^{k+1} update based on E_y^k, $H_z^{k+0.5}$ and E_x^{k+1} components.
3. Update of $H_z^{k+1.5}$ components.
4. E_y^{k+2} update based on E_y^{k+1}, $H_z^{k+1.5}$ and E_x^{k+1} components.
5. E_x^{k+2} update based on E_x^{k+1}, $H_z^{k+1.5}$ and E_y^{k+2} components.

Thus the FDTD algorithm based on the equivalent circuit of Fig. 2 proceeds the following way:

$$E_{x,m,n,i}^{k+1} = E_{x,m,n,i}^{k} + \Big(H_{z,m,n+0.5,i}^{k+0.5} - H_{z,m,n-0.5,i}^{k+0.5} - p_{x,m,n,i}^{k+0.5} + F_1 (e_{y,m-1,n+0.5,i}^{k} + e_{y,m-1,n-0.5,i}^{k} + e_{y,m,n-0.5,i}^{k} + e_{y,m,n+0.5,i}^{k}) \Big) F_2 , \quad (11)$$

$$e_{x,m,n,i}^{k+1} = F_3 e_{k,m,n,i} + F_4 p_{k,m,n,i}^{k+0.5}, \quad (12)$$

$$p_{x,m,n,i}^{k+1.5} = F_5 p_{k,m,n,i}^{k+0.5} + (E_{x,m,n,i}^{k+1} - e_{x,m,n,i}^{k+1}) F_6 , \quad (13)$$

$$E_{y,m,n,i}^{k+1} = E_{y,m,n,i}^{k} + \Big(H_{z,m-0.5,n,i}^{k+0.5} - H_{z,m+0.5,n,i-0.5}^{k+0.5} - p_{y,m,n,i}^{k+0.5} - F_1 (e_{k,m-0.5,n-1,i} + e_{x,m+0.5,n-1,i}^{k+1} + e_{x,m-0.5,n,i}^{k+1} + e_{x,m+0.5,n,i}^{k+1}) \Big) F_2 \quad (14)$$

$$e_{y,m,n,i}^{k+1} = F_3 e_{k,m,n,i} + F_4 p_{k,m,n,i}^{k+0.5}, \quad (15)$$

$$p_{y,m,n,i}^{k+1.5} = F_5 p_{k,m,n,i}^{k+0.5} + (E_{y,m,n,i}^{k+1} - e_{y,m,n,i}^{k+1}) F_6 . \quad (16)$$

Where p_x, p_y, e_x, e_y are algorithm varibles coresponding to V_{cx},V_{cy},I_x,I_y in Fig. 2, respectively, $F_1 = 0.25L_1\omega_b$, $F_2 = \frac{\Delta t}{C}$, $F_3 = \frac{1-\frac{R_1\Delta t}{2L_1}}{1+\frac{R_1\Delta t}{2L_1}}$, $F_4 = \frac{\Delta t}{L_1}\frac{1}{1+\frac{R_1\Delta t}{2L_1}}$, $F_5 = \frac{1-\frac{G_1\Delta t}{2C_1}}{1+\frac{G_1\Delta t}{2C_1}}$, and $F_6 = \frac{\Delta t}{C_1}\frac{1}{1+\frac{G_1\Delta t}{2C_1}}$.

The algorithm presented here for a 2D can be relatively easily extended to a 3D case. Table 1 presents comparison of computer resources needed for our algorithm and for that of Kunz and Luebbers [2]. Operation count is understood as

Table 1

Comparison of operation count of various methods

Algorithm	Variables		Operation count			
	2D	3D	2D		3D	
			$V_c > 0$	$V_c = 0$	$V_c > 0$	$V_c = 0$
Our method	7	10	37	33	56	52
Kunz and Luebbers [2]	7	10	77		96	

the number of floating point operations needed per FDTD cell and per iteration. It can be seen that the algorithm presented here is significantly more effective.

4. Example

Verification of the accuracy of our algorithm has been conducted on a canonical 1D problem previously considered in [5]. A Gaussian pulse plane wave is normally incident on a longitudinally magnetized plasma layer. The pulse travels through 350 FDTD cells of the total length of 15 mm. The magnetized plasma is placed between cells numbered 200 and 320 and its length is 9 mm. The other cells are filled with air. Both ends of the free space region are terminated by Mur absorbing boundary condition. For these simulations the following parameters of the plasma were assumed:

$$\omega_p = 2\pi \cdot 50 \cdot 10^9 \ \frac{\text{rad}}{\text{s}},$$

$$\omega_b = 3 \cdot 10^{11} \ \frac{\text{rad}}{\text{s}},$$

$$\nu_c = 2 \cdot 10^{10} \ \frac{\text{rad}}{\text{s}}.$$

The S parameters versus frequency for vertical and horizontal polarization were calculated just in front of and behind the plasma. These parameters were used to calculate right-

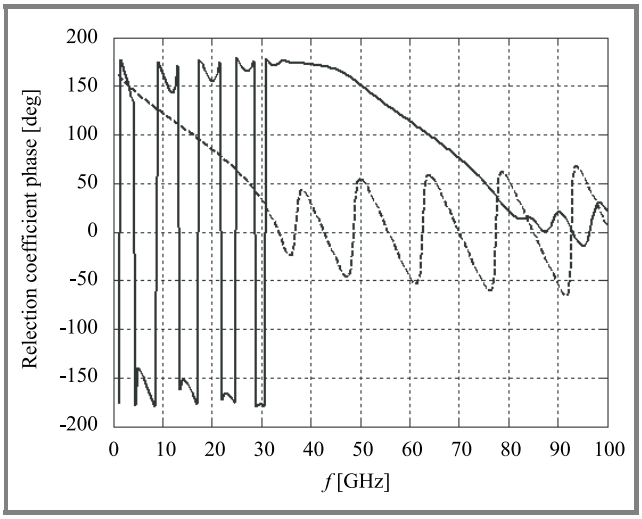


Fig. 4. FDTD reflection coefficient phase versus frequency for a plane wave incident on a plasma slab, continuous line corresponds to RCP, dashed line corresponds to LCP.

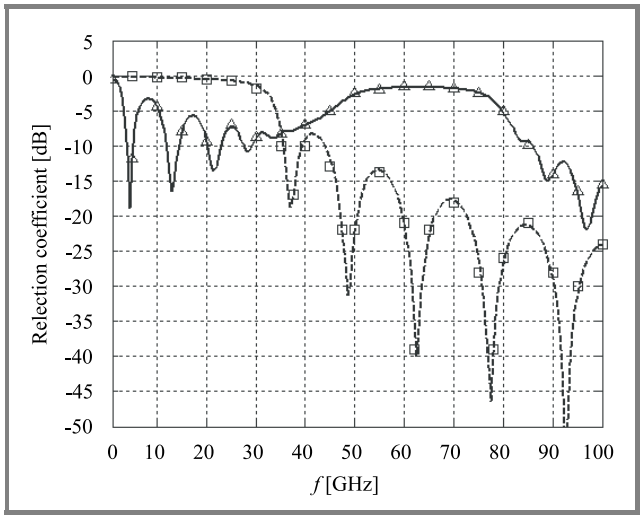


Fig. 3. FDTD reflection coefficient magnitude versus frequency for a plane wave incident on a plasma slab, continuous line corresponds to RCP, dashed line corresponds to LCP, triangles and squares the analytical results after [5].

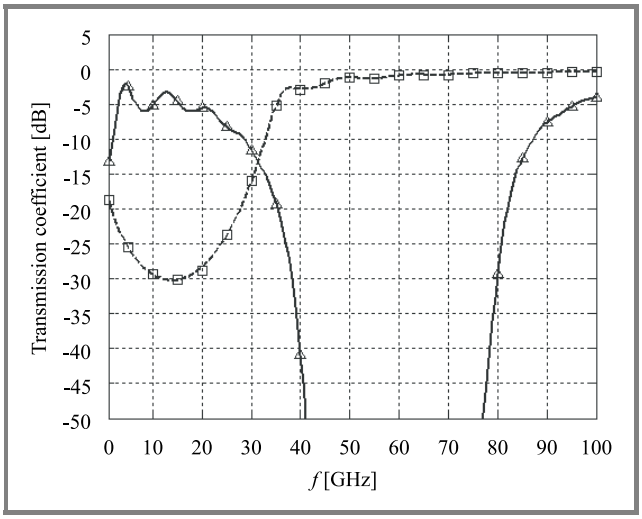


Fig. 5. FDTD transmission coefficient magnitude versus frequency for a plane wave incident on a plasma slab, continuous line corresponds to RCP, dashed line corresponds to LCP, triangles and squares the analytical results after [5].

hand and left-hand circularly polarized coefficients according to the formulae:

$$T_{RCP}(\omega) = S_{21x}(\omega) + \mathrm{j}S_{21y}(\omega), \tag{17}$$

$$T_{LCP}(\omega) = S_{21x}(\omega) - \mathrm{j}S_{21y}(\omega), \tag{18}$$

$$R_{RCP}(\omega) = S_{11x}(\omega) + \mathrm{j}S_{11y}(\omega), \tag{19}$$

$$R_{LCP}(\omega) = S_{11x}(\omega) - \mathrm{j}S_{11y}(\omega). \tag{20}$$

Figure 3 shows calculated results of reflection coefficients for right-hand and left-hand circular polarizations (denoted RCP and LCP, respectively). Perfect agreement with analytical results after [5] are obtained. Similarly good agreement

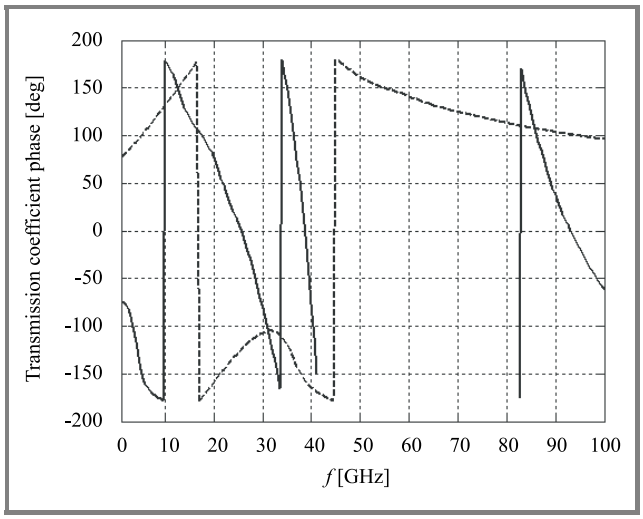


Fig. 6. FDTD transmission coefficient phase versus frequency for a plane wave incident on a plasma slab, continuous line corresponds to RCP (from 40 GHz to 80 GHz data are not presented due to phase uncertainties when the attenuation drops below –50 dB), dashed line corresponds to LCP.

with [5] has been obtained for the transmission coefficients (shown in Fig. 5) and for phase relations for both coefficients (shown in Figs. 4 and 6).

5. Conclusions

In this paper a new approach to FDTD analysis of magnetized plasma has been presented. It has been verified on a canonical example with known analytical solution. It proved to be more effective than previously reported approaches. At the same time it has been found robust and reliable in practical simulations of 2D and 3D cases.

References

[1] A. Taflove, *Computational Electrodynamics. The FDTD Method.* Artech House, 1995.

[2] K. Kunz and R. Luebbers, *The Finite Difference Time Domain Method for Electromagnetics*. CRC Press, 1993, ch. 15.

[3] J. L. Young and R. O. Nelson, "A summary and systematic analysis of FDTD algorithm for linearly dispersive media", *IEEE Anten. Propagat. Mag.*, vol. 43, no. 1, pp. 61–75, 2001.

[4] R. J. Loubbers and F. Hunsberger, "A frequency-dependent finite-difference time-domain formulation for transient propagation in plasma", *IEEE Trans. Anten. Propagat.*, vol. 39, no. 1, 1991.

[5] F. Hunsberger and R. Luebbers, "Finite-difference time-domain analysis of gyrotropic media. I: Magnetized plasma", *IEEE Trans. Anten. Propagat.*, vol. 40, no. 12, 1992.

[6] T. Kashiwa and N. Yoshida, "Transient analysis of magnetized plasma in tree-dimencional space", *IEEE Trans. Anten. Propagat.*, vol. 36, no. 8, pp. 1096–1105, 1988.

[7] W. Gwarek and A. Moryc, "An alternative approach to FDTD analysis of magnetized ferrites", *IEEE Microw. Wirel. Compon. Lett.*, vol. 40, pp. 331–333, 2004.

[8] W. Gwarek, "Analysis od an arbitrarily-shaped planar circuit-a time-domain approach", *Trans. Microw. Theory Techn.*, vol. MTT-33, no. 10, 1985.



Artur Moryc was born in Poland in 1977. He received the M.Sc. degree in physics in 2001 from Warsaw University, Poland. In 2002 he become a Ph.D. student at Warsaw University of Technology in the domain of electromagnetic modeling for applications in electronics. Since that time he has concentrated on applications of the finite difference time domain method. Currently, he is focused on development of new, more effective approach to FDTD analysis of electromagnetic fields in anizotropic and dispersive media such as ferrite and magnetized plasma.
e-mail: amoryc@elka.pw.edu.pl
Institute of Radioelectronics
Warsaw University of Technology
Nowowiejska st 15/19
00-665 Warsaw, Poland

Wojciech Gwarek – for biography, see this issue, p. 28.

INFORMATION FOR AUTHORS

The *Journal of Telecommunications and Information Technology* is published quarterly. It comprises original contributions, both regular papers and letters, dealing with a broad range of topics related to telecommunications and information technology, Items included in the journal report primary and/or experimental research results, which advance the base of scientific and technological knowledge about telecommunications and information technology.

The *Journal* is dedicated to publishing research results which advance the level of current research or add to the understanding of problems related to modulation and signal design, wireless communications, optical communications and photonic systems, speech devices, image and signal processing, transmission systems, network architecture, coding and communication theory, as well as information technology. Suitable research-related manuscripts should hold the potential to advance the technological base of telecommunications and information technology. Tutorial and review papers are published by invitation only.

Papers published by invitation and regular papers should contain up to 15 and 8 printed pages respectively (one printed page corresponds approximately to 3 double-space pages of manuscript, where one page contains approximately 2000 characters).

Manuscript: An original and two copies of the manuscript must be submitted, each completed with all illustrations and tables attached at the end of the papers.

Tables and figures have to be numbered consecutively with Arabic numerals. The manuscript must include an abstract limited to approximately 100 words. The abstract should contain four points: statement of the problem, assumptions and methodology, results and conclusion, or discussion, of the importance of the results. The manuscript should be double-spaced on only one side of each A4 sheet (210 × 297 mm). Computer notation such as Fortran, Matlab. Mathematica etc., for formulae, indices, etc. is not acceptable and will result in automatic rejection of the manuscript. The style of references, abbreviations, etc., should follow the standard IEEE format.

References should be marked in the text by Arabic numerals in square brackets and listed at the end of the paper in order of their appearance in the text, including exclusively publications cited inside. The reference entry (correctly punctuated according to the following rules and examples) **has to contain.**

From journals and other serial publications: initial(s) and second name(s) of the author(s), full title of publication (transliterated into Latin characters in case it is in Russian, possibly preceded by the title in Russian characters), appropriately abbreviated title of periodical, volume number, first and last page number, year. E.g.:

[1] Y. Namihira, "Relationship between nonlinear effective area and modefield diameter for dispersion shifted fibres", *Electron. Lett*., vol. 30, no. 3, pp. 262–264, 1994,

From non-periodical, collective publications: as above, but after title the name(s) of editor(s), title of volume and/or edition number, publisher(s) name(s) and place of edition, inclusive pages of article. year. E.g.:

[2] S. Demri and E. Orłowska. "International representability: Abstract models versus concrete models" in *Fuzzy Sets, Logics and Reasoning about Knowledge*, D. Dubois and H. Prade, Eds. Dordrecht: Kluwer, 1999, pp. 301–314.

From books initial(s) and name(s) of the author(s), place of edition, title, publisherts), year. Eg.:

[3] C. Kittel, *Introduction to Solid State Physics*. New York: Wiley, 1986.

Figure captions should be started on separate sheet of papers and must be double-spaced.

Illustration. Original illustrations should be submitted. All line drawings should be prepared on white drawing paper in black India ink. Drawings in Corel Draw and Postscript formats are preferred. Colour illustrations are accepted only in exceptional circumstances. Lettering should be large enough to be readily legible when drawing is reduced to two- or one column width as much as 4:1 reduction from the original. Photographs should be used sparingly. All photographs must be gloss prints. All materials, including drawings and photographs, should be no larger than 175 × 260 mm.

Page number: Number all pages, including tables and illustrations (which should be grouped at the end), in a single series, with no omitted numbers.

Electronic form: A floppy disk together with the hard copy of the manuscript should be submitted. It is important to ensure that the diskette version and the printed version are identical. The diskette should be labelled with the following information: a) the operating system and word-processing software used, b) in case of UNIX media, the method of extraction (ie. tar) applied, c file name(s) related to manuscript. The diskette should be properly packed in order to avoid possible damage during transit.

Among various acceptable word processor formats, TEX and LATEX are preferable. The *Journal's* style file is available to authors.

Galley proofs: Proofs should be returned by authors as soon as possible. In other cases, the article will be proof-read against manuscript by the editor and printed without the author's corrections. Remarks to the errata should be provided within two weeks after receiving the offprints.

The copy of the "Journal" shall be provided to each author of papers.

Copyright: Manuscript submitted to this journal may not have been published and will not be simultaneously submitted or published elsewhere. Submitting a manuscript, the authors agree to automatically transfer the copyright for their article to the publisher if and when the article is accepted for publication. The copyright comprises the exclusive rights to re produce and distribute the article, including reprints and also all translation rights. No part of the present journal may be reproduced in any form nor transmitted or translated into a machine language without permission in written form from the publisher.

Biographies and photographs of authors are printed with each paper. Send a brief professional biography not exceeding 100 words and a gloss photo of each author with the manuscript.

Application of optical dispersion techniques in phased array antenna beam steering

M. Muszkowski and E. Sędek — Paper — 50

A lightweight planar antenna element with optimized feed for use onboard spacecraft

K. Wincza and P. Kabacik — Paper — 53

Applying the radiated emission to the specific emitter identification

J. Dudczyk, M. Wnuk, and J. Matuszewski — Paper — 57

Broadside coupled stripline with double-side UC-PBG structure

P. Meissner and M. Kitliński — Paper — 61

All-optical intensity noise suppression for solid-state and semiconductor lasers

M. Csörnyei, T. Berceli, and T. Marozsák — Paper — 65

Mesh-free approach to Helmholtz equation based on radial basis functions

P. Kowalczyk and M. Mrozowski — Paper — 71

FDTD analysis of magnetized plasma using an equivalent lumped circuit

A. Moryc and W. Gwarek — Paper — 75

National Institute
of Telecommunications
Szachowa st 1
04-894 Warsaw, Poland

Editorial Office

tel. +48(22) 872 43 88
tel./fax:+48(22) 512 84 00
e-mail: redakcja@itl.waw.pl
http://www.itl.waw.pl/jtit

JOURNAL OF TELECOMMUNICATIONS AND INFORMATION TECHNOLOGY 2/2005